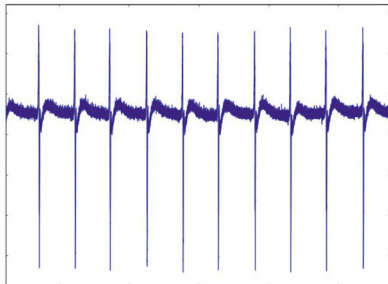
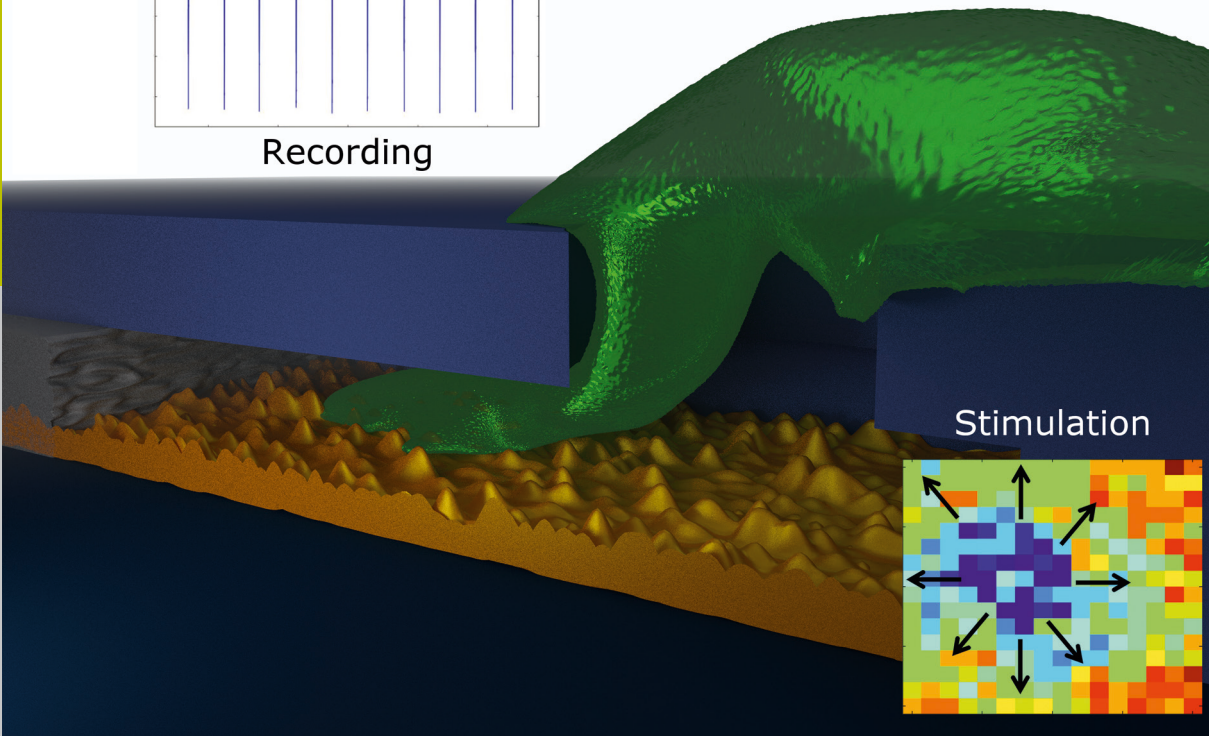


Nanocavity Arrays for Extracellular Recording and Stimulation of Electroactive Cell Systems

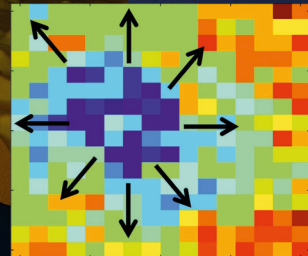
Anna Czeschik



Recording



Stimulation



Schlüsseltechnologien /
Key Technologies
Band / Volume 125
ISBN 978-3-95806-144-6

Forschungszentrum Jülich GmbH
Peter Grünberg Institute/Institute of Complex Systems
Bioelectronics (PGI-8/ICS-8)

Nanocavity Arrays for Extracellular Recording and Stimulation of Electroactive Cell Systems

Anna Czeschik

Schriften des Forschungszentrums Jülich
Reihe Schlüsseltechnologien / Key Technologies

Band / Volume 125

ISSN 1866-1807

ISBN 978-3-95806-144-6

Bibliographic information published by the Deutsche Nationalbibliothek.
The Deutsche Nationalbibliothek lists this publication in the Deutsche
Nationalbibliografie; detailed bibliographic data are available in the
Internet at <http://dnb.d-nb.de>.

Publisher and
Distributor: Forschungszentrum Jülich GmbH
Zentralbibliothek
52425 Jülich
Tel: +49 2461 61-5368
Fax: +49 2461 61-6103
Email: zb-publikation@fz-juelich.de
www.fz-juelich.de/zb

Cover Design: Grafische Medien, Forschungszentrum Jülich GmbH

Printer: Grafische Medien, Forschungszentrum Jülich GmbH

Copyright: Forschungszentrum Jülich 2016

Schriften des Forschungszentrums Jülich
Reihe Schlüsseltechnologien / Key Technologies, Band / Volume 125

D 82 (Diss. RWTH Aachen University, 2016)

ISSN 1866-1807
ISBN 978-3-95806-144-6

The complete volume is freely available on the Internet on the Jülicher Open Access Server (JuSER)
at www.fz-juelich.de/zb/openaccess.



This is an Open Access publication distributed under the terms of the [Creative Commons Attribution License 4.0](https://creativecommons.org/licenses/by/4.0/),
which permits unrestricted use, distribution, and reproduction in any medium, provided the original work is properly cited.

Zusammenfassung

Mikroelektrodenarrays (MEAs) sind aktueller Stand der Technik für extrazelluläre Messungen und Stimulationsexperimente an biologischem Gewebe und stellen eine wichtige Komponente in der Entwicklung biomedizinischer Anwendungen wie Retina-, Cochlear-Implantate und motorische Prothesen, sowie Herzschrittmachern und Wirkstoffuntersuchungen dar. Daher repräsentiert die Erforschung funktionaler Zell-Sensor-Schnittstellen und die Entwicklung neuartiger Oberflächenstrukturen und -modifikationen für verbesserte Elektrodeneigenschaften ein lebhaftes und fest etabliertes Fachgebiet dar. Eine große Herausforderung stellt hier die Vereinigung von örtlicher Auflösung, hinreichend für Messungen an einzelnen Zellen, und guter Signaleinkopplung dar. Ein notwendiger Aspekt hierfür ist die lückenlose Verbindung von Zelle und Elektrode. Generell bringen Elektroden mit Durchmessern kleiner als $20\ \mu\text{m}$ den Nachteil von hoher elektrischer Impedanz mit sich, welches das elektrische Rauschen bei Spannungsmessungen stark beeinflusst. In dieser Arbeit wird ein Nanocavity Sensor Array mit nanostrukturierten Elektroden für spannungsgesteuerte Stimulation

und extrazelluläre Aktionspotentialmessungen an zellulären Netzwerken präsentiert.

Diese Arbeit lässt sich in vier Teile strukturieren: Die Fabrikation des Sensors, seine Charakterisierung, gefolgt von der Evaluation für Zellanwendungen. Außerdem wird ein alternatives elektrogenes Zellsystem untersucht, hinsichtlich der Suche nach einem von Primärkultur und Tiernutzung unabhängigen neuronenenähnlichen Modellsystem.

Hinsichtlich der Sensorfabrikation wird zunächst die auf der Nutzung der Opferschicht eines konventionellen MEA basierende Herstellung von Nanocavity Arrays beschrieben, welche durch nasschemisches Ätzen realisiert wird. Die Sensorstabilität gegenüber Zellkulturbedingungen wird durch die Kultivierung von kardiomyozytenähnlichen Zellen getestet. Im Folgenden wird die Nanostrukturierung der Elektrodenoberfläche durch Interdiffusion eruiert und der Sensor hinsichtlich Elektrodenimpedanz und -kapazität zur Einschätzung der elektrischen Eigenschaften für Zelluntersuchungen charakterisiert. Mit Hilfe mikroskopischer Untersuchungen wird der der Strukturierung zugrunde liegende Prozess in Bezug auf Oberflächenrauigkeit, -struktur und -zusammensetzung näher untersucht. Die Ergebnisse werden daraufhin im Kontext der möglichen Anwesenheit von Fremdatomen und Verunreinigungen diskutiert, welche Hydrophobizität und Elektrodenkapazität als zwei sehr wichtige Parameter in der elektrophysiologischen Zell-Schnittstelle beeinflussen können.

Abschließend wird durch Adhäsionsuntersuchungen, Aktionspotentialmessungen und Stimulation die Sensorfunktionalität für Zellanwendungen demonstriert. Ein weiterer Teil dieser Arbeit stellt die Differenzierung der kommerziell erwerbzbaren neuronalen Zelllinie ReN-

cell VM dar. Diesbezüglich wurden verschiedene Protokolle getestet und die differenzierten Zellen elektrisch stimuliert, um die Entwicklung von spannungs-gesteuerten Ionenkanälen zu prüfen.

Zusammenfassend wird in dieser Studie ein Sensor-System zur Erforschung der Kommunikation zwischen Zelle und Chip präsentiert, welches komplettiert wird durch einen Ansatz zur Entwicklung eines neuronähnlichen elektrogenen Zellmodells, basierend auf der Differenzierung einer Zelllinie anstatt der Nutzung von primärer Zellkultur.

Abstract

Microelectrode arrays (MEAs) are state-of-the-art devices for extracellular recording and stimulation of biological tissue. Furthermore, they are a relevant tool for the development of biomedical applications like retina, cochlear and motor prostheses, cardiac pacemakers and drug screening. Hence, research on functional cell-sensor interfaces, as well as the development of new surface structures and modifications for improved electrode characteristics, is a vivid and well established field. Combining single-cell resolution with sufficient signal coupling remains challenging due to poor cell-electrode sealing. Furthermore, electrodes with diameters below 20 μm often suffer from a high electrical impedance affecting the noise during voltage recordings. In this study, a nanocavity sensor array with nanostructured electrodes for voltage-controlled stimulation and extracellular action potential recordings on cellular networks is presented.

This work mainly consists of four parts: The device fabrication, its characterization, followed by the device evaluation for cell applications. Additionally, an alternative electrogenic cell system is investigated,

emphasizing the advantages of a neuron-like cell system, which is not relying on animal use for primary cell culture.

First, a simplified method for the fabrication of nanocavity arrays is realized, based on utilizing the sacrificial layer of a conventional MEA and is performed by a wet-etch procedure. The device's stability is tested under cell culture conditions by culturing cardiomyocyte-like cells on chip. Next, the nanostructuring of the electrode surface by interdiffusion is introduced and the device is characterized in terms of electrode impedance and capacity in order to evaluate the electric properties for cell interactions. To examine the underlying structuring processes in detail, microscopic investigations are carried out targeting surface roughness, structure and composition. The results are discussed in relation to possible foreign atoms and contaminations, influencing hydrophilicity and electrode capacitance as two important parameters in interfacing cells electrophysiologically.

Finally, the device's functionality for cell applications is demonstrated by cell adhesion investigations, action potential recordings and stimulation. Subsequently, different strategies in differentiation of the commercially available neuronal progenitor cell-line ReNcell VM are tested. Differentiated cells are electrically stimulated, demonstrating the development of voltage-gated ion channels. In summary, a system for investigation of cell-chip communication is presented, completed by an approach to develop a neuron-like electrogenic cell model based on cell-line differentiation instead of primary cell culture.

Contents

1	Introduction	1
2	Fundamentals & Theory	7
2.1	Basics of Electrophysiology	8
2.1.1	Membrane Potential	8
2.1.2	Action Potentials	11
2.1.3	Signal Propagation	17
2.2	Cell Models for Electrophysiology	22
2.2.1	HL-1	22
2.2.2	ReNcell VM	22
2.3	MEAs and the Electrode-Electrolyte Interface	24
2.3.1	Helmholtz Double Layer	25
2.3.2	Gouy-Chapman Model	26
2.3.3	Gouy-Chapman-Stern Model	28
2.3.4	Butler-Volmer Equation	30
2.3.5	Surface Modifications	32
2.4	Extracellular Recording and Stimulation	35
2.4.1	Point Contact Model	35

2.4.2	Stimulation Forms	37
2.4.3	Charge Transfer	38
2.5	Optical Detection	39
3	Materials & Methods	43
3.1	Device	44
3.1.1	Planar MEA	44
3.1.2	Sacrificial Layer Etching	45
3.1.3	Surface Structuring by Inter- diffusion	47
3.1.4	Gold Interdiffusion Samples	47
3.2	Characterization	48
3.2.1	Electrochemical Impedance Spectroscopy	48
3.2.2	AFM	51
3.2.3	SEM	53
3.2.4	Contact Angle Measurement	56
3.3	Cell Culture	57
3.3.1	HL-1	57
3.3.2	ReNcell VM	60
3.3.3	Immunofluorescence Analysis	63
3.4	Setup	65
3.4.1	Amplifier System	65
3.4.2	Calcium Imaging	68
4	Results & Discussion	73
4.1	Nanocavity Devices	74
4.1.1	Cavity Formation by Chrome Etching	74

4.2	Characterization	78
4.2.1	Impedance and Capacity	78
4.2.2	AFM: Surface Roughness	85
4.2.3	SEM/EDX: Surface Structure and Composition	86
4.2.4	Contact Angle: Surface Energy	101
4.2.5	FIB: Cell-Chip Coupling	104
4.3	Application	107
4.3.1	Action Potential Recordings	107
4.3.2	Voltage-Controlled Stimulation	110
4.4	Implementation of an Alternative Cell System	115
4.4.1	Differentiation Protocols and Immunostaining	116
4.4.2	Optical Action Potential Detection	118
4.4.3	Voltage-Controlled Stimulation	128
5	Conclusion & Outlook	133
	References	139
	Author's list of publications	159
	Acknowledgements	161

Contents

Chapter 1

Introduction

The term “bioelectronics” describes an expanded and vivid interdisciplinary research field. Especially cell-based bioelectronics, targeting the convergence of electronics with biology and biotechnology [1], does not only affect the world of science and research, but does also inspire society, arts and subcultures. This manifests in the biohacking movement [2–4], focusing on a wide range of fields like do-it-yourself biology, genomics, body enhancements and following the idea of cyborgs. The latter originally describes a fictional being containing organic and biomechanical parts, but is usually applied to a human organism with integrated artificial components or technology [5, 6]. The idea of merging aspects of human life and electronics was widely pictured in popular culture like science fiction TV shows (the “Star Trek” cyborg character Seven Of Nine), movies (the movie “Matrix” (1999), which emphasizes

brain-machine interface or the movie “Avatar” (2009), which features mind-uploading) and literature (“Neuromancer” (1984) by William Gibson).

Those pop-cultural ideas of enhancing the human body with electronic devices have been answered in the last years by research with highly functional implants and prostheses. These devices generally feature a transducer, which connects the electronic system with the biological system. In case of electrical implants and prostheses, the transducer is usually an electrode or an array of electrodes, interfacing cells of the addressed body part. Strategies in restoring sight by retina prostheses [7], treating loss of limbs [8] and physical abilities by motor prostheses and exoskeleton suits (“HAL 5”, developed by Tsukuba University and Cyberdyne), hearing deficit by cochlear implants [9] and cardiac arrhythmia by implantable pacemakers and defibrillators [10] are no fiction anymore. Besides applications in patient therapy, bioelectronic devices and on-chip technologies play also an important role in research of diseases (like the neurodegenerative Parkinson’s or Alzheimer’s Disease [11, 12]) or pharmacological studies and drug screening [12, 13]. Both therapy and research applications demand attention on the cell-transducer interface. Several sensor concepts are realized here, which can be classified by the fabrication method (complementary metal oxide semiconductor (CMOS) technology or lithography) or transducing system (for example field effect transistor (FET) or microelectrode array (MEA)).

To investigate single cells as well as intracellular communication in cell networks, microelectrode arrays (MEAs) are widely used and are the tools of choice in many extracellular *in vitro* and *in vivo* investigations [14]. One advantage here lies in the less complex buildup

than used for FETs. Further, MEAs can be fabricated with CMOS or CMOS-independent processes and arbitrary electrode sizes on silicon- or glass-based substrates [15–17]. The use of MEAs facilitates non-invasive, highly parallelized electrophysiological recordings [18, 19] and neuroelectrochemical measurements [20, 21]. For instance, MEAs can be used for the detection of neurotransmitter release on the network level as opposed to carbon fiber electrodes [22, 23]. In general, cells can be cultured on chip-based sensors up to several weeks or months enabling long-term experiments. Hence, they provide an interesting alternative to probe-based techniques that are currently the gold standard for this type of measurements.

Optimizing the physical interface properties remains a major task in bioelectronics [14, 24]. Standard planar microelectrodes have some shortcomings regarding impedance and resolution of single cell voltage-based measurements. To provide an appropriate spatial resolution, the electrode size should not overcome the size of a single cell. This electrode miniaturization, however, leads to a higher electrode impedance and therefore additional electronic noise.

Another crucial aspect in the performance of on-chip electrical experiments on biological tissue is the seal resistance of the electrode–cell interface [15]. A large gap between cell and electrode represents one of the main drawbacks of planar bio-chips [15, 25, 26] since it causes a low junction resistance and thus large leakage currents, resulting in a low signal-to-noise ratio (SNR). Additionally, electrodes with a high distance to the cell require higher electrode potentials in cell stimulation experiments.

Various attempts in material research and design of sensor surfaces aim for a functional cell-sensor interface and an efficient signal transmis-

sion. Different layouts have been realized to support cell guidance [27], adherence [24], and sealing [28] for electrical and chemical recording. Approaches for improving the cell-sensor interface include: surface modifications by nanopores, -pillars [29, 30], -spines [31, 32] and -wires [33, 34] as well as neurocages [35], graphene [36] and carbon nanotubes [37–40] or interdigitated geometries [41].

Nanocavity arrays are promising devices for localized on-chip recordings of electrogenic cells in a network, due to their high spatial resolution and good signal to noise characteristics [42, 43]. They combine a large electrode area – and therefore low electrode impedance – with a small cavity opening.

Another improvement of the electrode impedance can be achieved by nanostructuring the electrode surface [30]. This increases the effective electrode area and could thus increase the electrode capacitance and lower the sensor impedance. Also such a structured surface is assumed to be advantageous for cell adhesion [44].

In this thesis a new simplified approach to fabricate nanocavity sensors is presented and its applicability evaluated by extracellular action potential recordings and voltage-controlled stimulation. The need for an easily accessible fabrication method is addressed by utilizing the adhesion layer of a standard MEA and introducing nanostructuring of the electrode material by interdiffusion, which further improves the electrode characteristics and could be beneficial for cell adhesion. The fabrication method is investigated and the device was characterized in terms of electrode impedance and capacitance. This study further focuses on an understanding of the underlying interdiffusion effect by demonstrating the influence of the processing temperature. Structural examination was carried out by atomic force microscopy (AFM),

scanning electron microscopy (SEM) and discussed under consideration of surface energy and composition influences. The quality of cell-chip coupling is documented by focused ion beam (FIB) sectioning. Action potential recordings were performed on a model system of cardiomyocyte-like HL-1 cells and the cell networks response to voltage-controlled stimulation was observed by simultaneous calcium imaging.

The beneficial electronic and cell adhesion properties of nanocavities and surface structuring are combined here, leading to a low impedance device with a high spatial resolution for interfacing single cells and cell networks. Further, the efficiency of nanocavity fabrication and electrode structuring is optimized by utilizing standard device components and process steps.

The second part of this work is the differentiation and implementation of an alternative electrogenic cell system for electrophysiological applications. Several differentiation strategies are tested and on-chip stimulation with simultaneous calcium imaging was performed to investigate the development of voltage-sensitive ion channels. This offers the opportunity to further implement a neuron-like cell system without using primary cell culture from animals.

The scripture is structured as following. First, in chapter 2, a general introduction in the underlying theoretical aspects is given. This includes basic electrophysiology and the electrophysiology of the investigated cell systems, the description of the electrode-electrolyte interface which is pivotal for any cell culture experiment with MEAs and subsequently, the fundamentals of the targeted experiments of cell recording and stimulation as well as optical detection of action potentials are described. An overview on the used materials and methods is

1. Introduction

given in chapter 3. Here, the device fabrication is described as well as characterization techniques, concluding with a introduction to the cell culture protocols and the setup for recording and stimulation applications. The results of this thesis are presented and discussed in chapter 4, ranging from the device processing and the device characterization in terms of electrical and structural properties to the device application for cell experiments. Finally, the findings in the implementation of neuron-like cell system are shown and discussed, followed by a summery of the gained perceptions in chapter 5, appointed with impulses for future investigations.

Two publications [45, 46] have emerged from the scope of this work, which have been used in excerpts in subsections 4.1.1, 4.2.1, 4.3.1 and section 2.3 as well as in the abstract and this introduction.

Chapter 2

Fundamentals & Theory

2.1 Basics of Electrophysiology

2.1.1 Membrane Potential

Eucaryotic cells are functional compartments, enclosed by membranes. These membranes consist of three parts: a lipid double layer with a thickness of ~ 5 nm, which acts as a diffusion barrier for ions. The glycocalyx (40 nm), which provides communication with and protection from the environment (e.g. adverse molecules and viruses). And the spectrin-actin network, an approx. 300 nm thick mechanical stabilisator [47].

Since the intra- and extracellular space is filled with aqueous salt solutions with different ion concentrations (see Table 2.1), a potential difference between the inner and outer cell space is generated, called the “membrane potential”. Here, the intracellular solution is dominated by K^+ ions and the extracellular by Na^+ and Cl^- ions. To enable

Ion	Intracellular	Extracellular
Na^+	12 mmol L ⁻¹	145 mmol L ⁻¹
K^+	155 mmol L ⁻¹	4 mmol L ⁻¹
Ca^{2+}	10^{-8} - 10^{-7} mmol L ⁻¹	2 mmol L ⁻¹
other cations		5 mmol L ⁻¹
Cl^-	4 mmol L ⁻¹	120 mmol L ⁻¹
HCO_3^-	8 mmol L ⁻¹	27 mmol L ⁻¹
other anions	155 mmol L ⁻¹	
resting potential	-90 mV	0 mV

Table 2.1: Extra- and intracellular ion concentration, and resting potential of an eukaryotic cell. Adapted from [48].

interaction with the environment, the cell membrane is equipped with

various proteins (see Fig. 2.1). Ion channels as one example allow for ion diffusion (driven by the chemical potential difference) through the cell membrane. The example of K^+ ion transport can be used to demonstrate this process. The concentration gradient over the membrane initiates a K^+ efflux through the K^+ channel out of the cell, while the so created electrical potential difference (the intracellular space becomes more negative compared to the extracellular space) initiates a K^+ influx into the cell. When electrical and chemical potential differences achieve a balance, i.e. in- and outflow of potassium ions are the same, an equilibrium potential is established.

As for K^+ , there are also specific channels for other ions, introducing a relative permeability P_{ion} for every ion species. Therefore parts of the membrane can be seen as resistors with certain conductivities. To calculate the potential in the equilibrium state ($\sum I = 0$ for the ion currents) across the insulating membrane for a single ion species, the Nernst equation can be used:

$$E_{ion} = \frac{RT}{zF} \ln \frac{[c]_e}{[c]_i} \quad (2.1)$$

With gas constant R , absolute temperature T , charge number z , Faraday constant F and extra- and intracellular ion concentration $[c]_{e/i}$. This is also called the equilibrium potential. Considering a case with the contribution of only one ion species, the species' equilibrium potential equals its resting potential, the steady-state membrane potential. Since more than one ion species are involved, a combined resting potential has to be calculated, which is mainly determined by the K^+ equilibrium potential, although the minor Na^+ and Ca^{2+} permeabilities have to be considered as well. There are small leakage currents of

2. Fundamentals & Theory

both ions through protein transport channels and into the cell, turning the intracellular potential to more positive values and causing a K^+ efflux. These currents are driven by an electrochemical force, which is caused by the difference in membrane potential and Na^+ (or Ca^{2+} , respectively) equilibrium potential. Hence, ion pumps take effect to work against the channel diffusion, holding up the resting potential. The Goldman equation (2.2) applies, which considers internal and

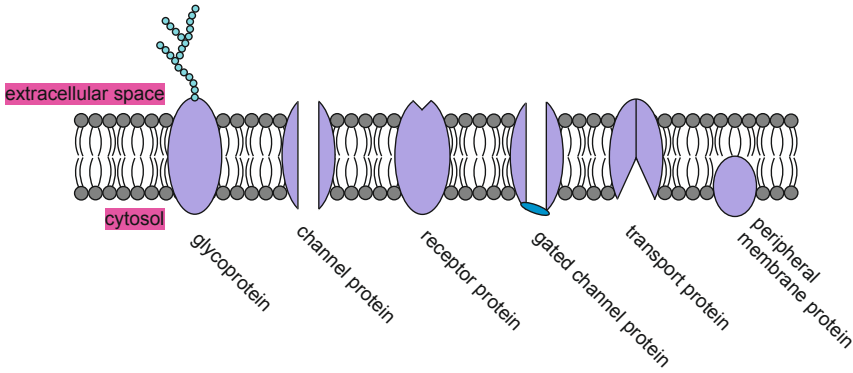


Figure 2.1: Simplified model of the cell membrane, which contains the lipid bilayer and different proteins. The ion permeabilities implemented by the channel proteins enable interaction with the cell environment.

external concentration $c_{e/i}$ and membrane permeability P_{ion} for each species and sums over the ions with the highest currents through the membrane (Na^+ , K^+ and Cl^-). It provides the membrane potential for the steady state (sum of all ion flows through the membrane equals zero), the so-called resting potential:

$$E_{rest} = \frac{RT}{F} \ln \frac{P_{Na}c_e^{Na} + P_Kc_e^K + P_{Cl}c_i^{Cl}}{P_{Na}c_i^{Na} + P_Kc_i^K + P_{Cl}c_e^{Cl}} \quad (2.2)$$

The Goldman model assumes a linear voltage drop over the membrane and a zero net current. However, that does not explain the electrical excitability and the appearance of action potentials, which will be discussed in the next paragraph.

2.1.2 Action Potentials

An action potential (AP) is a rapid and local change of the membrane potential from the resting potential of between -50 mV and -70 mV to positive values around $+30$ mV, which can propagate along the membrane and is induced by a depolarization of the cell. The initial change of the membrane potential that is referred to as depolarization can be caused by various sensory inputs to neurons with specialized receptor proteins, classified by the sort of stimuli they respond to. For instance: chemoreceptors (chemical stimuli), thermoreceptors (temperature), mechanoreceptors (mechanical stress or strain), photoreceptors (visible light), osmoreceptors (osmolarity of fluids) or baroreceptors (pressure in blood vessels). These membrane proteins alter the membrane's ion permeability when they respond to one of the mentioned influences and create a potential change. Basically, there are two kinds of potential changes: graded potentials and action potentials, both can be caused by signals from other cells or by extracellular stimulation (addressed in detail in subsection 2.4).

Opposed to action potentials, the amplitude of graded potentials is proportional to the magnitude of the stimulus (see Fig. 2.2) [49]. Graded potentials usually do not involve action of voltage-gated ion channels. In contrast to action potentials, which actively excite the neighboring membrane, gated potentials beyond the threshold decay

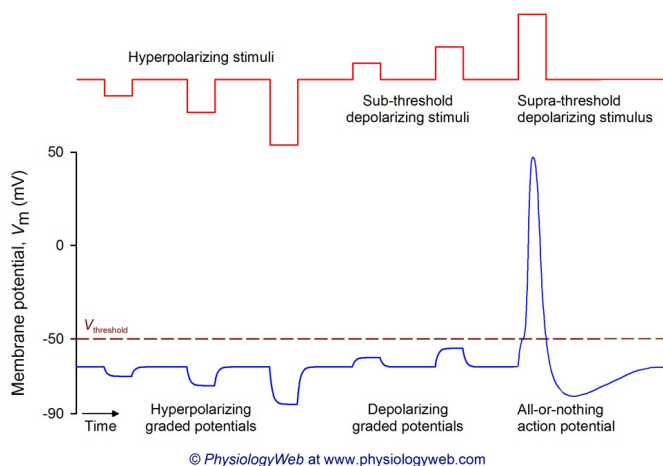


Figure 2.2: Overview about possible potential changes in excitable cells. Graded potentials can be depolarizing or hyperpolarizing, but may not reach the threshold for evocation of an action potential. Only if the threshold is exceeded, an action potential can occur. Image reprinted with permission from [49].

to the resting potential following the cable equation (see section 2.1.3) and thus represent the passive electrical property of the membrane.

Neuronal Action Potential The neuronal action potential is induced by the opening of voltage-gated Na^+ channels, when such a potential change (depolarization) reaches the threshold of between -40 mV and -50 mV [50]. Na^+ ions flow into the cell and drive the membrane potential to more positive values, towards the Nernst potential for Na^+ (approx. $+60\text{ mV}$ [48]). Next, voltage gated K^+ channels open on a slower time scale and a potassium efflux out of the cell sets in to repolarize the cell after internal dynamics of the proteins initiate closing of the Na^+ channels. Since the opening window of the K^+ channels is longer than of the fast Na^+ channels, a repolarization even

below the initial membrane potential is possible (hyperpolarization). The K^+ channels then close and the Na^+ channels stay inactivated until the resting potential is re-established again by ion diffusion and pumps (Na^+/K^+ exchanger). Then a new AP can be processed. If the depolarization does not reach the threshold, the membrane potential will return to the resting potential without generation of an AP (“all or none” principle).

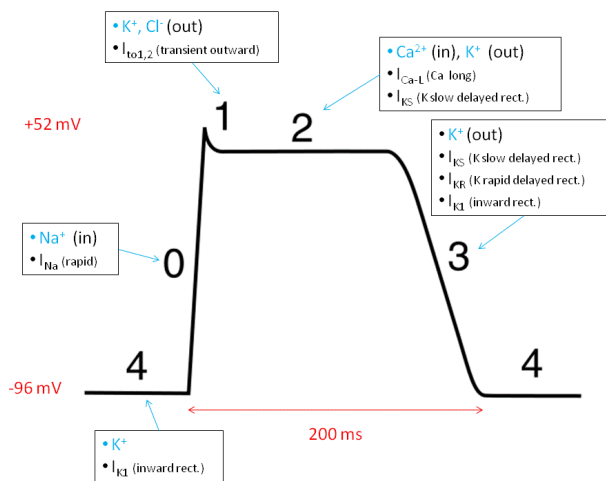


Figure 2.3: The cardiac action potential. While the neuronal AP is mainly defined by Na^+ and K^+ flows, Ca^{2+} is eminent for the cardiac AP. Re-used within the GNU Free Documentation License [51].

Cardiac Action Potential Whereas the neuronal AP is mainly defined by Na^+ and K^+ flows, for the cardiac AP Ca^{2+} is eminent. Is the cardiac cell stimulated, externally or by an adjacent cell through gap junctions, the cardiac AP starts with a steep slope in the potential course (see Fig. 2.3, phase 0), caused by fast Na^+ channels (similar to the neuronal AP). In phase 1, the fast Na^+ chan-

2. Fundamentals & Theory

nels inactivate and a minor decrease in membrane potential is caused by transient outward K^+ and Cl^- currents. In a next step, balanced (long-lasting, “L-type”) Ca^{2+} inward and (slow rectifier) K^+ outward currents result in the phase 2 potential plateau and the hence increased intracellular Ca^{2+} concentration initiates cell contraction. The Na^+/Ca^{2+} and Na^+/K^+ exchangers start to re-establish the original ion concentrations. The so-called rapid polarization phase is introduced by the inactivation of the L-type Ca^{2+} channels, while the slow rectifier K^+ channels stay open and more K^+ channels (e.g. rapid delayed and inwardly rectifying) open, restoring the potential to values around -90 mV. Then the rapid channels close, while the inwardly rectifying channels continue helping to re-establish the resting potential (phase 3 and 4). Ion pumps additionally pump out the intracellular Ca^{2+} and the contraction relaxes [51].

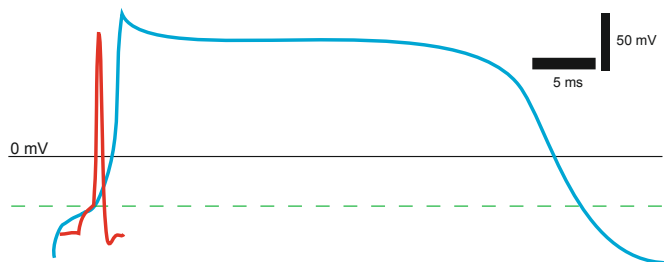


Figure 2.4: Time scale of neuronal and cardiac action potential. Due to slow Ca^{2+} channels involved in the cardiac action potential process, the cardiac AP has a much longer duration. Adapted from [52].

Pacemaker Potential In contrast to sensory neurons, some cells do not need external stimuli to generate action potentials; they depolarize spontaneously and with a regular rate. This mechanism can be found for example in cardiac pacemaker cells, located in the

sinusoidal node of the heart. Here, from a membrane potential around -60 mV, slow Na^+ channels open, producing a small, depolarizing inward current. This leads to the opening of transient (“T-type”) Ca^{2+} channels and a further depolarization of the cell. At about -40 mV L-type Ca^{2+} channels opens until the action potential threshold is reached, between 30 mV and 40 mV. Since the further depolarization is done by slow L-type Ca^{2+} channels, while T-type Ca^{2+} and Na^+ channels close, the slope of the action potential is lower than in other cardiac cells. Repolarization occurs after K^+ channels open (and L-Type Ca^{2+} channels close at the same time), providing an outward K^+ current and leading to hyperpolarization, which again is needed to activate the pacemaker channels and start the cycle again [53]. In contrast to the cardiac action potential of non-pacing cells, the AP here is caused by a large Ca^{2+} current, not the influx of Na^+ [51].

Thus, the pacemaker potential or diastolic depolarization is the potential increase during the non-contracting time between two heart beats, which is the requirement for reaching the action potential threshold. Not the fast Na^+ channels, but relatively slow Ca^{2+} channels are crucial for the generation of a pacemaker potential and the principle of spontaneously fired action potentials [54]. Due to this fact, the cardiac AP differs clearly in its temporal pattern from the neuronal AP, as can be seen in Fig. 2.4.

Hodgkin-Huxley To model the electrical behavior of the cell membrane, i.e. to find an expression for the time-dependent membrane current, the theory proposed in 1952 by Hodgkin and Huxley can be used [55]. It has been stated, that the membrane can be handled as a capacitor with the capacitance C_M . Further, the ionic concentrations can

2. Fundamentals & Theory

be presented by voltage sources, referring to the equilibrium potentials of the relevant ion species (E_{ion}). Last, the ion specific permeability of the membrane is symbolized by resistors with conductances g_{ion} . The resulting equivalent circuit (Fig. 2.5) is called “Hodgkin-Huxley element” and can be described by a differential equation, basing on the equation for the plate capacitor:

$$\begin{aligned} I &= \frac{dQ}{dt} = C \frac{dV}{dt} + V \frac{dC}{dt} \\ C_M \frac{dV_M}{dt} &= I - I_K - I_{Na} - I_L \end{aligned} \quad (2.3)$$

The ion and leakage currents I_K , I_{Na} and I_L can be calculated using the difference between membrane potential and equilibrium potential, combined with the membrane conductances g_{ion} :

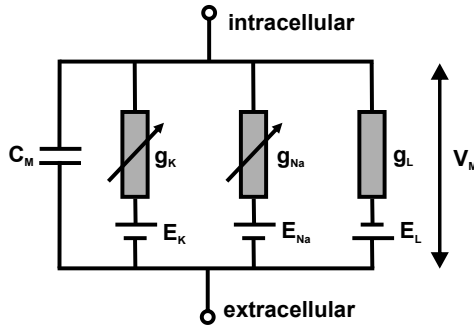


Figure 2.5: The Hodgkin-Huxley element, the cell membrane’s equivalent circuit. The membrane capacitance and the membrane permeability are represented by C_M and conductances g_K , g_{Na} and g_L , while the equilibrium potentials of the relevant ion species are considered as well.

$$\begin{aligned}I_K &= g_k(V_M - E_K) \\I_{Na} &= g_{Na}(V_M - E_{Na}) \\I_L &= g_L(V_M - E_L)\end{aligned}\tag{2.4}$$

In the end, the Hodgkin-Huxley equation for the membrane current is achieved:

$$I = C_M \frac{dV_M}{dt} + g_K(V_M - E_K) + g_{Na}(V_M - E_{Na}) + g_L(V_M - E_L)\tag{2.5}$$

2.1.3 Signal Propagation

Cable Theory To describe the signal transmission along a cylindrical cell, one can use the model of a coaxial cable, consisting of an inner conductor and an outer conductor, separated by an isolator or dielectric.

The condition for cellular signal propagation is the depolarization of the neighboring membrane parts above the AP threshold. This is done by the potential difference between the excited membrane at point x and the neighboring membrane area $x + dx$ (or $x - dx$), generating an ion current from x to $x \pm dx$. This current depolarizes the neighboring membrane. If the depolarization is sufficient to cross the threshold, Na^+ channels open and a new AP is created [48]. To model the electrical characteristics of a cylindrical cell, one can handle every membrane element dx as a parallel circuit of an ohmic resistor R_M , representing the conductivity of the membrane by different ion channels, and a capacity C_M , representing the membrane's isolating character at areas where no ion channels provide ion permeability. Since a current into the electrolyte is involved in the signal transmission, the resistance of

2. Fundamentals & Theory

the electrolyte inside and outside the cell also have to be considered: R_i (internal) and R_e (external). This results in the equivalent circuit of a coaxial cable, seen in Fig. 2.6.

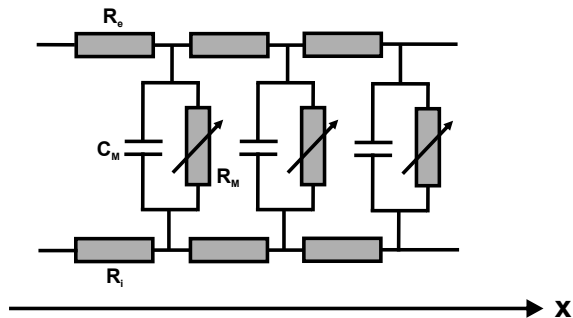


Figure 2.6: The equivalent circuit of a coaxial cable, the model for signal transmission along a cylindrical cell. The internal and external electrolyte resistance R_i and R_e is included as well as the membrane capacitance C_M and the membrane resistance R_M .

The current across the membrane can be calculated via:

$$I_M = I_C + I_{ion} = C_M \frac{\delta V_M}{\delta t} + \frac{V_M}{R_M} \quad (2.6)$$

With I_C as the capacitive current and $I_{ion} = I_{Na} + I_K + I_L$ the ionic current. Following Ohm's law, the decrease in V_M with distance can be stated as equal with the product of current times resistance [56]:

$$\frac{\delta V_M(x, t)}{\delta x} = -R_i I_i \quad (2.7)$$

R_i is the resistance of the cytoplasm and I_i the current along the axon or cylindrical cell. Further, I_i can be related to the membrane current I_M :

$$\frac{\delta I_i}{\delta x} = -I_M \quad (2.8)$$

Combining equations 2.6, 2.7 and 2.8, one gets the cable equation for the “axon cable”:

$$\lambda^2 \frac{\delta^2 V_M}{\delta x^2} - \tau \frac{\delta V_M}{\delta t} = V_M(x, t) \quad (2.9)$$

with the membrane length constant

$$\lambda^2 = \frac{R_M}{R_i} \quad (2.10)$$

and the membrane time constant

$$\tau = C_M R_M \quad (2.11)$$

Considering that velocity is basically calculated by $v = dx/dt$, the velocity of a potential wave along the membrane can be calculated *via*:

$$v = \frac{2\lambda}{\tau} = \frac{2\sqrt{\frac{R_M a}{2R_i}}}{R_M C_M} \quad (2.12)$$

The equation has been expanded with a , the fiber radius and thus the propagation velocity is proportional to \sqrt{a} .

To include a voltage-dependent membrane resistance, equation (2.9) has to be combined with the Hodgkin-Huxley equation. As the signal transmission along the cell is described by cable theory, the intercellular signal transmission is sustained by synapses, the cellular contact points.

Chemical Synapse In cells that are not directly in contact with each other, signal transmission is done via chemical synapses, which transfer incoming signals via neurotransmitter release (see Fig. 2.7a). Here, two neurons are separated by a synaptic cleft (20-50 nm) [47].

2. Fundamentals & Theory

When an electrical signal arrives at the presynaptic terminal, voltage-gated Ca^{2+} channels are activated and trigger the fusion of synaptic vesicles, which contain neurotransmitters. The neurotransmitters are released into the synaptic cleft and are detected and translated into different postsynaptic events by various receptors. For example, those postsynaptic events can be changes in the membrane potential (leading to an AP) or gene expression. The transmission speed of chemical synapses is determined by the diffusion and the reuptake of neurotransmitters [57].

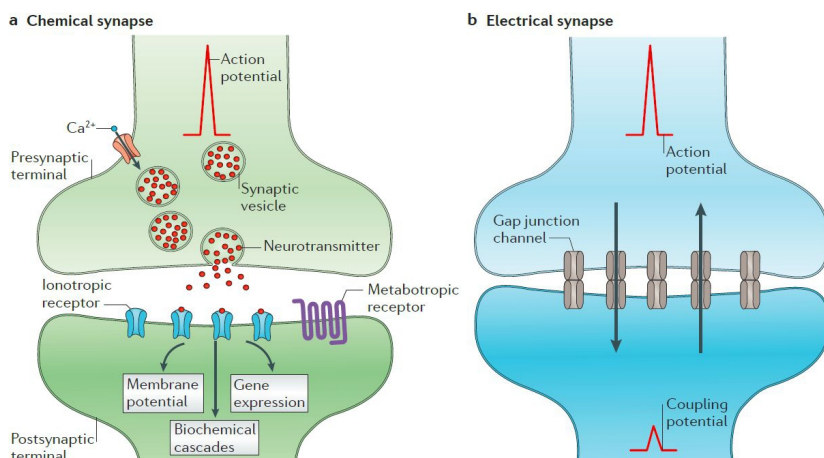


Figure 2.7: Chemical and electrical synapse. Reprinted with permission from [57]. Chemical synapses (a) transfer incoming signals via neurotransmitter release. In electrical synapses (b), cells are directly connected with each other; signals do not have to overcome a synaptic cleft.

Electrical Synapse In electrical synapses, cells are directly connected with each other; signals do not have to overcome a synaptic cleft. Therefore this connection can be seen as the above described cable transmission with a different electrolyte resistance. The cytoplasm of

the cells is connected by intercellular channels, the gap junctions (see Fig. 2.7b). These allow for direct transmission of electrical ion currents, intracellular messengers and small metabolites. Therefore electrical synapses have an insignificant transmission delay. Furthermore, in contrast to chemical synapses, they are bidirectional [57].

2.2 Cell Models for Electrophysiology

2.2.1 HL-1

As a model system for electrophysiological measurements, the cardiac muscle-like cell line HL-1 is often chosen. It was derived from an AT-1 mouse cardiomyocyte tumor by Claycomb et al. [58] and shows some valuable features for electrical recording and stimulation experiments, very similar to those of primary cardiac myocytes. The cells grow in monolayers and due to their tumoral origin, can be proliferated and cultured for a long time. They keep their phenotype over several passages and further spontaneously generate synchronized action potentials with amplitudes up to the mV range, which spread over the whole cell layer. The culture's electrical activity can be confirmed by eye due to the contraction, which is linked to the occurrence of action potentials. Therefore HL-1 cells are ideal for the first assessment of bioelectronic devices [52]. The usage of HL-1 cells suggests itself for investigation of electrical stimulation and pacing procedures as well, to conduct fundamental research for applications like heart pacemaker devices.

2.2.2 ReNcell VM

ReNcell VM is a human neuronal progenitor cell line derived from the ventral mesencephalon of human fetal neural tissue. For immortalization, the cells have been retrovirally transduced with the myc

transcription factor, which is based on the viral myelocytomatose proto-oncogene (v-myc). This leads to an increased proliferation.

This cell system was developed by ReNeuron [59] and is commercially available from Millipore. According to the distributor and Donato et al. [60] ReNcell VM shows a stable pheno- and genotype over multiple passages and, due to their multipotency, can be differentiated into glial cells and neurons. Also they are reported to differentiate into dopaminergic neurons and develop the ability to generate action potentials. Thus, this cell type represents a promising cell platform for the investigation of neuro-degenerative diseases like Parkinson's Disease (PD), as well as the modeling of neuronal networks on chip and research on intercellular communication pathways. Another advantage of using this cell line is that it achieves a neuronal-like system independent of primary cell culture and therefore avoids the use of animals.

2.3 MEAs and the Electrode-Electrolyte Interface

In the following sections, an overview over the benefits of micro-electrode array (MEA) technology as well as the theoretical foundations for understanding the interface between a system of interest and a transducer shall be given. The subsequent introducing paragraph has partly been published in [45] and [46]. Using MEA technology is the method of choice for *in vivo* and *in vitro* electrophysiological and electrochemical investigations of single cells, cell networks and tissue. MEAs provide an interesting alternative to probe-based techniques like patch clamp and carbon fiber microelectrodes, since they represent a long-term, non-invasive, highly parallelized measurement system. Cells can be cultured on MEAs up to several weeks. Due to a high spatial resolution, provided by the high number of sensor electrodes on one chip, these devices can not only perform on single cell scale, but can also be used for investigations on cell network level. Electrical extracellular recording and stimulation techniques with MEAs are well established [14, 15, 25, 61–68] and the optimization of the physical interface properties has gained growing attention in the last years [24, 28, 30, 42, 43, 69, 70]. Electrode impedance, sealing resistance between cell and sensor, electrode size and density are the most important parameters for improvement of this interface, since they correlate with the signal-to-noise ratio and the spatial resolution. A high junction resistance is coupled with low leakage currents and is therefore beneficial for signal transduction. A low sensor impedance supports a high signal-

to-noise ratio for voltage recordings and improves the charge transfer capabilities for cell stimulation.

The electrochemical electrode-electrolyte interface is crucial for medium containing cell measurements, therefore a closer look on the correlated theories will be taken. After that, the attempts in material research and sensor design by the community to improve cell-sensor coupling and electrical electrode parameters will be presented.

2.3.1 Helmholtz Double Layer

As soon as a metal is exposed to a liquid, basic concepts of electrochemistry have to be considered. In the case of extracellular MEA measurements, the interface between the electrode and electrolyte is of paramount importance, since it greatly influences the signal transmission between cell and sensor. If an electrode is immersed into an ion solution, the excess charge of the metal assembles at the surface, while in the electrolyte ions with opposite charge are attracted to the metal surface. This process is driven by the different electron energies of both media. Since an electrolyte usually consists not only of ions, but also of solvent molecules with a dipole moment, the ions are not directly in contact with the metal surface due to their solvation sheaths. Two regions of equal and opposite charge are build up and their charge distribution is known as the electric double layer, which can be modeled as a parallel-plate capacitor. Its plate distance equals $\frac{r}{2}$, with r as the free ion's radius. Since the "plate separation" is extremely small, the double layer has a high capacitance. On the metal side of the system, the charge extends over a region around 1 Å, while the region in solution is around 5-20 Å thick [71]. This is the most elementary

model to treat the electrode-electrolyte interface and was developed by Helmholtz [72, 73].

Starting from the parallel-plate capacitor view, the capacity of this so-called Helmholtz layer can be calculated with:

$$C_H = \frac{2\epsilon_0\epsilon_r}{r} \quad (2.13)$$

with relative permittivity ϵ_r , vacuum permittivity ϵ_0 and the ion radius r . Electrode and electrolyte are both handled as ideal conductors here and the capacity is assumed to be constant [71, 74]. This does not conform to real systems, therefore a more elaborate model was established.

2.3.2 Gouy-Chapman Model

In contrast to Helmholtz, Gouy and Chapman assumed the electrolyte solution to be freely diffusing point-like ions in a dielectric continuum (the solvent). Therefore the solution is not treated as ideal conductor. Electrostatic forces produce the greatest concentration of charge carriers directly at the electrode surface and thermal processes tend to randomize the charge carrier distribution. The interplay of both influences creates a diffusive layer at greater distances from the electrode surface. There, the electrostatic forces are more likely to be overcome [74]. In the following, the way to achieve an expression for the capacitance in the Gouy-Chapman model shall be sketched, orientated at the approach of Schmickler et al. [71].

2.3. MEAs and the Electrode-Electrolyte Interface

For a planar electrode, the potential can be calculated with the Poisson equation:

$$\frac{d^2\phi}{dx^2} = -\frac{\rho(x)}{\epsilon_r\epsilon_0} \quad (2.14)$$

with the charge density in the electrolyte $\rho(x)$:

$$\rho(x) = ze_0(n_+(x) - n_-(x)) \quad (2.15)$$

Here, $n_{+/-}(x)$ are the densities of cations and anions and can be calculated via Boltzmann statistics, n_0 shall be the bulk density, k_B the Boltzmann constant:

$$n_+ = n_0 \exp\left(-\frac{ze_0\phi(x)}{k_B T}\right) \quad (2.16)$$

$$n_- = n_0 \exp\left(\frac{ze_0\phi(x)}{k_B T}\right) \quad (2.17)$$

Inserting equations (2.15), (2.16) and (2.17) in (2.14) leads to the Poisson-Boltzmann equation. By applying $\frac{ze_0\phi(x)}{k_B T} \gg 1$, one can simplify to the linear Poisson-Boltzmann equation:

$$\frac{d^2\phi}{dx^2} = \kappa^2\phi(x) \quad (2.18)$$

And the Debye length:

$$L_D = \frac{1}{\kappa} \quad (2.19)$$

with

$$\kappa = \left(\frac{2(ze_0)^2 n_0}{\epsilon_r\epsilon_0 k_B T}\right)^{\frac{1}{2}} \quad (2.20)$$

2. Fundamentals & Theory

By solving 2.18 with an exponential ansatz $\phi(x) = A \exp(-\kappa x)$ and obtaining the constant A from the charge balance condition $\int_0^\infty \rho(x) dx = -\sigma$ and the Poisson's equation, this yields:

$$\phi(x) = \frac{\sigma}{\epsilon_r \epsilon_0 \kappa} \exp(-\kappa x) \quad (2.21)$$

Applied to the differential capacity $C = \delta\sigma/\delta\phi$, the capacity for the Gouy-Chapman model can be calculated:

$$C_{GC} = \epsilon_r \epsilon_0 \kappa \cosh\left(\frac{ze_0\phi(0)}{2k_B T}\right) \quad (2.22)$$

2.3.3 Gouy-Chapman-Stern Model

The Gouy-Chapman model assumes ions as point-like objects that can gain infinitely close access to the electrode surface. Therefore equation (2.22) yields to an unlimited increase of capacitance with the increase of $\phi(0)$ (not verified experimentally). This downside was addressed by Stern [75].

The ionic radius as well as the solvation sheaths and a layer of solvent on the electrode surface (see Fig. 2.8) have to be considered, leading to a so-called outer Helmholtz plane, which marks the closest ion approach. Stern treated the shortcoming of the Gouy-Chapman approach by dividing the electrode-electrolyte interface model into two parts. At low electrolyte concentrations and polarizations, the limits of the Gouy-Chapman model are negligible. At high electrolyte concentrations or larger polarizations, the ions tightly accumulate at the electrode and the Helmholtz model applies. For distances farther than the Helmholtz plane, the statistical Boltzmann approach of Gouy and

2.3. MEAs and the Electrode-Electrolyte Interface

Chapman can be used, showing that the charge in solution gathers in a diffusive ion layer. In the end, this demonstrates that the capacitance can be seen as a series network of Helmholtz parallel-plate capacitance (representing the charges at the Helmholtz plane) and differential Gouy-Chapman capacitance (representing the diffusive charge in the bulk solution) [74]:

$$\frac{1}{C_{GCS}} = \frac{1}{C_H} + \frac{1}{C_{GC}} \quad (2.23)$$

The Gouy-Chapman-Stern model still might have its weak points (i.e. effects like ion pairing and chemical interactions with the surface are neglected), but nevertheless it represents a sufficiently good model for predicting real systems.

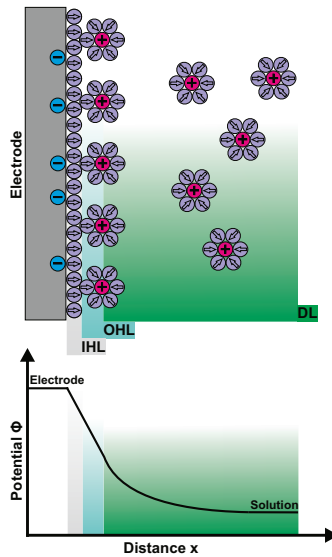


Figure 2.8: The Gouy-Chapman-Stern layer and the regarding potential function. Depicted are the inner Helmholtz layer (IHL, grey), the outer Helmholtz layer (OHL, blue) and the double layer (DL, green).

2.3.4 Butler-Volmer Equation

To complete the image of the electrode-electrolyte interface, electron-transfer reactions and their kinetics have to be highlighted. They especially count when a voltage is applied to the electrode in reference to the electrolyte's potential. To obtain an equation for the relation between faradaic current and voltage, a concept is adapted from chemical kinetics [71]:

First, the electrochemical reaction rate has to be defined:

$$\nu = k_{ox}c_{red}^s - k_{red}c_{ox}^s \quad (2.24)$$

With the surface concentrations of the reduced and oxidized species $c_{ox/red}^s$ and $k_{ox/red}$ as the rate constants. To formulate expressions for the latter, the Transition State Theory (TST) can be used:

$$k_{ox} = A \exp\left(-\frac{\Delta G_{ox}(\phi)}{RT}\right) \quad (2.25)$$

$$k_{red} = A \exp\left(-\frac{\Delta G_{red}(\phi)}{RT}\right) \quad (2.26)$$

The Gibbs energies ΔG depend on the electrode potential ϕ and the factor A is constant. Using a Taylor series around ϕ_0 and the electrostatic contribution to the Gibbs energy $F\phi$, the standard equilibrium potential for a redox reaction, leads to:

$$\Delta G_{ox}(\phi) = \Delta G_{ox}(\phi_0) - \alpha F(\phi - \phi_0) \quad (2.27)$$

with

$$\alpha = -\frac{1}{F} \left. \frac{\delta \Delta G_{ox}}{\delta \phi} \right|_{\phi_0} \quad (2.28)$$

and

$$\Delta G_{red}(\phi) = \Delta G_{red}(\phi_0) + \beta F(\phi - \phi_0) \quad (2.29)$$

with

$$\beta = -\frac{1}{F} \left. \frac{\delta \Delta G_{red}}{\delta \phi} \right|_{\phi_0} \quad (2.30)$$

α and β are the anodic and cathodic transfer coefficients. By assuming that the electrostatic potentials of the reactants are unchanged when the electrode potential is changed, it can be stated:

$$\left. \frac{\delta \Delta G_{ox}}{\delta \phi} \right|_{\phi_0} = - \left. \frac{\delta \Delta G_{red}}{\delta \phi} \right|_{\phi_0} \quad (2.31)$$

And therefore:

$$\alpha + \beta = 1 \quad (2.32)$$

Now equations (2.25), (2.26), (2.27), (2.29) and (2.32) can be combined and with the Nernst equation (2.1) the Butler-Volmer equation is obtained, providing a relation for the faradaic current density:

$$j = j_0 \left[\exp\left(\frac{\alpha F \eta}{RT}\right) - \exp\left(-\frac{(1-\alpha)F \eta}{RT}\right) \right] \quad (2.33)$$

$$j_0 = F k_0 (c_{red}^s)^{1-\alpha} (c_{ox}^s)^\alpha \quad (2.34)$$

With the current density j , the exchange current density j_0 and the overpotential $\eta = \phi - \phi_0$. At equilibrium potential, the anodic and cathodic current cancel each other, since they have the same magnitude

(j_0), but different signs. With these equations, charge transfer reactions in dependence of an applied over-potential can be estimated.

2.3.5 Surface Modifications

One of the major tasks in bioelectronics is the optimization of the devices' physical interface. Various attempts have been made to functionalize the interface between sensor and cell to achieve a better signal transmission in electrical recording and stimulation as well as chemical recordings. Hence, the attributes surface structure and sensor-cell sealing demand special attention, since the correlated parameters electrode impedance and sealing resistance strongly influence transmission (see chapter 2.4). Already the first successful MEA measurements on heart cells [76] and dissociated neurons [25] were performed with electrodes modified by platinum black, leading to establishment of the so-called "Pine Array". This sensor was developed by the Pine Lab and widely used for the investigation of neurons [77, 78]. The MEA consists of 61 electrodes in a hexagonal order, which have a diameter of $12\ \mu\text{m}$ and a pitch of $70\ \mu\text{m}$. Electroplating the electrode with platinum black increases the electrode area and thus decreases the electrode impedance, following the equations:

$$Z_C = \frac{1}{i\omega C} \quad (2.35)$$

with

$$C = \epsilon_0 \epsilon_r \frac{A}{d} \quad (2.36)$$

Z_C is the impedance of a capacitor and C the capacitance of a plate capacitor, referring to the capacitor model for the electrode-electrolyte interface.

The disadvantage of platinum black as an electrode modification is its instability, which requires a re-platinization after a certain time of use. To address this issue, mechanically stable nanoporous platinum MEAs have been developed [79]. Similar concepts have been realized with nanoporous [80] as well as “fuzzy” gold electrodes [81]. Besides platinum and gold as high conductive, biocompatible and chemical stable materials, also other materials have been investigated for targeting the need to increase electrode area on the one hand and to improve the cell-sensor contact on the other hand. One example here is the titanium nitride (TiN) electrode, which is produced by plasma-enhanced chemical vapor deposition (PECVD) under nitrogen atmosphere, resulting in a fractal deposition and therefore a nanocolumnar, rough structure [82, 83]. Further materials under development for improvement of the cell-electrode contact are carbon nanotubes (CNTs), processed by nickel or iron catalysts, electroplating or microcontact printing as well as PEDOT/polypyrrole coatings [84, 85] or combinations of polymers with CNTs, graphene or biomolecules [86–88].

Independent of the electrode material, several methods for two- or three-dimensional electrode design represent another possibility to support cell guidance, adherence and sealing by surface structuring and patterning on the nanoscale. Besides the already mentioned nanopores, nano-pillars [29, 30], -spines [31, 32] and -wires [33, 34] have been investigated, providing cell engulfment and perfusion. To include single neuron specificity, so-called neurocages have been created [35, 89]. Referring to the example of Maher et al., these neurochips are built up of a gold electrode at the bottom of a pyramidal cavity, in which the cell is immobilized. Additionally, thin tunnels are implemented to allow axon guidance and outgrowth. All these attempts suffer from

2. Fundamentals & Theory

the downside of an advanced fabrication method which implies several lithography steps.

An ideal approach for a highly functionalized device, allowing for voltammetric and amperometric cell investigations, could be realized in a combination of the presented methods of surface nanostructuring for improved electrode impedance and cell adherence, channels for guidance and outgrowth, and 3D structures like nanocages for immobilization and sealing.

2.4 Extracellular Recording and Stimulation

2.4.1 Point Contact Model

In the Point Contact Model, the interface between electrogenic cell and electrode is described by an idealized equivalent circuit, shown in Fig. 2.9. The contact between cell and electrode is simplified to one single point in the cleft with the junction potential V_J . As shown, the electrical behavior of the membrane can be calculated with the Hodgkin-Huxley model (eq.(2.5)). The cleft itself is electrically represented by the seal resistance. Aside from electrode size, density and impedance this is one of the most important parameters for on-chip electrophysiology. The sealing, i.e. the amount of signal leakage through the cleft in the surrounding medium is covered here by the inverse quantity, the junction conductance g_J . This relates to the cleft geometry [90, 91], the surface morphology, surface modification and cell type. The electrode is modeled by the electrode capacity C_E . A charge transfer resistance is not included, since faradaic processes shall not be considered here. With Kirchhoff's law, a relation between the junction potential and the intracellular potential can be set:

$$\begin{aligned} C_E \frac{dV_J(t)}{dt} + g_J V_J(t) \\ = C_M \frac{d(V_M(t) - V_J(t))}{dt} + \sum_{ion} g_{ion} (V_M(t) - V_j(t) - E_{ion}) \end{aligned} \quad (2.37)$$

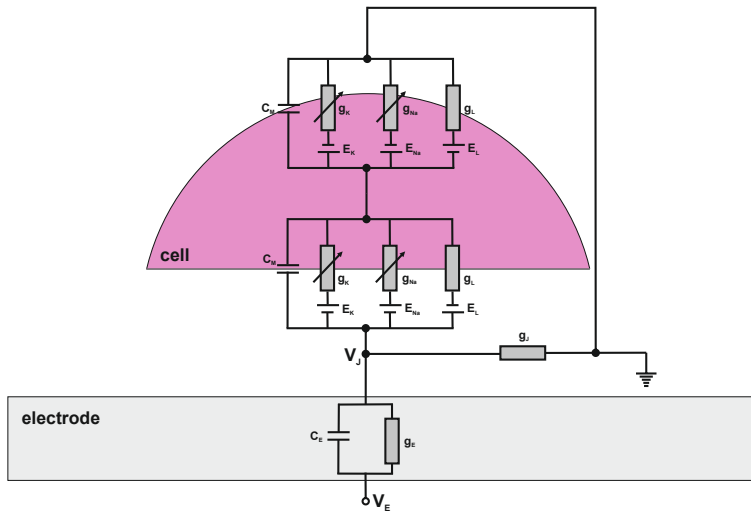


Figure 2.9: The equivalent circuit of the cell-electrode system, used in the Point Contact Model. The contact between cell and electrode is represented by a single point with the junction potential V_J . The sealing is described by the junction conductance g_J and the electrode is modeled by the capacity C_E , the conductance g_E and the potential V_E .

But assuming the capacitive electrode current to be negligible, the junction potential V_J to be small compared to the membrane potential V_M , and the ion concentration in the cleft as homogenous, the equation can be simplified to:

$$V_J(t) = \frac{1}{g_J} \left(C_M \frac{dV_M(t)}{dt} + \sum_{ion} g_{ion} V_M(t) - E_{ion} \right) \quad (2.38)$$

For modeling on a subcellular scale, the Point Contact Model should be replaced by the Area Contact Model [92, 93] with a sufficient spatial resolution at the cell-electrode interface. For the scope of the processes described in this work, the Point Contact approach is the standard model and has a satisfying accuracy.

2.4.2 Stimulation Forms

Regarding electrostimulation, first the suitable stimulation form has to be chosen. The appropriate waveform is differed between current- and voltage-controlled stimulation. In case of the first, the stimulation current is defined by the stimulation function, while the voltage is free to change corresponding the Ohm's law. In order to avoid irreversible chemical reactions at the stimulation electrode, so-called charge-balanced current pulses are used, especially in the area of deep brain stimulation. This means, that positive and negative charge, accumulating due to the anodic and cathodic current stimulation pulse, are equal:

$$\int_t I_+ dt = \int_t I_- dt \quad (2.39)$$

Nonetheless, current-controlled stimulation has the disadvantage, that the voltage for the anodic and cathodic part of the stimulation function are usually not equal and can not be exactly controlled. This means, the applied voltage can reach values that induce irreversible chemical reactions. On the contrary, in case of voltage-controlled stimulation, the voltage is defined by the stimulation function, while the current is unfixed. The voltage can easily be kept within a safe stimulation range (“water window”), avoiding gas evolution at the electrode. The obvious drawback here is that there is a lack of information about ion charge and current, which are crucial for stimulation success. Additionally, another lack is the possibility to apply charge-balanced stimulation pulses, and therefore there is the possibility that charge accumulates. However, in context of high-frequency stimulation this can be beneficial for stimulation success [68].

2.4.3 Charge Transfer

In addition to the voltage- and current-controlled stimulation mode, it also has to be distinguished between capacitive and faradaic stimulation. If capacitive stimulation is applied, there is no charge transfer between electrode and electrolyte. A potential is generated by the charges at the electrode surface, following Poisson’s law. This effects the ions in the electrolyte and leads to a current density and a counter-acting potential in the solution.

In case of faradaic stimulation, the voltage reaches values which trigger electrochemical reactions like oxidation and reduction. Charge carriers pass the electrode-electrolyte boundary. The so created faradaic

current is dependent on the voltage drop, as well as the applied electrode current and the diffusion of reagents to the electrode.

2.5 Optical Detection

As described in subsection 2.1.2, intracellular calcium is involved in action potential generation. In addition to contributing to the electrochemical potential, cellular calcium ions play an important role as second messengers in signal transduction. They trigger neurotransmitter release, regulate muscle contraction and act in processes like fertilization and cell death [94]. Therefore observation of changes in intracellular calcium concentration directly provides information about the cell functionality and it represents a possibility for indirect monitoring of action potential occurrence and propagation.

In this work, fluorescence-based calcium imaging is used to prove cell functionality in terms of electrical activity. Additionally it is combined with electrophysiological experiments to observe the cell system's response to extracellular stimulation. Especially for the latter, optical action potential detection by calcium imaging is a beneficial method, since it does not suffer electrical cross talk. This is a phenomena that usually occurs when electrical recording and stimulation is simultaneously performed and leaves the recording channel electrically "blind" for the moment of stimulation transmission into the cell system. Thus, by replacing electrical recordings by an optical method, stimulation experiments can be carried out and results can be acquired instantaneously. The technique's basic principles are described in the following, referring to Takuhashi et al. [95].

To visualize intracellular calcium, so-called calcium indicators are used. These fluorescent dyes change their emission/absorption spectra or fluorescence wavelength when binding to calcium. The indicator is brought into the cell, where it can bind to intracellular calcium. If the dye-calcium combination is now excited with a dye-specific wavelength, photons with a shifted wavelength are emitted and can be detected via microscopy and recorded with high-speed and high-sensitivity devices. Hence, a change in intracellular calcium can be associated with a change in fluorescence intensity.

In a first step, one can distinguish between two groups of calcium indicators: chemical (based on BAPTA, a calcium-specific aminopolycarboxylic acid) and genetically encoded (based on GFP, the green fluorescent protein, or variants of this) indicators. Here, the group of chemical calcium indicators is relevant, since they generally show larger signals for a given change in calcium concentration than other probes. Further criteria for classification are their ratiometric or non-ratiometric (e.g. single-wavelength) character, as well as the excitation/emission group (blue, green, yellow/orange, red/NIR) and their chemical form (salt/acid, ester, dextran conjugates). The method of choice for loading dye into the cell is dependent on the latter.

Most of the fluorescent dyes are cell membrane impermeant, therefore there are a number of techniques for dye loading into the cell: Macro- and microinjection for larger molecules, diffusion techniques and ATP-induced permeabilization are some of them. In this thesis, the dye Fluo-4 AM has been used, utilizing the so-called ester loading process. Here, the molecule's carboxylic group is modified with an acetoxymethyl (AM) ester group, leading to an uncharged complex that is able to pass through the cell membrane. Within the cell, the

AM ester group is cleaved by esterases and the charged form of the dye becomes trapped in the cell [96].

Another characteristic influencing the calcium indicator choice is the dissociation constant K_D , which represents the calcium binding affinity. The best calcium sensitivity is achieved below and near K_D . High-affinity dyes can yield high fluorescence intensity, but also saturate at quite low calcium concentrations and tend to buffer intracellular calcium. This can lead to inaccuracies in estimation of calcium concentration. Low affinity dyes are advantageous for calcium investigation on a subcellular scale and rapid concentration changes, since their reaction kinetics are fast enough to cover high temporal resolution events.

For a qualitative measure of the intracellular calcium concentration, a pseudo-ratio $\Delta F/F_0$ can be used [97]:

$$\frac{\Delta F}{F} = \frac{F - F_{base}}{F_{base} - B} \quad (2.40)$$

with the change in fluorescence ΔF , the measured fluorescence intensity of the indicator at the start of the experiment F , the background intensity B and F_{base} the intensity before stimulation, i.e. before calcium increase. $\Delta F/F$ is thought to approximate the intracellular calcium concentration. With this approach, differences of indicator concentration between cells can be normalized [98].

Chapter 3

Materials & Methods

3.1 Device

3.1.1 Planar MEA

Planar micro-electrode arrays (MEAs, see Fig. 3.1) were produced in-house in the clean-room of the Helmholtz Nanoelectronic Facility (HNF) Jülich or the Center of Advanced European Studies and Research (caesar), Bonn. As previously described [22, 46] a 4-inch borosilicate wafer was structured by standard photo-lithography. The fabrication scheme is depicted in Fig. 3.2.

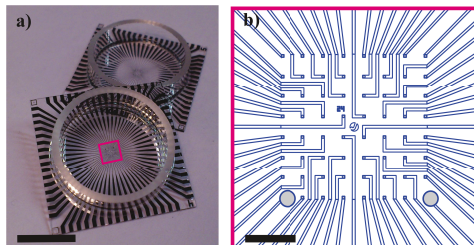


Figure 3.1: a) Micro-electrode array (MEA) with glass ring for cell culture applications. b) Electrode and feedline design of the active area in the chip center. At the end of every feedline a circular electrode is located, creating a 8×8 pattern. Blueprint by M. Banzet.

A double-layer resist (LOR 3b, Microchem, Newton, MA and AZ nLOF 2070, MicroChemicals, Ulm, Germany) was used to define the electrode area and the respective feedlines. This 8×8 square array pattern can be seen in Fig. 3.1b. After development of the resist structure, a metal stack of Ti/Pt/Cr or Ti/Au/Cr was deposited by electron beam. In a subsequent lift-off step, the metal structure was defined. The chip was passivated using an overall 800 nm thick stack of five alternating SiO_2 (200 nm) and Si_3N_4 (100 nm) layers

(ONONO) or an approx. 2 μm thick polyimide layer (PI), fabricated by plasma enhanced chemical vapor deposition (PECVD, at 280 $^{\circ}\text{C}$) or a spincoating process, respectively. On this passivation, a second photolithography was performed and the structured resist was used to introduce a circular opening into the passivation layer on top of the electrodes and to open the bond pads by reactive ion etching (RIE). This defines in the end the electrode area later exposed to the electrolyte. For the metal stack the Ti layer serves as adhesion material between borofloat surface and electrode materials (Au or Pt), whereas the Cr layer promotes the adhesion between electrode metal and ONONO passivation and serves additionally as sacrificial layer. The cavity production by utilization of the Cr layer will be described in the next subsection. The chip dimensions are 1 inch \times 1 inch, with 28 μm wide (in the center region) feedlines, electrode openings of 12 or 24 μm and center-to-center distance (pitch) between the electrode openings of 200 μm .

For applications not related to cell culture, like investigation of the chrome etching process (see subsection 3.1.2), impedance spectroscopy or microscopy, MEAs with the same design and composition but a smaller size of 11 mm \times 11 mm and electrode openings with a diameter of 3, 8, 10, 15 and 20 μm were also used.

3.1.2 Sacrificial Layer Etching

In a last production step, the nanocavities were fabricated by removing the chromium adhesion layer to an adjustable length along the electrode feedline (Fig. 3.2d). The resulting reservoir between electrode and passivation layer is defined by the feedline width and the

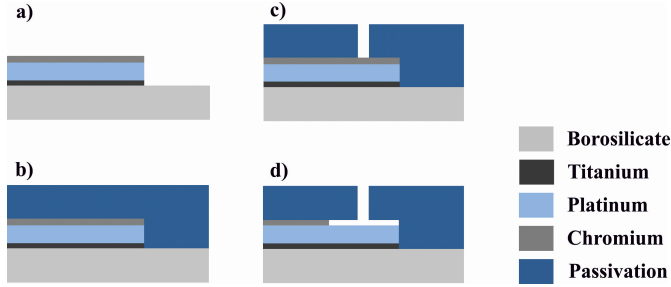


Figure 3.2: Schematic fabrication steps of a Pt nanocavity array. First Ti/Pt/Cr feedlines were deposited on a borofloat wafer (a). A stack of alternating silicon oxide (200 nm) and silicon nitride (100 nm) layers was deposited to passivate the device (b) and opened by reactive ion etching (c). The cavities between passivation and electrodes were fabricated by wet etching of the chromium layer (d). Published in [45] and reproduced by permission of Wiley-VCH.

length of the back-etched feedline as well as the afore chosen thickness of the chromium adhesion layer. The chromium etching was executed with a commercially available chromium etch solution (Chrome Etch No. 1, MicroChemicals) on basis of ceric ammonium nitrate ($(\text{NH}_4)_2[\text{Ce}(\text{NO}_3)_6]$) and perchloric acid (HClO_4) and has the following composition: 10.9% ceric ammonium nitrate, 4.25% perchloric acid and 84.85% H_2O . Ceric ammonium nitrate is a strong oxidizing agent and therefore provides the main reaction in the etching process:



The oxidation state of Ce is reduced from IV to III and the oxidation state of Cr is increased from 0 to III. Perchloric acid serves as chemical stabilizer for ceric ammonium nitrate. At the beginning of the etching process, a black film on the electrode opening can be observed. This

can be identified as chromium nitrate, which is reported to be steadily produced during etching [99], but dissolves in the aqueous etchant.

The etch rate was determined to 7 $\mu\text{m}/\text{min}$, measured on a MEA with 80 nm chrome layer and 24 μm electrode opening [46], approaching a square-root dependence of time for long-time scales ($x \sim \sqrt{t}$). The etching process was controlled optically and stopped by transferring the sample to a water bath, rinsing it for several minutes.

3.1.3 Surface Structuring by Inter-diffusion

Interdiffusion is a well known and documented phenomenon [100–108] which represents the migration of two atom species from separated areas into each other. Here, it mainly describes the migration of the electrode (Au or Pt) and sacrificial layer material (Cr), respectively. After removing the chromium layer, a rough nanostructure is revealed. For an Au/Cr system it is known that the process of atomic diffusion is temperature dependent and needs a certain activation entropy to be triggered. Diffusion of crystalline solids can be interpreted as jumps of individual atoms. The reason for diffusion is a decrease of the Gibb's free energy of the system and the driving force is the chemical potential (atoms diffuse from high potential areas to low potential areas) [108].

3.1.4 Gold Interdiffusion Samples

For a targeted investigation of gold interdiffusion on a large scale, unstructured gold samples were fabricated in a clean-room environment. For this, a 4-inch silicon wafer was oxidized and metalized

with a stack of Ti/Au/Cr (10 nm/200 nm/100 nm). Subsequently, the wafer was cut into 7 mm × 7 mm pieces. To reveal the temperature dependence of the surface structuring procedure by interdiffusion, the samples were treated in a furnace with different annealing temperatures (100 °C, 200 °C, 300 °C, 400 °C, N=5 for each temperature) for two hours without ramping and compared to unheated samples (20 °C, N=5). The chromium layer was removed by wet etching and the samples were washed before characterization by different microscopy methods, impedance spectroscopy and contact angle measurements.

3.2 Characterization

3.2.1 Electrochemical Impedance Spectroscopy

When considering AC circuits, there are two main entities which have to be taken into account: Inductance (caused by voltages induced by the magnetic fields of currents) and capacitance (electrostatic storage of charge induced by voltages between conductors) [109]. To apply the concept of resistance to AC circuits, impedance is introduced as a quantity which represents magnitude and phase difference between the voltage and current response.

Sensor impedance is an important parameter in bioelectronics, especially to evaluate the performance of devices interfacing cells and tissue. Low-impedance electrodes support a high signal-to-noise ratio and are therefore indicator for a good signal transmission in recording

applications. Further, a low impedance is beneficial for the charge transfer capabilities in cell stimulation.

In electrochemical impedance spectroscopy (EIS) a small AC voltage signal $v(t) = V_m \sin(\omega t)$ with voltage amplitude V_m is applied to the system of interest and the resulting steady state current $i(t) = I_m \sin(\omega t + \vartheta)$ with the current amplitude I_m and phase difference ϑ is measured [110]. Equivalent to the ohmic behavior of a DC system, the impedance can then be defined as the relation between AC voltage and current:

$$Z(\omega) = \frac{v(\omega, t)}{i(\omega, t)} = \frac{V_m \sin(\omega t)}{I_m \sin(\omega t + \vartheta)} \quad (3.2)$$

The magnitude is here $|Z| = |V_m|/|I_m|$. Hence, impedance is a more general concept and the ohmic resistance can be seen as impedance with zero phase angle. A phase difference of zero can be interpreted as purely resistive behavior while the capacitive characteristics of an electrode in an electrolyte causes a certain phase shift of 90° . Mathematically the properties of magnitude and phase can be combined in the representation of Z as an imaginary vector quantity:

$$Z = Z' + iZ'' = |Z| \exp(i\vartheta) \quad (3.3)$$

The real value and the imaginary value can be identified with the resistive impedance $Z_R = R$ (since an ideal resistor is purely real) and the purely imaginary reactive impedance of inductor or capacitor: $Z_L = i\omega L$ and $Z_C = \frac{1}{i\omega C}$, with the inductance L and the capacity C . The impedance for the system of interest in this thesis consists dominantly of resistive impedance and capacitive reactive impedance

3. Materials & Methods

and is hence expressed by:

$$Z = R + \frac{1}{i\omega C} \quad (3.4)$$

The impedance data within this work were measured with a Biologic VSP300 potentiostat and is graphically presented in a Bode plot. This is usually a combination of a Bode magnitude plot (representing the system's frequency response) and the Bode phase plot (representing the phase shift). For clarity, the phase data plot was renounced here. For extracting the sensor capacitance from the measured impedance data, the electrode-electrolyte interface as the electrochemical system of interest was emulated by an equivalent circuit (see Fig. 3.3) containing an ohmic resistor (modelling the electrolyte resistance R_e) in series with a ohmic resistor and a capacitance in parallel (modelling the charge transfer resistance R_{ct} and the Helmholtz double layer capacitance C_{dl}).

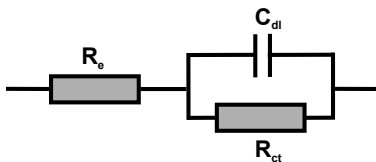


Figure 3.3: Equivalent circuit for determination of the sensor capacity from impedance data. R_e represents the electrolyte resistance and is in series with the charge transfer resistance R_{ct} and the double layer capacitance C_{dl} .

3.2.2 AFM

The Atom Force Microscope (AFM) was introduced in 1986 by Binnig et al. as a combination of scanning tunneling microscope (STM) and profilometer [111]. With AFM, both insulators and conductors can be investigated non-destructively. The main elements of an AFM are the AFM tip (usually made of silicon or silicon nitride and with a dimension in the nanometer range), the so-called cantilever (carrier of the tip), a light source and a photo-detector (see schematic image in Fig. 3.4). The core mechanism of this technique is the determination the atomic forces between tip and sample surface. This forces cause deflection or oscillation of the AFM tip, which is measured via a laser focused on the cantilever and reflected to a photo-detector. The force on the tip can then be calculated with a relation between force F and deflection in z direction Δz :

$$F = k\Delta z \tag{3.5}$$

With k being the spring constant, describing the characteristics of the oscillating cantilever. It is dependent on geometry and material and has a dimension of 1 N m^{-1} [112]. Therefore forces of several pN or even in the fN range can be measured. From the changing force on the AFM tip, the distance to the surface can be concluded and thus the topography is imaged. The AFM has several operation modes. To map the surface structure of Au and Pt nanocavity arrays and to estimate the sample's roughness, a Bruker Nanoscope V Multimode has been used in the tapping mode. Here, a tip oscillation near the tip's resonance frequency is generated by a piezoelectric element. The

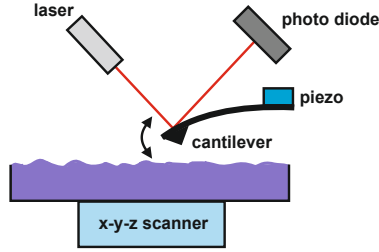


Figure 3.4: Schematic display of the AFM working principle in the tapping mode. The force between AFM tip and sample surface is determined by measuring the deflection of the tip.

resonance frequency is defined as:

$$f_0 = \frac{1}{2\pi} \left(\frac{k}{m} \right)^{\frac{1}{2}} \quad (3.6)$$

It becomes clear, that mass and spring constant are the defining parameters and the tip is the crucial element. In order to reach the maximal deflection for a given force, a low k is necessary and to minimize environmental noise, a high resonance frequency is aspired. This is gained by a low k tip material. The low k is then combined with a small tip mass, resulting in a large k/m ratio [111]. Here, a Bruker RTESPA-300 tip was used, made of antimony doped silicon, with a spring constant of around 40 N m^{-1} and a resonance frequency of approx. 300 kHz. With decreasing distance between tip and sample, the amplitude decreases due to forces like van der Waals forces, dipole-dipole interactions and electrostatic forces. The cantilever amplitude is maintained constant by height adjustment and the force of the intermittent contacts between tip and sample surface is mapped [113].

3.2.3 SEM

Scanning electron microscopy (SEM) is a technique to image the surface topography of a specimen by scanning with a focused electron beam. A detailed description is given in the book of Goldstein et al. [114], which served as guideline for the following short overview. SEM basically consists of an electron gun, two or more electron lenses, a deflection system and an electron detector (see simplified scheme in Fig. 3.5a). The electron gun is a source of electrons, which are accelerated to an energy in the range of 1-40 keV. To achieve a sharp image with high magnification, the beam is focused on the sample surface by electron lenses. Next, the electron beam leaves the last lens, enters the specimen chamber and falls onto the sample surface, where it interacts within a depth of approx. 1 μm . The two main signals of these process are secondary electrons and back-scattered electrons, induced by the accelerated electrons of the electron beam. These electrons are collected by the electron detector, consisting of a positively charged wire mesh screen, a scintillator, a light pipe and a photomultiplier tube. After being attracted by the charged screen, the electrons get converted by the scintillator into light, which again is transformed into an amplified electrical signal by the photomultiplier. For image formation a scanning system is needed, represented by the deflection system. This contains two pairs of electromagnetic coils, which are used to control the beam position, leading to a rectangular scanning raster. When scanning the sample surface, variations in signal intensity occur, creating an image on the viewing screen. The magnification is set by reducing or extending the area size scanned by the scan coils. Here, a Zeiss Gemini 1550 system was used to image

3. Materials & Methods

the surface topography of nanostructured Au layers and cavity devices.

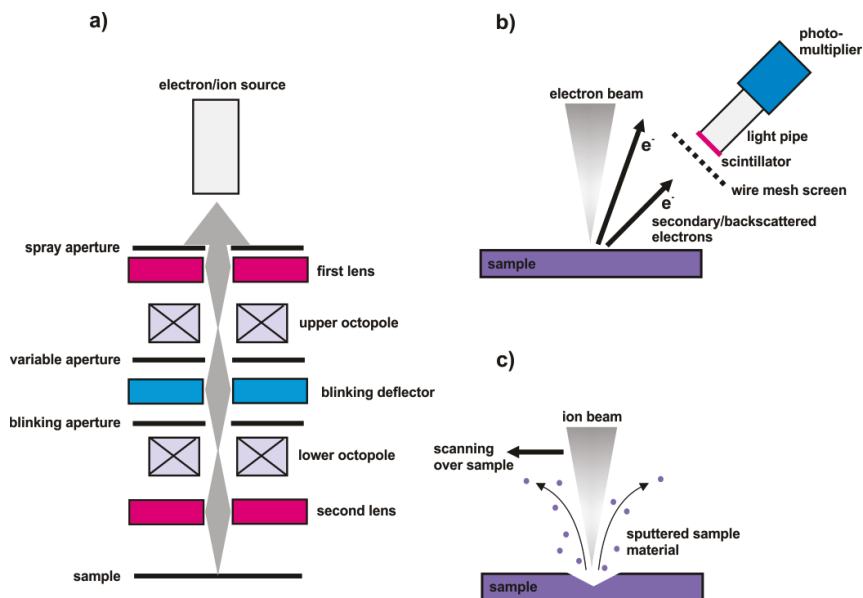


Figure 3.5: a) Schematic display of the FIB/SEM construction. The electron (SEM) or ion (FIB) source is focused by several apertures and lenses on the sample surface. b) SEM working principle: the electron beam causes secondary and backscattered electrons, which are detected by a scintillator. c) FIB working principle: The focused ion beam abrades material out of the sample surface.

EDX To perform elemental composition analysis, energy-dispersive x-ray spectroscopy (EDX) was used. This technique bases on the x-ray excitation of the sample surface and is usually combined with a SEM system. Each chemical element has a unique structure and therefore a unique x-ray emission spectrum. The electrons of an atom within the sample are distributed in discrete energy levels, so-called electron shells. The high-energy electron beam also used for SEM

excites an electron from a inner shell and increases its energy to leave the atom, leaving behind an electron hole. This hole can be filled by an electron from an outer, higher energetic shell. The excess energy of this transition is emitted in form of x-rays, which are characteristic for the emitting element and its atomic structure [115]. The resulting radiation is measured by a energy-dispersive spectrometer, resulting in a sample specific spectra which depicts emission peaks for the elements contained in the investigated sample. The penetration depth and thus the lateral resolution is dependent on the primary electron energy E_0 and the energy of the excited electron shell E_c , as well as the material density ρ [116]:

$$Z_m = 0.033 \frac{(E_0^2 - E_c^2)}{\rho} \quad (3.7)$$

The EDX analysis within this thesis was performed with a Magellan 400 SEM-FEI system and the penetration depth for Au and Cr ranges around 0.5 μm .

FIB The core element of a focused ion beam (FIB) system is the ion column (see Fig. 3.5a), which is similar to the electron beam column of a SEM. The main difference is the use of a gallium ion (Ga^+) beam instead of an electron beam. The ion beam is generated by a strong electric field applied to a liquid metal ion source. Here, a liquid gallium cone is formed on top of a tungsten needle and treated with an excitation voltage of around 7 kV. The emitted ion beam is focused by electrostatic lenses and beam stigmatism is balanced by an octopole. The beam current is varied with an aperture mechanism and ranges between 1 pA and 10 nA for different applications like low-current FIB imaging and high-current FIB milling. The ion beam energy ranges between 10 and 50 kV.

FIB milling, the technique used here for FIB cross-sectioning of cells on nanocavity arrays (with a FIB Helios 600), bases on sputtering of neutral or ionized substrate atoms. A high ion current beam is focused on the sample surface, resulting in a physical sputtering of surface material (see Fig. 3.5b). The etch rate depends on the scanning style, possible material redeposition and the angle of incidence. A more detailed overview about FIB techniques can be found in [117] and [118].

3.2.4 Contact Angle Measurement

The contact angle of a liquid drop on a solid surface is directly related to the three surface tensions of the solid-liquid, solid-vapour and liquid-vapour interface. In mechanical equilibrium, this relation is given by the Young equation [119]:

$$\gamma_{lv}\cos\theta_Y = \gamma_{sv} - \gamma_{sl} \quad (3.8)$$

θ_Y is here the Young contact angle and a schematic of the system is shown in 3.6. The contact angle can be determined by a tangent of the liquid drop at the surface base. To gain an accurate fit of the drop shape and the contact angle, several methods are in use. The best fit is a numerical integration of the Young-Laplace equation, referring to literature [119, 120]. The Laplace-Young equation provides a relation between drop radii of a curved area r_1 and r_2 , surface tension γ_{lv} and pressure difference across the curved liquid surface Δp :

$$\Delta p = \gamma_{lv} \left(\frac{1}{r_1} + \frac{1}{r_2} \right)$$

The accuracy for the fit is better than $\pm 0.3^\circ$ [120]. Contact angle measurements on plane and structured gold surfaces have been performed with a Data Physics OCA20 contact angle measurement setup and the Laplace-Young contact angle fit was performed automatically by the belonging Data Physics software.

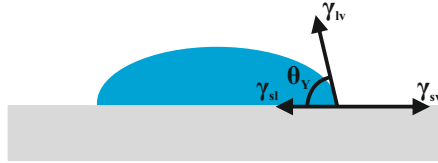


Figure 3.6: To determine the contact angle, a liquid drop is placed on the surface and a tangent is set at the drop surface base. The contact angle is a measure for the surface tensions of the solid-liquid (γ_{sl}), solid-vapour (γ_{sv}) and liquid-vapour (γ_{lv}) interface.

3.3 Cell Culture

3.3.1 HL-1

As previously described [45, 46, 121], cardiomyocyte-like HL-1 cells (see Fig. 3.7) were cultured in T25 culture flasks in a humidified atmosphere at 37°C and $5\% \text{CO}_2$. Cells were maintained in Claycomb medium with $10\% \text{FBS}$, $100 \mu\text{g mL}^{-1}$ Penicillin and 100U mL^{-1} Streptomycin (PenStrep), 2mM L-glutamine [58] (all from Life Technology) and 0.1mM norepinephrine (Sigma), and split after reaching confluency, approx. two times per week. For splitting, 1mL of a Trypsin/ethylenediaminetetraacetic acid (EDTA) solution was applied,

3. Materials & Methods

5 mL Claycomb medium was added and the cell suspension was centrifuged for 5 min at 500 g. The resulting cell pellet was then resuspended in 1 mL media and a certain cell amount was taken off for sample preparation. The rest of the cells was re-plated for further maintenance. The cells in the confluent cell layer form gap junctions and begin to send action potentials through the cell sheet. With further maturation, the cells develop contractive behavior and action potentials can be confirmed by observing cell movement.

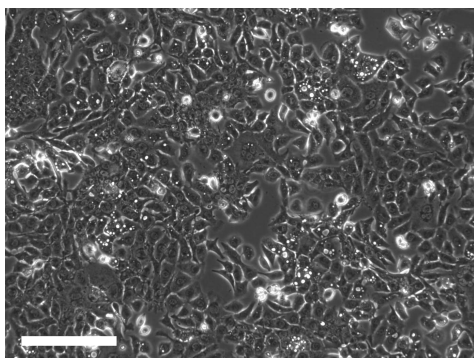


Figure 3.7: HL-1 cells in an almost fully confluent monolayer. In this state, gap junctions are formed and the cells start contraction. Scale bar: 200 μm .

Sample Preparation After post-processing (cavity etching, placing of glass culture rings), MEAs were thoroughly washed with MilliQ water to remove etching residues as well as dust particles and other impurities. After drying with nitrogen, chips were prepared for cell culture applications. First a sterilization with UV light (20-30 min) was done in order to avoid bacteria or yeast contamination and subsequently, the chip surface was coated with an adhesion mediating protein. Here, MEAs were incubated with a sterile solution

of $5 \mu\text{g mL}^{-1}$ fibronectin and $0.02 \mu\text{g m}^{-1}$ gelatin for one hour at room temperature. After formation of the protein layer, the device was washed two times with sterile MilliQ water. HL-1 cells were plated in a sufficient density, aiming to achieve a confluent cell layer after 3-4 days *in vitro* (DIV). When the cells reached confluency, electrophysiological measurement were carried out.

For FIB sectioning, HL-1 cell were plated on nanocavity arrays, fixed and dehydrated like described in literature [122]. For that, cells were washed two times with pre-warmed PBS and chemically fixed with a solution of 3% glutaraldehyde in PBS for 20 min at room temperature. Glutaraldehyde was removed and cells were washed with PBS (1x) four times. Dehydration was carried out by placing the samples for 5 min at a time in a concentration cascade of ultra-pure ethanol (10%-100%). The samples were stored in 100% ethanol until being dried by critical point drying (CPD).

CPD was performed with established parameters: 70% ethanol was used as agent and after cooling to 10°C , the medium was exchanged 10 times with liquid CO_2 . After the ethanol was replaced mostly by CO_2 , the CPD chamber was heated to 39°C , above the critical temperature point of CO_2 at atmospheric pressure (35°C). Reaching the critical temperature, a transition from liquid to vapour happens, without a change in density. Therefore, the sample is not damaged by surface tension during this drying method. In the end, the pressure was slowly decreased to atmospheric pressure. To prepare for SEM/FIB investigations, the samples were sputtered with iridium to provide a conductive area on the organic cell material. Additionally, the structure of interest was covered with platinum, before performing the FIB cut.

3.3.2 ReNcell VM

ReNcells VM (see Fig. 3.8a) were initially cultured following the standard maintenance protocol by Millipore [123]. For this, a T25 culture flask was coated with laminin to improve the cell adhesion. This was done by incubating $20 \mu\text{g mL}^{-1}$ laminin solution at 37°C for at least four hours or overnight. The culture flask was washed with medium one time, before plating the cells. Culture medium was prepared by adding fibroblast and epidermal growth factors (FGF and EGF, each 20 ng mL^{-1} medium) as well as PenStrep ($10 \mu\text{g mL}^{-1}$) to Millipore's ReNcell NSC Maintenance Medium. When reaching 80% confluency, the cells were splitted by the Trypsin/EDTA induced enzymatic process. Differently from HL-1 culture, cells were centrifuged at 300 g before re-plating. For differentiating the cells towards neuronal fate, three protocols were tested, which are described in the following.

Millipore Differentiation The addition of FGF to the ReNcell maintenance medium supports cell proliferation, while EGF supports the dopamine-induced proliferation. According to the Millipore protocol, differentiation (see differentiated ReNcells in Fig. 3.8c) is initiated by withdrawal of growth factors. Therefore, the medium was exchanged with growth factor-free maintenance medium, supplemented only with PenStrep. Millipore recommends a differentiation period of two weeks with a media change every 2-3 days. Donato et al. [60] report rounded cell bodies with extensive neurite outgrowths after 4 days with this differentiation method and identified neurons, astrocytes and oligodendrocytes with immunocytochemistry after finalizing the

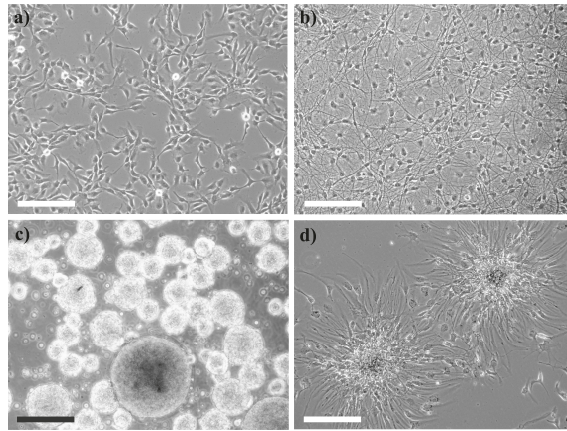


Figure 3.8: ReNcell VM in the undifferentiated (a) and differentiated (b) state. When differentiating, small and round cell bodies are formed and neurite outgrowth sets in. ReNcells are able to form neurospheres (c), which migrate after transfer to a laminin-coated surface (d). Scale bars: 200 μm .

protocol. Here, cells were differentiated two weeks minimum before immunostainings were performed.

Neurospheres Neural stem cells are able to grow as neurospheres, free-floating clusters of cells. Donato et al. [60] presented an extension of the standard Millipore differentiation protocol by culturing ReNcells first as neurospheres, before applying the Millipore protocol. This differentiation protocol is also documented elsewhere [124, 125] and has been tested within this thesis. For that, cells were cultured for several days in standard maintenance medium on uncoated culture ware. Subsequently, neurospheres formed (see Fig. 3.8c and d) and were transferred to laminin-coated samples, before the Millipore differentiation protocol was induced.

Heparin Supported Differentiation Choi et al. [126] demonstrated differentiation of ReNcell VM into neuronal and glial cells within three weeks following a heparin-based differentiation protocol. Heparin is reported to support neuronal and dopaminergic differentiation [126] as well as to activate Wnt signaling for neuronal morphogenesis [127], therefore this protocol was chosen as one alternative to the standard differentiation protocol by Millipore. The heparin differentiation medium was compounded as following: 5 mL DMEM F12 without Glutamax was supplemented with 2% (v/v) B27 without vitamin A (Life Technologies), $2\ \mu\text{g mL}^{-1}$ heparin (Stem Cell Technologies) and 1% (v/v) PenStrep. ReNcell have been differentiated for 21 days with a medium change every 2-3 days.

Co-factor Induced Differentiation This differentiation protocol bases on the work of Kirkeby et al. [128], who developed a differentiation procedure to achieve neuronal cells from human embryonal stem cells. This protocol was adapted to the ReNcell VM system. Here, the differentiation period of 21 days can be divided into three phases and is documented in detail in [129]. In the first phase (day 0-4), a base medium made of DMEM F12 medium (24 mL), neurobasal (NB) medium (24 mL), N2 supplement (1:100) and 0.5% PenStrep ($1\ \text{mg mL}^{-1}$, 500 μL), 1 mL B27 without vitamin A (1:50) was used for cultivation. On the first two days, $10\ \mu\text{M}$ medium rock inhibitor (Y-27632, Tocris Bioscience) was added to the culture medium.

In the second phase (day 4-11), the concentrations of the base medium components were changed to: 24.1 mL DMEM/F12, 24.1 mL NB medium, N2 supplement (1:200), 0.5 % PenStrep and B27 without vitamin A (1:100). The medium was changed every two days, without

rock inhibitor. In the third phase (day 11-21) the base medium was prepared as following: 48.2 mL NB medium, B27 without vitamin A (1:50), 333 μL ascorbic acid (0.2 mM) and 0.5% PenStrep. Here, with every medium change 20 ng mL^{-1} brain-derived neurotrophic factor (BDNF) and 10 ng mL^{-1} glial cell line-derived neurotrophic factor (GDNF) was added. Additionally, from day 14 on 0.5 mM dibutyryl-cAMP (db-cAMP) was added with every medium change.

Sample Preparation For on-chip applications, ReNcell VM were plated on laminin coated MEAs or nanocavity arrays. The chips have been treated with an O_2 plasma (5 min, 1 mbar, 80 W, Diener PICO), for cell adhesion supporting surface cleaning and activation. Within the scope of this thesis, a better compatibility of PI passivated devices with differentiating ReNcells has been revealed, compared to differentiation on ONONO passivated devices. Fig. 3.9 shows differentiating ReNcells on a PI chip (left) and on an ONONO chip (right). For long term-culture, the PI surface seems to provide better adhesion and cell viability, while the cells form bundles and detach after several days on the ONONO surface. This might be due to a different interaction of the adhesion protein laminin with the surface. Immunostainings have been carried out on flame-activated glass coverslips and will be described in the following subsection.

3.3.3 Immunofluorescence Analysis

The antibody-based method of immunofluorescence staining is widely used to detect specific cell proteins. Indirect immunofluorescent labelling was performed on differentiated ReNcell VM to evaluate the differentiation process. In this technique, cells are incubated with a

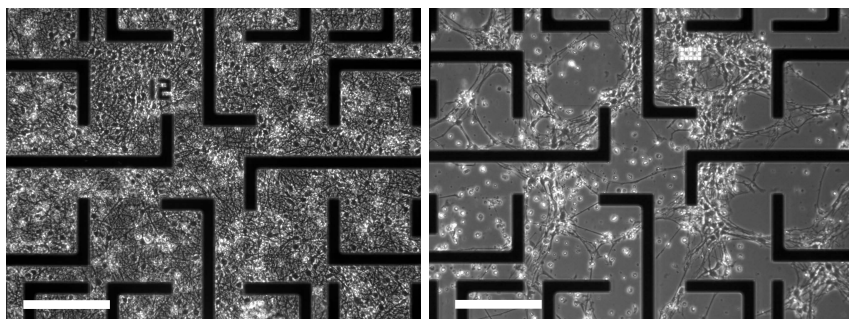


Figure 3.9: Differentiating ReNcells on a PI passivated chip (left) and an ONONO passivated chip (right). While on PI a homogenous and dense cell layer is provided, cells detach and form bundles after several days on ONONO. Scale bars: 200 μm .

primary antibody, which binds to the target protein. Then, a second antibody is used, which carries the fluorochrome with a specific emission wavelength. This binds to the first antibody and thus, the protein of interest can be identified by the emission color in fluorescence microscopy. For immunifluorescent stainings cells were cultured and differentiated on laminin coated glass coverslips. First, a cross-linking fixation method was applied to the cell samples, leading to intra- and inter-molecular covalent bonds between amino-containing groups, which stabilizes the cell structure. Here, cells were rinsed three times with pre-heated PBS ($1\times$) and fixed with 4% paraformaldehyde (PFA) for 15 min at room temperature. Subsequently, the samples were washed again three times with PBS ($1\times$). To permeabilize the cell membrane for cell-impermeable antibodies to reach the antigens, cells were treated for 15 min with a permeabilization solution (0.3 % Triton X-100) at room temperature. After washing again, blocking of unspecific bonding sides was performed over night by incubation with 1% BSA and 2% goat serum in PBS at 4 $^{\circ}\text{C}$ or for one hour at

room temperature. The next day, primary antibodies were added: Microtubule-Associated Protein 2 (MAP2, rabbit host, Millipore) in a 1:500 dilution in 0.5 % BSA/PBS solution (1×) and tyrosine hydroxylase (TH, chicken host, Neuromics) in a 1:200 dilution in 0.5 % BSA in PBS (1×). The samples were incubated for 2 hours at room temperature in a wet chamber, before being washed and second antibodies were added with 4',6-diamidino-2-phenylindole (DAPI, dilution 1:500): Alexa Fluor 488 goat anti-chicken (1:1000, Life Technologies) to bind to the primary TH antibody and Alexa Fluor 546 goat anti-rabbit (1:1000) for the primary MAP2 antibody (Life Technologies). Subsequent incubation of one hour at room temperature was done and the samples were washed a last time. Coverslips were mounted with mounting medium (Dako Deutschland) on a microscope slide. 520 nm (Alexa 488), 574 nm (Alexa 546) and 460 nm (DAPI) are the corresponding emission wavelengths for the following fluorescence microscopy.

3.4 Setup

3.4.1 Amplifier System

For action potential recordings and voltage-controlled stimulation, the Bioelectronic Multifunctional Amplifier System (BioMAS) was used, a custom-made amplifier system developed and built in-house in the electronic department of ICS-8/PGI-8, Forschungszentrum Jülich. A detailed description of the system, which consists of a generalized main amplifier and specialized headstages, providing huge flexibility in carrying out bioelectronic measurements with various chip types and

3. Materials & Methods

measurement purposes, can be found in the dissertation by S. Eick [130]. Based on that, a short view over the main system components shall be given.

Main Amplifier The main amplifier (see Fig. 3.10a) contains in sum thirteen PCBs (printed circuit boards), one of which is used for the communication with a PC and controlling the measurement with a microcontroller. Further PCBs are occupied with recording and amplification circuits for the incoming cell signals. Another main part is the control and generation of the stimulation signals, localized on another PCB. The amplifier supports 64 channels for recording and on each of these channels an user-defined voltage stimulation pulse can be applied, either of sinusoidal or triangular shape (frequencies up to 200 kHz and amplitudes up to ± 5 V) or rectangular shape (same frequency range and amplitudes up to ± 10 V). In case of recording

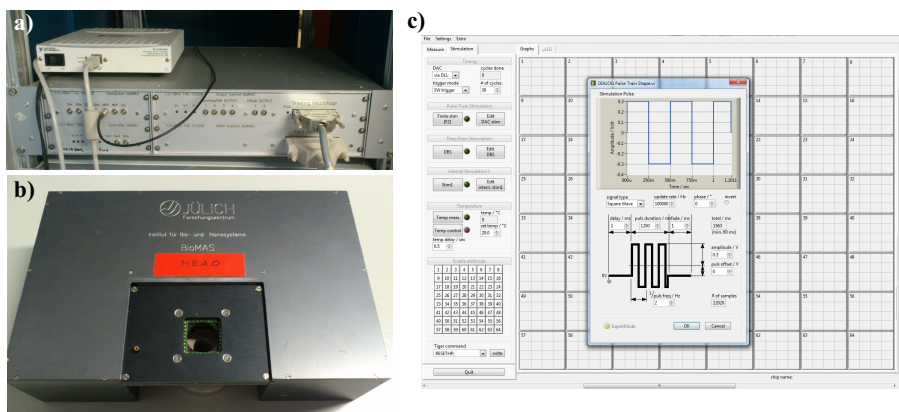


Figure 3.10: Components of the BioMAS system. a) Mainamplifier, b) pre-amplifier (headstage) and c) software interface for stimulation.

applications, the incoming signal experiences the first amplification by an inverting amplifier, with a factor of -1 or -10. After being low-pass

filtered to remove high frequency noise, the signal is passed to the second processing stage. Here, it can be chosen between a high-pass filter, realized by a RC-circuit and with an adjustable cutoff-frequency and a pass to the next processing stage without any modifications. The purpose of the first option is to suppress low-frequency drift in long-term measurements, whereas the second option is chosen if low frequency signals or DC signals are of interest.

The third processing stage is the final signal amplification. Similar to the first amplification, it is done by an inverting amplifier, providing again an amplification factor of -1 or -10. Therefore, the main amplifier enables signal amplification between factor 1 and 100. Subsequently, the signal is passed to a data acquisition (DAQ) card (National Instruments) and sampled for the transfer to a PC.

Pre-Amplifier The headstage (pre-amplifier, see Fig. 3.11b) used within this work features both recording and stimulation properties. A chip with the cell system of interest is placed directly into the headstage and contacted via 64 contact pins. The core elements for recording are two PCBs with amplifier electronics for in sum 64 channels. The amplification here is performed by a non-inverting amplifier with a high input impedance. An operational amplifier (OPA) is used, providing an amplification factor of 10. Thus, the combined amplification system offers a maximum amplification of 1000. Additionally the headstage has a slot for a reference electrode, which is connected to ground. For electrophysiological recording and stimulation, an Ag/AgCl wire was connected and immersed into the electrolyte solution of the chip.

For stimulation experiments, the voltage pulse can be generated either by the main amplifier or the DAQ card. Here, the main amplifier mode was chosen and the corresponding stimulation pulses were applied via one or several electrodes of the headstage.

Software The software for the BioMAS system was also developed in-house and programmed by D. Lomparski and W. Hürttlen. It can be divided into two parts: a graphical user interface (GUI), programmed in LabVIEW, and a dynamic link library (DLL) programmed in C++ and implemented in the LabVIEW software. The DLL executes the communication between microcontroller and main amplifier and controls the DAQ. This means, the DLL coordinates the data acquisition and storage to the PC and provides downsampled data for the instantaneous measurement visualization. The GUI is depicted in Fig. 3.11c. The 64 channels can be observed simultaneously and the stimulation pulse can be set in terms of waveform, frequency, duration and amplitude.

3.4.2 Calcium Imaging

As described in section 2.5, cells were stained with the calcium sensitive fluorescent dye Fluo-4 AM to image the intracellular calcium concentration, which is correlated to the occurrence of action potentials. In order to do that, a solution of 0.5 mM Fluo-4 AM in dimethylsulfoxide was added to the medium in a ratio of 1:2000 (v/v) and HL-1 cells were incubated 15-30 min, while differentiated ReNcells were incubated to this end for 30-45 min. After washing one time with pre-warmed medium, chips were transferred to the headstage for stimulation experiments and culture dishes were fixed on a lab boy

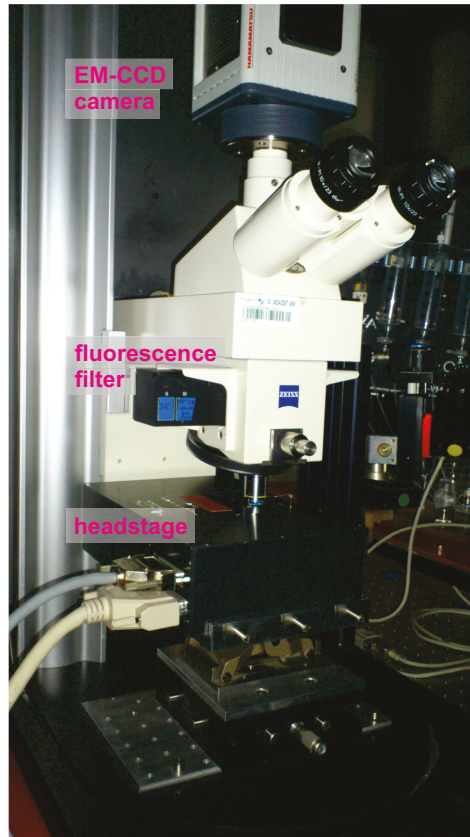


Figure 3.11: Setup for calcium imaging supported stimulation experiments. The headstage with inserted chip is visible on the bottom, followed by the fluorescence filter set for Fluo-4 AM stainings and the EM-CCD camera for video acquisition.

3. Materials & Methods

underneath the upright fluorescence microscope (Zeiss AxioTech Vario). Ca^{2+} activity was monitored in a darkfield configuration (excitation filter: BP 450-490; beam splitter: FT 510; emission filter: LP 515). To observe the cell activity, a $10\times$ (HL-1) or $63\times$ (ReNcells) immersion objective was used, for stimulation experiments inserted through the top opening of the headstage (see Fig. 3.11) and combined with a $1.6\times$ tubus lens. Calcium imaging videos with a usual length of 60 s (30 ms exposure time) have been recorded with a high sensitivity EM-CCD camera (Hamamatsu C9100-13) and the Hokawo 2.6 imaging software. Imaging was performed using a rolling average filter with a width of 4 frames and a sequential subtraction of 4 frames, referring to the Hokawo software manual calculated as following:

$$\text{AVE}_n = \text{AVE}_{n-1} + \frac{\text{IMG}_n - \text{AVE}_{n-1}}{K} \quad (3.10)$$

$$\text{SUB}_n = \text{IMG}_n - \text{AVE}_n \quad (3.11)$$

AVE_n : actual averaged image, AVE_{n-1} : previous averaged image, IMG_n : actual image frame, SUB_n : actual sequential subtraction image, K : number of the average frames, with the image variables referring to the image intensity. With $K = 4$ the rolling average causes a noise reduction with the factor 2 and therefore a better signal-to-noise ratio of the recorded fluorescence signals. The subtraction of successive image frames leads to a differentiation-like result, showing only the changes in fluorescence intensity and thus improving the signal recognition for very low signals.

Due to the live processing, equation 2.40 for a fluorescence pseudo-ratio does not apply here and the temporal averaging has to be taken into account, resulting in a simplified relation for the detected fluores-

cence intensity:

$$F' = \frac{F - F_{av}}{F_{av}} \quad (3.12)$$

With the temporal averaged intensity F_{av} and the measured fluorescence intensity of the indicator at the start of the experiment F . The complete setup for stimulation experiments with instantaneous calcium imaging is depicted in Fig. 3.11.

Propagation Analysis The propagation analysis by cross-correlation of HL-1 calcium waves was performed by a Matlab script, written by P. Rinklin [131]. The principle of operation of this script is sketched in the following.

The recorded calcium imaging videos were first transferred into the AVI format by the camera software. Next, a down-sampling to a frame size of 32×32 pixels was done and the intensity traces of each of the resulting pixels were normalized with regard to their temporal average. Subsequently, the traces were smoothed by a Gaussian filter (window width 300 ms, only for calculation of interspike intervals, not for graphical display) and active pixels were discriminated from inactive pixels by setting a certain intensity threshold. The matrix was then binary transformed into an activity mask by using its minimum value plus two times its standard deviation as a threshold and searched for connected activity regions. For cross-correlation, the average intensity trace of each active region was calculated and each pixel of the region was cross-correlated with this reference trace. In this way, each of the region's relative signal delay was detected.

In the end, the delay values were color-mapped and therefore the temporal propagation of the calcium wave could be visualized.

Chapter 4

Results & Discussion

4.1 Nanocavity Devices

4.1.1 Cavity Formation by Chrome Etching

For the fabrication of nanocavity arrays for on-chip electrophysiology, conventional MEAs were fabricated using standard cleanroom technology (see subsection 3.1.1). Gold or platinum was used as electrode material and while openings ranging between 8 and 24 μm could be chosen (smaller electrode openings aim for amperometric techniques which are not in focus here), 12 and 24 μm were expedient for voltammetric applications. After cleanroom processing of the MEAs, a simplified protocol for the fabrication of nanocavity arrays was realized. For this, the chromium adhesion layer between the electrode material and the passivation was removed along the feedlines by perchloric chromium etch solution. Fig. 4.1 shows an optical image of the back-etched nanocavity sensors. The resulting device exhibit cavities with a width of 28 μm , corresponding to the width of the feed lines. The cavity length can be controlled by optical microscopy during the etching process and ranges here around 50 μm , while the cavity height is determined by the thickness of the chromium adhesion layer (typically in the range of 100 nm). The microscopic control of the formation process revealed an etching of approx. 48 μm in 5 min to produce cavities between the metal layer and the $\text{SiO}_2/\text{Si}_3\text{N}_4$ passivation. Fig. 4.2a shows the dependency of cavity length and etching time and images showing the progression of the etching front at different time stamps are shown in the inset of the figure. The formation of nanocavities

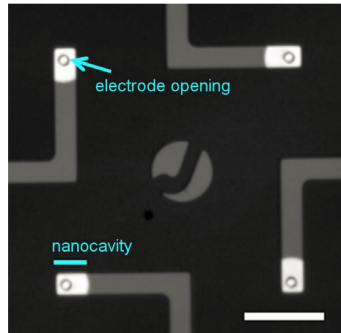


Figure 4.1: Microscopic image of 4 nanocavity sensors. The back-etched cavities are visible as rectangular bright areas at the end of the feedlines. Also the circular 12 μm electrode opening is pictured. Scale bar: 100 μm. Published in [45] and reproduced by permission of Wiley-VCH.

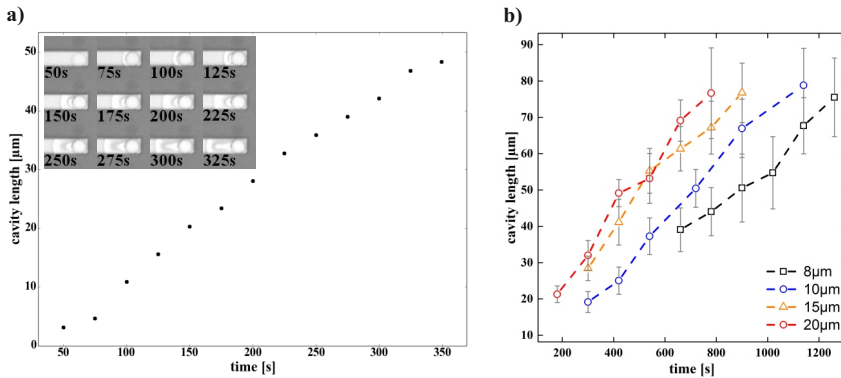


Figure 4.2: a) Nanocavity length, measured from the aperture's edge in feedline direction, over etching time. Inset: etching progress at different time stamps. The etch front, progressing from right to left along the feed line, is indicated by the sharp transition from white to grey. Published in [46] and reproduced by permission of The Royal Society of Chemistry. b) Cavity length in dependence of etching time for different electrode apertures.

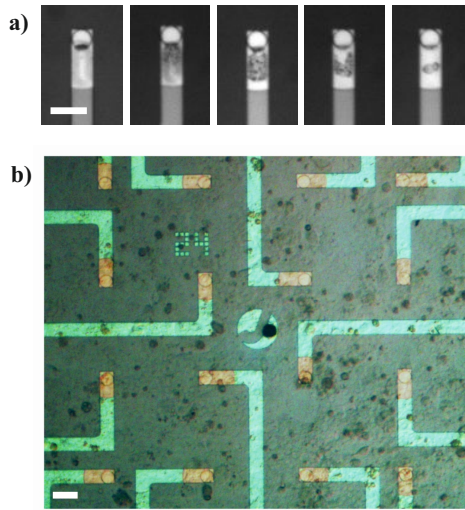


Figure 4.3: a) Filling of a cavity sensor with electrolyte. From left to right, a subsequent expulsion of air bubbles by liquid intrusion can be observed. b) HL-1 cells have been cultured on chip for several days. Back-etched cavities can be seen as rectangular structures along the feedlines. Published in [46] and reproduced by permission of The Royal Society of Chemistry. Scale bars: 50 μm .

is a well-controlled process, which can be tuned to the desired length of the nanocavity by exchanging the etching solution with water at an appropriate time. For long time-scales, the etching progress of the chromium sacrificial layer approaches a square-root dependence of time ($x \sim \sqrt{t}$) as expected for a diffusion limited process. The influence of the aperture opening on the etching time has been evaluated as well. Fig. 4.2b shows the cavity length over etching time for nanocavity arrays with sensor openings of 8, 10, 15 and 20 μm . It can be seen, that the cavity formation is fastest in case of 20 μm openings and slows down with decreasing aperture. Comparing the minimal (8 μm) and maximal (20 μm) opening for an etching time of 700 s, a doubling of cavity length can be observed. Although this is a noteworthy rate, it is also obvious that the influence of sensor opening is negligible for the difference between 20 μm and 15 μm , the relevant dimensions for voltammetric recording and stimulation experiments.

A first check of nanocavity functionality has been performed by observing the cavity filling, which is depicted in Fig. 4.3a. Here, the dark structure in the cavity channel is assumed as air bubbles, subsequently expelled by liquid intrusion. The device's stability under cell culture conditions was tested by culturing cardiomyocyte-like cells (HL-1) on chip for several days (see Fig. 4.3b).

4.2 Characterization

4.2.1 Impedance and Capacity

Impedance of Nanocavity Devices A pivot aspect for the performance of single-cell electrical recordings is the electrode impedance. This parameter is correlated to the inverse electrode area. This means that a large electrode/electrolyte interface leads to low impedance and usually a good signal-to-noise-ratio as long as the seal resistance between cell and electrode is high. In a former study it has been shown that reducing a circular aperture opening of a 30 μm electrode to 5 μm does not significantly degrade the impedance characteristics of nanocavity devices [42]. Fig. 4.4 shows the mean impedance spectra, measured from the data of 12 back-etched nanocavity sensors on the same chip. Data acquisition was performed in a frequency range between 1 Hz and 10 kHz on a nanocavity array with 12 μm electrode apertures. For the size of the total released electrode area ($\sim 1100 \mu\text{m}^2$), the readily etched sensors exhibit a rather low impedance corresponding to an unusually high specific capacitance of $\sim 160 \mu\text{F cm}^{-2}$. This could be attributed to an increased surface roughness and consequently an increased interfacial capacitance [132, 133]. More surprisingly however, only a slight influence of the nanocavity on the impedance spectra even at high frequencies can be observed. In principle, the limited conductivity in thin nanochannels should show an effect at high frequencies if the ohmic resistance starts to approach the capacitively dominated impedance of the electrode-electrolyte interface. For example, an estimation of the resistance $R = (\rho \cdot l)/A$ with the specific resistivity ρ , length l and area

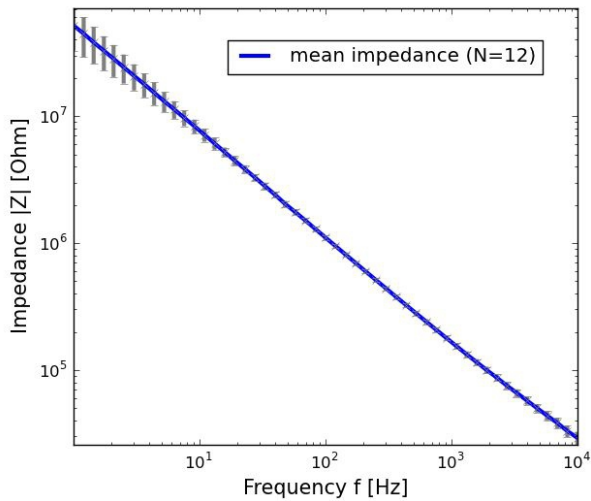


Figure 4.4: Mean impedance of 12 nanocavity sensors with an aperture of $12 \mu\text{m}$ on one chip. Published in [45] and reproduced by permission of Wiley-VCH.

4. Results & Discussion

A in a channel section of $20\ \mu\text{m} \times 20\ \mu\text{m} \times 100\ \text{nm}$ ($L \times B \times H$), filled with phosphate buffered saline (PBS, resistivity $\sim 0.6\ \Omega\text{m}$), already yields a value of $\sim 6\ \text{M}\Omega$. The full spectra of the nanocavity sensor can be approximated by solving the cable equation (2.9) with appropriate boundary conditions [43]. For the devices used in this work, a limiting influence due to the ohmic drop in the nanocavity is expected, starting already below 1 kHz, which is not evident in the data. This can be demonstrated by considering the capacitive reactance $X_C = 1/(2\pi fC)$ of the channel for the purpose of comparison. Assuming a capacitance of $\sim 10\ \text{nF}$ this leads to values of $\sim 0.9\ \text{M}\Omega$ for 100 Hz, $\sim 0.2\ \text{M}\Omega$ for 500 Hz and finally $\sim 90\ \text{k}\Omega$ for 1000 Hz, leaving the magnitude range of the ohmic resistance. Also the phase ($\sim 70^\circ$ at 1 kHz) suggests that the impedance is still dominated by the capacitance.

The described correlation between cavity dimensions and ohmic resistance as well as fabrication aspects have to be taken in account for the design of the nanocavity sensors. Sacrificial layers with a thickness in the range of 10-100 nm have been used. A significantly thicker sacrificial layer and therefore larger cavity height would decrease the ohmic drop in the nanochannel. However, the choice of cavity height is limited by device passivation at the edges of the feed lines - a significantly higher metal stack would probably result in passivation fractures. In case of large cavity heights very conformal edge-covering passivation methods would be necessary. Passivation by an atomic layer deposition (ALD) process could be a promising solution for those insulation-related issues. The length of the cavity can be tuned by the back-etching time. A further back etching of the sacrificial layer increases the exposed electrode area and thereby decreases the electrode impedance. However, depending on the cavity height and the frequency range of

interest, very long cavities will not yield an additional benefit due to the ohmic drop inside the nanochannel. Furthermore, a drawback of a longer cavity is a potential instability of the sensor.

Time-Dependent Impedance To evaluate the effect of cavity etching on the impedance of the device, impedance spectroscopy during the etching process has been performed. In Fig. 4.5, the absolute impedance values are shown in dependence of the etching time. At the end of an 800 s etching process, a decrease in impedance of about one order of magnitude can be observed. At the beginning of the etching process, when the cavity formation is initiated, the impedance is in the order of $4.3 \cdot 10^6 \Omega$ and $6 \cdot 10^5 \Omega$ for 1 kHz and 10 kHz, respectively. The specific capacitance of the just opened electrode without cavity formation lies in the range of $27 \mu\text{F cm}^{-2}$. From the microscopic time lapse images in Fig. 4.2, the progression of the cavity etching over time can be seen. During the etching process, a continuous decrease in impedance is observed until the cavity length reaches approx. $80 \mu\text{m}$ (corresponding to ~ 600 s etching time) (Fig. 4.5). At this point, effects of a larger electrode-electrolyte interface are masked by the ohmic resistance of the narrow cavity. Hence, the limiting factor for impedance improvement for long cavities is the ohmic drop inside inside the nanochannel. The back-etched electrodes show again a relatively high specific capacitance in the range of $100 \mu\text{F cm}^{-2}$. This is several times higher than the usually observed value for planar gold surfaces [134]. An increased specific electrode capacitance is generally caused by a high surface roughness of the interface. In fact, several approaches aim at increasing the capacitance of the electrodes introducing nanopatterned interface. Here, this effect is ascribed to

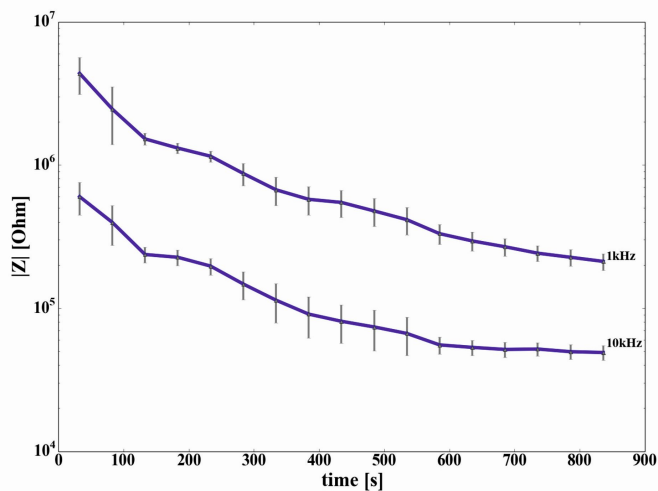


Figure 4.5: Impedance data (mean \pm standard deviation, $N=4$) as a function of etching time for probing frequencies of 1 kHz and 10 kHz at different points during the etching process. The impedance decreases with increasing etching time until at 600 s ($\sim 80 \mu\text{m}$ cavity size) the ohmic resistance of the narrow cavity starts to mask the effect of a larger electrode-electrolyte interface. Published in [46] and reproduced by permission of The Royal Society of Chemistry.

interdiffusion phenomena at the Au/Cr interface, caused by the high temperatures used in the fabrication process (300 °C).

To conclude, it is assumed that the reason for the impedance decrease of nanocavity arrays is an increased specific capacity. To specify the contribution of the surface capacity and proof the assumption of temperature control of the structuring process of gold, a silicon wafer has been metalized with a Ti/Au/Cr (10 nm/200 nm/100 nm) stack and cut into single 7 mm×7 mm samples. These samples have been heated up to a maximum temperature of 400 °C in 100 °C steps to be compared to the unheated sample state (20 °C) and an equivalently processed Ti/Pt/Cr wafer. The chromium layer was removed by a wet etch procedure. Platinum has not shown a distinct interdiffusion effect, neither in completely processed MEA devices, nor in the metalized Si samples. Therefore the interdiffusion influence of platinum is assumed to be negligible here.

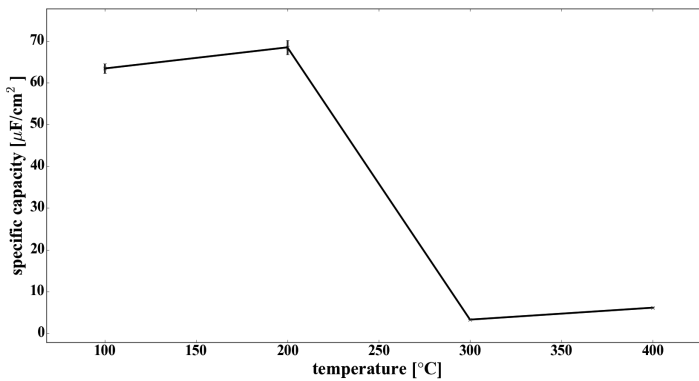


Figure 4.6: Specific surface capacitance of gold over annealing temperatures. The gold samples have been treated with KOH to remove Al residues on the surface. The values decrease with increased temperature.

To investigate the influence of the nanostructure to the increase in sensor capacity, impedance spectra have been performed on the differently annealed Au samples. Fig. 4.6 shows the capacity, calculated from these spectra. The values decrease with increased annealing temperature.

In summary, it is shown, that the here presented nanocavity sensors exhibit a low impedance. Although different strategies for decreasing the sensor impedance have been documented in literature [30, 42], the approach investigated in this thesis represents a simplified method to achieve improved electronic sensor properties. In contrast to known nanocavity fabrication protocols and electrode structuring methods, no additional lithography steps are needed and the device's cavity and structuring principle can be applied to standard MEA electrodes and hence a flexible and widely implementable technique is developed.

Although the device shows a relatively high surface capacitance, the decrease in impedance is clearly attributed to the cavity etching. This is demonstrated by impedance spectroscopy, simultaneous to the etching process. In contrast to former assumptions, the surface morphology seems to decrease the sensor capacity. Thus, these results do not match the measurements on the complete processed device. Possible influences here could be oxide formation (Au_2O_3 or Cr_2O_3) on the surface, due to chromium residues, impurities or foreign atoms. Surface strain or stress due to the temperature treatment or the quality of the gold layer could be further aspects for investigation. This motivates a detailed examination of the surface structure and composition, which has been done by AFM, SEM and EDX as presented in the following section.

On macroscopic examination of the temperature samples (see Fig. 4.7), a loss of metallic reflectivity and a change in color with increased

temperature can be observed. This can be ascribed to increased surface roughness, which will be discussed next.

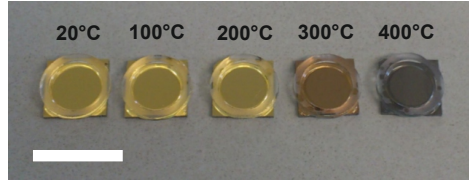


Figure 4.7: Macroscopic view on gold samples with different annealing temperature. The change in color due to different microscopic roughness is clearly visible. Scale bar: 10 mm.

4.2.2 AFM: Surface Roughness

To quantify the increase in surface roughness of interdiffusive Au nanocavity arrays, AFM investigations have been made. In Fig. 4.8 AFM images of nanocavity sensors with Au and Pt electrodes are depicted. Both metals appear very rough considering their fabrication by e-beam deposition. The Au sample shows larger and higher structures than the Pt sample (notice the different image scale here). The Au electrode shows a mean RMS roughness of 5.42 ± 1.43 nm and 5.74 ± 1.22 nm for a $25 \mu\text{m}^2$ and $4 \mu\text{m}^2$ area, respectively. The Pt electrode however, yield a mean RMS roughness of 2.47 ± 0.07 nm and 2.56 ± 0.06 nm. In principle, for a larger area of investigation, a higher RMS value should be expected. The small difference in RMS values for different areas is explained by the small magnitude of the interdiffusion structure compared to the magnitude of the considered sample section. Nonetheless, the difference in roughness and therefore the effect of surface structuring by interdiffusion is clearly evident here and confirms

4. Results & Discussion

the theory of a high surface capacity due to increased surface roughness and therefore a higher surface area for gold, whereas the interdiffusion effect of Pt is negligibly small.

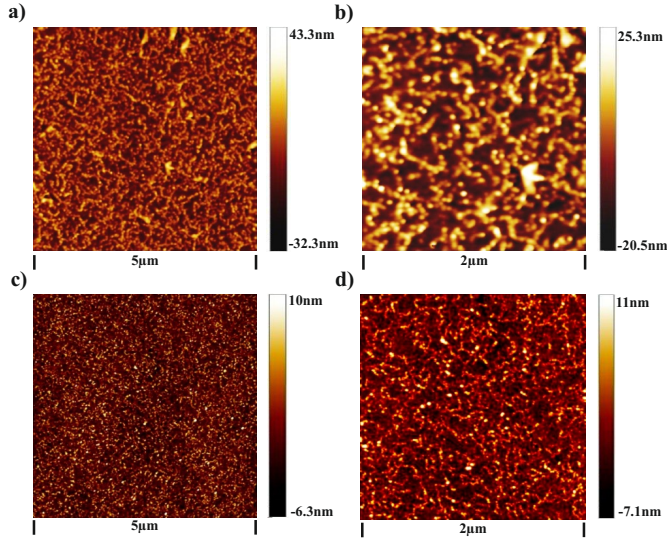


Figure 4.8: AFM images of a gold (a,b) and platinum (c,d) nanocavity array. The difference in roughness and therefore the effect of surface structuring by interdiffusion is clearly evident here (notice the different image scales).

4.2.3 SEM/EDX: Surface Structure and Composition

To characterize the readily fabricated device, SEM images were taken. In Fig. 4.9a-c SEM images of a Ti/Au/Cr nanocavity electrode with $\text{SiO}_2/\text{Si}_3\text{N}_4$ passivation can be seen. It shows a rough electrode surface with the expected structuring by interdiffusion. The chip was processed at a higher temperature (maximum temperature of approx.

300 °C) compared to devices which does not show a structuring effect by interdiffusion. Hence and on basis of the described characteristics of

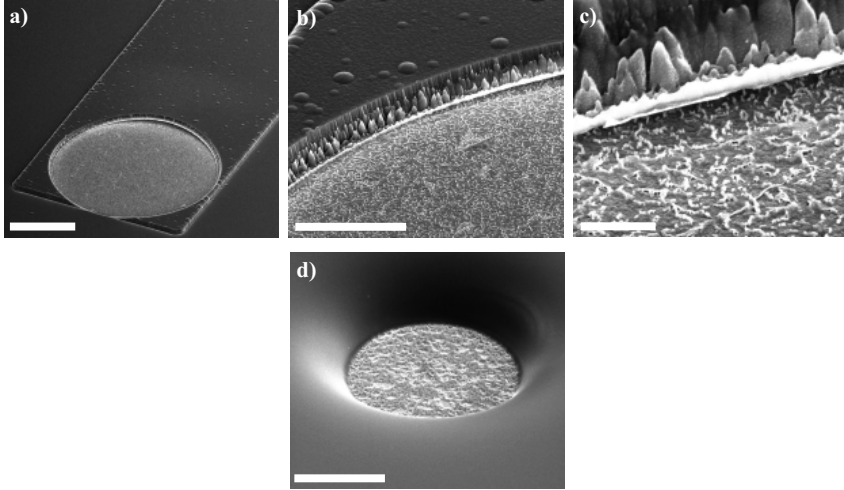


Figure 4.9: SEM images of a nanostructured cavity device with gold electrode and $\text{SiO}_2/\text{Si}_3\text{N}_4$ passivation (a-c) and platinum electrode and PI passivation (d). The effect of gold interdiffusion on the electrode surface can be seen (c) as well as the bending of the brittle passivation due to intrinsic stress (a). The latter does not occur in case of PI (d). Scale bars: 5 μm .

the interdiffusion phenomena, it can be assumed that the structuring effect could be controlled by annealing temperature. This represents a first guiding finding towards the characterization of the structuring process.

An additional effect which can be observed in Fig. 4.9, is the bending of the $\text{SiO}_2/\text{Si}_3\text{N}_4$ passivation layer at the edge of the electrode opening in feedline direction. This is caused by the rather brittle material characteristics of the passivation stack. Besides the discussed advantageous properties in cell culture of PI for chip passivation (see subsection 3.3.2), PI also does not show this kind of cavity deformation,

as demonstrated with the equivalent SEM image of a PI passivated cavity sensor in Fig. 4.9d.

The structure of thin evaporated metal films is decisive for their electrical resistivity and depends on substrate material and temperature during evaporation, evaporation rate, vacuum quality and film thickness [135, 136]. The substrate temperature plays a particularly important role. For a first microscopic characterization of the differently annealed samples, SEM images have been taken (see Fig. 4.10). Besides the described interdiffusion effect for annealing temperatures of 200 °C and higher, the entropically favorable polycrystalline character of gold, manifesting in morphological grains at the layer surface, can be seen in the 20 °C and 100 °C samples and to a lesser extent at 200 °C and 300 °C. It has been reported, that these grains are comparable in dimensions with the film thickness [137]. Here, the gold film thickness has been 200 nm, while the observed grains for the 20 °C sample appear in a range of around 100 nm. Further, it is known that the crystallographic grain size (imbedded in the bulk) saturates with increasing film thickness (for gold at a thickness of 140 nm and a grain size of 48 nm [136]), while the morphological grain size (at the film surface) keeps increasing with film thickness. This can be explained by interpreting the saturation as high density crystallographic defects and considering the morphological grains as agglomerates of crystallographic grains. As expected and described in literature [135, 138], the grain structure gets flattened with increasing temperature. This especially becomes clear by comparison of the 200 °C and 300 °C samples. Van Attekum et al. investigated in their work [137] the resistivity for gold films at room temperature in dependence of the film thickness. It is revealed, that possible structural defects by grain formation have a major influence on the resistivity

only for film dimensions smaller than 50 nm. The resistivity for gold films of 200 nm is reported with $2.5 \mu\Omega\text{cm}$, therefore the influence of grain formation on film resistivity can be neglected within the scope of this thesis.

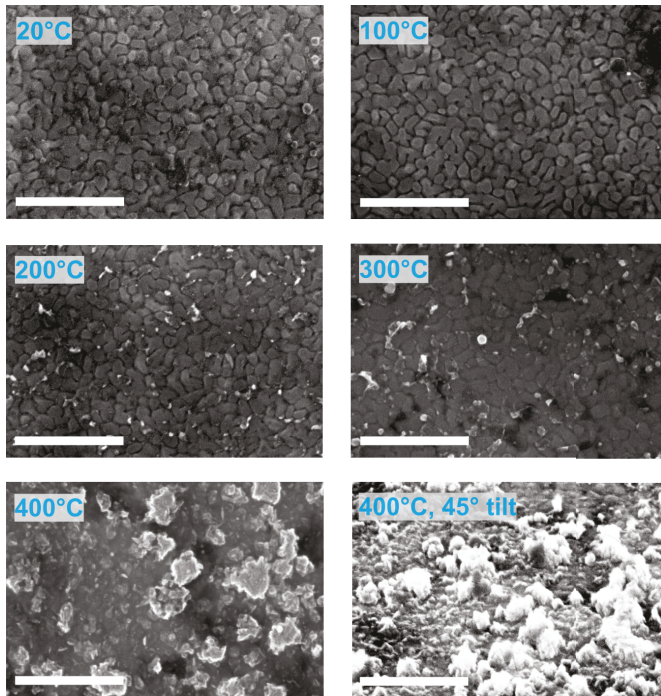


Figure 4.10: SEM images of gold samples annealed at different temperatures. A Ti/Au/Cr metal stack was deposited on a silicon wafer, after heating and cutting in square samples, the chromium layer was removed by wet-etching. At 20 °C, 100 °C and 200 °C the grain boundaries of gold are clearly visible, while first interdiffusion structures form at 200 °C. The effect increases at 300 °C and ends in formation of an eutectic alloy at 400 °C. Scale bars: 500 nm.

Although grain formation is not a pivot aspect for resistivity considerations, it has to be preconceived for evaluation of grain boundary

interdiffusion effect. Atomic diffusion in solid metals and alloys is mediated by defects like point defects (vacancies, interstitials), dislocations, grain boundaries, phase boundaries or free surfaces, since the mobility of atoms is usually higher around those discontinuities [108]. The two main mechanisms which have to be taken into account here are bulk diffusion through the gold and grain boundary diffusion. In Fig. 4.10 the appearance of first diffusive structures between single grains can be seen for an annealing temperature of 200 °C, which is consistent with the observations of Hirvonen et al. [100], who reported no migration of chromium for a 150 °C annealing, but for 250 °C and 450 °C. After annealing with 300 °C a diffusion increase can be observed as well as a spreading of the metal grains, before leading to the nodal and undulating structure seen in the 400 °C image. Similar structures have been shown in [107]. The tilted perspective furthermore depicts a structural change on a smaller scale in-between the bigger nodes. Because the activation energy for grain boundary diffusion is lower than for bulk diffusion [108], first the grain boundaries are decorated with diffusion structures.

Two rather macroscopic side effects of the 400 °C annealing are shown in 4.11. Here, surface defects have formed, which interestingly reflect the sample geometry (Fig. 4.11a and b). The orientation of the defect square is parallel to the orientation of the sample square. This is probably a matter of structure transfer due to the different lattice constants of gold and chrome. Additionally the thermal strain seems to cause fissures in the gold layer (Fig. 4.11c and d), leaving the layer in single isolated patches which might not be in contact with the remaining metal film anymore.

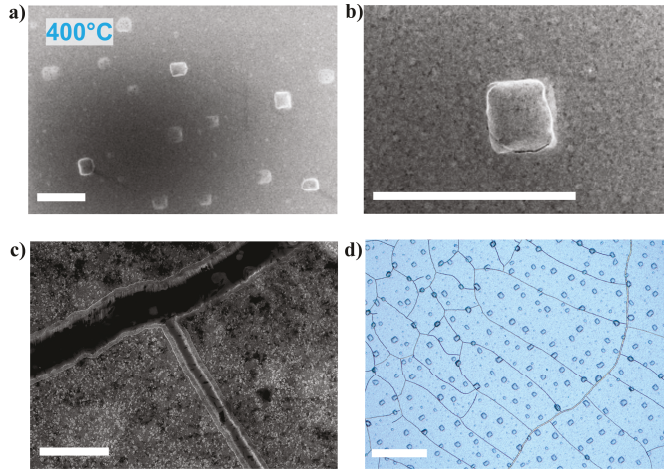


Figure 4.11: SEM images (a-c) of a 400 °C annealed gold sample and an optical micrograph (d), depicting structural defects ascribed to the high temperature treatment. Scale bars: 50 μm (a,b,d) and 5 μm (c).

A potential drawback of the process which has to be considered is on the one hand the possible formation of chromium oxide on the surface structure. This has been reported in particular for a 11 h anneal at 250 °C and generally for 450 °C [100]. On the other hand, the relation between diffusion process and change in resistivity, as reported by Rairden [103] as well as Thomas and Haas [139], can alter the potential functionality for electronic devices. This means that the Au layer's resistivity increases with proceeding diffusion, i.e. increasing chromium content. Slusark et al. [102] report a change in resistivity of approx. 2.1 $\mu\Omega\text{cm}$ per Cr percentage. For 300 °C and higher annealing they found a maximum gold resistivity of 23 $\mu\Omega\text{cm}$. Many studies focus on the influence of a chromium adhesion layer on the properties of gold conducting paths, thus investigate the chromium diffusion into the gold layer. Since the self-diffusion coefficient of gold

4. Results & Discussion

is higher than that of chromium ($1.6 \cdot 10^{-36}$ vs. $4.7 \cdot 10^{-59} \text{ m}^2 \text{ s}^{-1}$ at 300 K [104]), it can be assumed here, that gold is rather migrating into the chromium layer than the other way around. This is confirmed by the work of Majni et al. [140] about the interdiffusion of chromium and gold films on silicon. By backscattering spectra and an Arrhenius fit they determine the interdiffusion coefficient of Au in Cr for a temperature of 425 °C to be $D = 2.2 \cdot 10^{-16} \text{ cm}^2 \text{ s}^{-1}$, the pre-exponential factor to be $D_0 = 2 \cdot 10^{-11} \text{ cm}^2 \text{ s}^{-1}$ and the Au activation energy of a grain boundary controlled diffusion process to be $E_T = 0.68 \text{ eV}$. Combining these parameters with the annealing temperatures used for the samples in Fig. 4.10 leads to the dependence of diffusion coefficient and temperature depicted in Fig. 4.12a. For temperatures above 200 °C the coefficient starts to rise and reaches $0.21 \cdot 10^{-16} \text{ cm}^2 \text{ s}^{-1}$ for 300 °C and $1.62 \cdot 10^{-16} \text{ cm}^2 \text{ s}^{-1}$ for 400 °C. This is consistent with the interdiffusion investigations by SEM, showing a distinct structure at these temperatures. The effect at 200 °C might be ascribed to a comparable small coefficient of $0.01 \cdot 10^{-16} \text{ cm}^2 \text{ s}^{-1}$ and a deviance in temperature setting during the annealing process.

In [140] an activation energy for Cr of 2.35 eV is given. The equivalent plot of the diffusion coefficient can be seen in in Fig. 4.12. It is obvious, that the time scale is several magnitudes smaller and the starting temperature is higher for Cr than for Au diffusion.

This leads to the question of the surface composition and how much Cr the structured Au electrode includes. For that, the phase diagram of the Cr-Au bulk has to be examined (see [139, 141]), leading to the estimation of the maximum chromium solubility in Au to be about 25% and 15% at 150 °C [102]. To evaluate these values, EDX spectra of

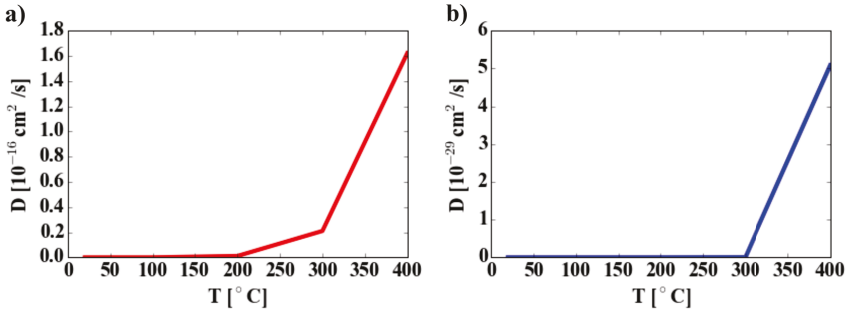


Figure 4.12: Visualization of the interdiffusion coefficient D for Au (left) and Cr (right) in dependence of annealing temperature, based on findings in [140].

a structured and readily processed nanocavity sensor have been taken first.

The EDX image of the sensor (see Fig. 4.13) as well as the correspondent spectra (Fig. 4.14) validates the characterization of the interdiffusion process. Si and Au have been detected here, as well as O and N. The latter originates from the oxide and nitride content of the passivation. Cr was not detected, as expected for an approx. 300 °C annealed metal layer. The weak signal depicted in the EDX micrograph for Cr is an artefact caused by similarities in emission of O and Cr: The $K\alpha$ emission line energy of oxygen (524.9 eV) and the $L\alpha$ emission line energy of chromium (582.8 eV) are close. Thus, the low “chromium content” identified in this image actually belongs to the oxygen emission of the sample. To go further into the question of surface composition of the chrome etched gold layer, EDX spectroscopy has been performed on the 200 °C, 300 °C and 400 °C annealed gold samples. Representative spectra are shown in Fig. 4.15. In all spectra Au and Si have been found, corresponding to the silicon substrate

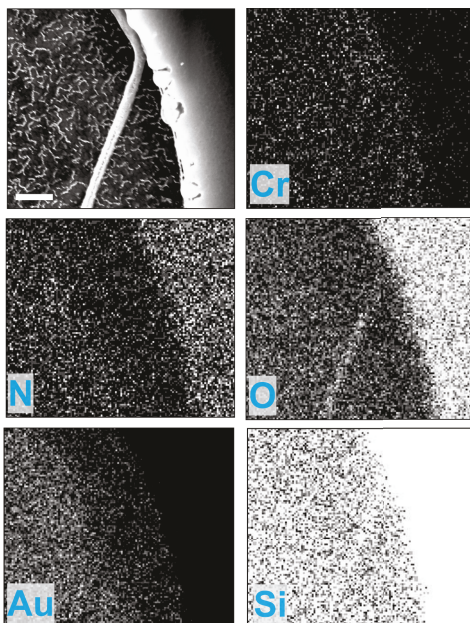


Figure 4.13: SEM image and EDX micrographs of an Au nanocavity sensor, processed at a temperature of approx. 300 °C. Depicted is the transition from electrode area to passivation. Scale bar: 500 nm.

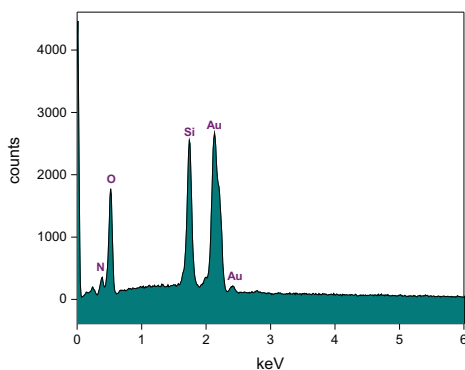


Figure 4.14: EDX spectra of a complete processed Au nanocavity sensor, process temperature approx. 300 °C.

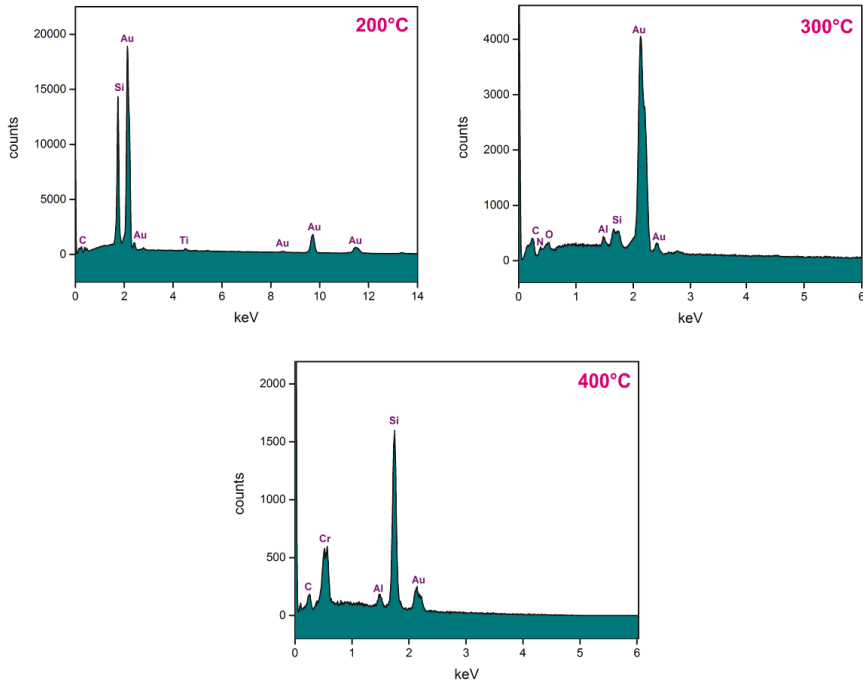


Figure 4.15: Exemplary EDX spectra of differently annealed Au layers. Besides the elements of electrode, substrate and sacrificial layer material, a contamination with Al has been detected.

and the Au layer, whereas a very small amount of Cr (2.46% in one of three spectra, see table 4.2) on the 300 °C and no chromium on the 200 °C sample has been detected. Additionally a contamination with Al was found in the 300 °C and 400 °C spectra, caused by the evaporation chamber in which Al has been processed before. It is assumed, that Al residues on the chamber wall disengaged at some point of the fabrication process, therefore a rather statistical appearance in terms of location on the sample and temperature dependence is not surprising. The material diffusion at 300 °C and 400 °C is higher than at 200 °C, another aspect which could explain the Al absence in the 200 °C spectra. The temperature dependent capacity data shown in Fig. 4.6 has been measured on KOH treated samples (0.1M solution, 20 h). KOH has been used to remove any Al on the surface, but considering the material mixing by interdiffusion and alloy forming, it is still uncertain how much Al remained in the Au layer. The low nitrogen and oxygen content found in the 300 °C sample could be identified as a contamination, maybe caused by chrome etch residues (NO_3 group in the etch solution). Interestingly, also a small carbon peak appears in the spectra of all samples, which can be ascribed to a possible organic contamination (see Fig. 4.10). This assumption is supported by dark (less conductive) areas in the SEM pictures, interpreted as organic material. To follow the question of layer composition and remaining Cr in the case of 400 °C annealing, the EDX spectra have been quantified (see tables 4.1,4.2 and 4.3).

As shown in the corresponding spectra, no Al was found in the 200 °C sample, while a small amount of $0.51 \pm 0.21\%$ was detected in the 300 °C sample. Si and Ti was found in both samples. This can be explained by the penetration depth of the EDX, which has

Spectrum	C	N	Si	Ti	Au
1	1.72	1.78			96.50
2	3.39	1.37			95.24
3	2.59	4.88	12.47	0.46	79.61
4	3.56	4.42	12.43	0.52	79.07
5	3.94	4.53	12.32	0.51	78.71
Mean	3.04	3.40	12.41	0.50	85.83
Std.	0.79	1.50	0.06	0.03	8.22

Table 4.1: Quantification of elements found by EDX in the 200 °C sample. All values in weight%.

the magnitude of ~ 500 nm. Since the penetration depth is energy-dependent, it can be differ for the presented spectra, depending on what energy range was applied for investigation.

The points on the 400 °C sample which has been investigated can be exemplary seen in Fig. 4.16. Spectrum 1 and 4 were taken on points of elevated material, while spectrum 2 and 3 were taken on the lower areas of the topography. As expected, all spectra give peaks identified with the materials of substrate, electrode and sacrificial layer: Si, Au and Cr.

Table 4.3 shows the amount of Al, Si, Cr and Au in weight percent. In the elevated sample points (spectrum point 1 and 4) the Cr amount is slightly lower than in the lower points (41.10% and 44.05% vs. 53.70% and 47.48%). This could confirm the diffusional behavior of Au und Cr depicted in the diffusion coefficient plots in Fig. 4.12. The diffusion of Au starts at a lower temperature (due to a lower activation energy) and is faster. Additionally, the Au diffusion is more distinct at the grain boundaries. Thus, the elevated structures contains more Au, while the result of the later Cr diffusion inset can

4. Results & Discussion

Spectrum	N	O	Al	Si	Au
1	1.75	1.16	0.71	1.10	93.16
2	2.15		0.46	1.54	93.39
3	1.74	1.29	0.40	1.25	95.32
4	2.29		0.45	2.26	93.73
Mean	1.98	1.23	0.51	1.54	93.90
Std.	0.24	0.07	0.12	0.45	0.85

Table 4.2: Quantification of elements found by EDX in the 300 °C sample. Due to reasons of arrangement, the values for C, Ti and Cr (2.14%, 2.46%, 1.28%) are not depicted. They were measured only in one spectrum each (1, 2, 4). All values in weight%.

be observed in the lower topography. It is interesting to see that the mean sample percentage of Cr is higher than the amount of Au. This can be explained on the one hand by the eutectic point of the Cr/Au composite, which influences the resulting Au structure. On the other hand, a possible diffusion of Au into the underlying Si/Ti layer has to be considered, whereas the only 10 nm thick Ti layer represents only a small contribution. At an annealing temperature of 370 °C all three phases are in equilibrium. The Gibbs free energy equals zero and a complete mixing of Au, Si, Ti and Cr takes place [140, 142]. Thus, the high amount of Cr in the whole sample and especially in the lower areas of the surface structure represent the formation of an eutectic alloy at the interface of Au and Cr. Further it can be assumed that for temperatures above 350 °C the alloy formation dominates the above discussed grain boundary diffusion. This is supported by the spectra of samples with an annealing temperature below the eutectic point (200 °C and 300 °C), in which no Cr was found. The structure of the 200 °C and 300 °C samples can hence be completely ascribed to the

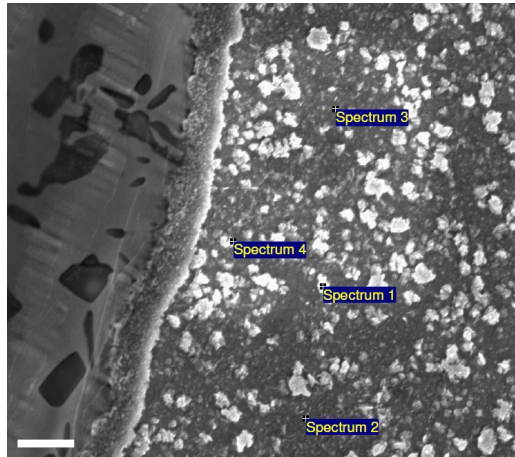


Figure 4.16: Several locations on a 400 °C annealed gold sample were investigated by EDX spectroscopy. The points of interest are marked in this SEM image. Scale bar: 500 nm.

diffusion process. Despite that, a very small amount of Ti was found in all three quantified EDX investigations (data not shown): $\sim 0.49\%$ (200 °C), $\sim 1.28\%$ (300 °C) and $\sim 2.42\%$ (400 °C). The increasing trend indicates an increasing diffusion of the Ti adhesion layer underneath the Au layer.

It can be concluded, that for the utilization of interdiffusive gold electrodes, a starting temperature of the effect around 200 °C was found. While the grain structure of gold (distinctive at lower temperatures) is assumed to be negligible, surface defects at higher temperatures (400 °C) have to be considered in terms of reduced conductivity. A very distinct structural effect could be demonstrated for annealing at 400 °C, caused by alloy building of the involved materials. Further, the EDX evaluation of readily processed nanocavity devices shows a rather unremarkable spectrum, exhibiting Au (electrode material)

4. Results & Discussion

Spectrum	Al	Si	Cr	Au
1	1.45	31.35	41.10	26.11
2	0.40	35.74	53.70	10.15
3	0.58	29.61	47.48	22.32
4	1.27	29.63	44.05	25.04
Mean	0.93	31.58	46.58	20.91
Std.	0.51	2.89	5.42	7.35

Table 4.3: Quantification of elements found by EDX in the 400 °C sample. All values in weight%. The corresponding points of investigation are depicted in Fig. 4.16.

as well as Si, O and N (substrate and passivation). The differently annealed planar gold samples contain Au (200 °C and 300 °C) and a contamination by Al (300 °C). The most exceptional spectrum is attributed to the 400 °C sample, showing a high amount of Cr ($\sim 47\%$) compared to a lower amount of Au ($\sim 21\%$) and also an Al contamination. While many investigations of metal diffusion focus on the diffusion of the adhesion layer material into the conduction path on top, initial investigations on the diffusion of the electrode material have been achieved here. This lays the foundation for utilizing the electrode material of conventional devices for a further functionalization towards a improved electrochemical or electrophysiological interface.

So far it has been shown, that there are several possible influences of the surface structure and composition like Au grains, Al contamination, thermal fissures and Cr residues, while the structure and composition of 400 °C annealed Au/Cr samples is dominated by alloy formation. Another aspect which should be investigated for evaluating the electrochemical behavior of interdiffusive structured devices is the

surface energy, i.e. hydrophobicity. To follow this, contact angles were measured in dependence of the annealing temperature.

4.2.4 Contact Angle: Surface Energy

Fig. 4.17 shows the contact angle in dependence of the annealing temperature. For that, a 5 μL drop has been deposited and after 10-20 s the contact angles have been determined by the Laplace-Young fit. After the angle rises until 100 $^{\circ}\text{C}$, between 200 $^{\circ}\text{C}$ and 300 $^{\circ}\text{C}$ a drop sets

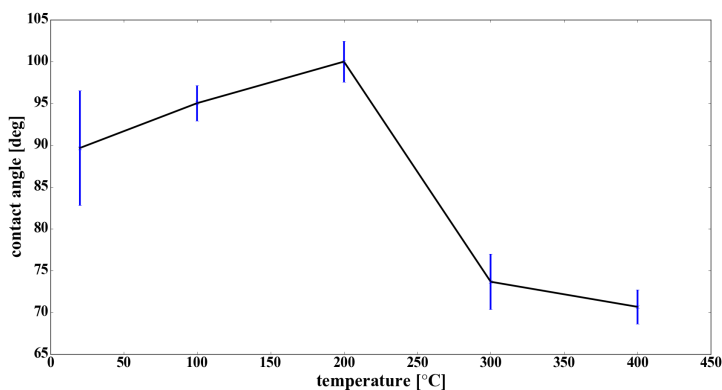


Figure 4.17: Contact angle of gold in dependence of annealing temperature.

in. This indicates a correlation with the interdiffusion of gold, which starts above 200 $^{\circ}\text{C}$. Although the Au samples have been treated with a plasma activation before the capacity was determined, it becomes clear, that the contact angle and temperature dependent surface capacity are correlated. Thus, the hydrophobicity first increases, which could be interpreted as an increase in surface roughness from 20 $^{\circ}\text{C}$ to 200 $^{\circ}\text{C}$. Also, the increasing contact angle could be an indication for a surface

contamination by foreign metal atoms, water or organic material. All of this could alter the surface behaviour. Then, the angle drops and the hydrophobicity decreases marking an activation point for a surface effect between 200 °C and 300 °C. Considering the SEM images of the 300 °C and 400 °C sample, attention has to be drawn to the relative small contact angle difference between those two points. Here, a significant topographical change leads only to a small change in contact angles. After all, also a counteracting effect of annealed and therefore merging grain boundaries and the interdiffusion effect has to be taken into account. While the gold interdiffusion causes a higher surface roughness, the annealing of gold grains represent a smoothing effect.

Aiming to establish a consistency between the advantageous electrical properties of nanocavity arrays in terms of low impedance and high surface area and the opposing results of investigations on large scaled Au layers, several factors have been revealed which could distort a detailed surface capacity estimation: metallic or organic impurities and contaminations, thermal stress as well as material mixing due to alloy formation. A main point yielded by the contact angle measurements is the similar behavior of the 300 °C and 400 °C samples. The drop in the contact angle indicates a common effect on surface energy for these samples. It is further remarkable, that there is only a small contact angle difference between 300 °C and 400 °C, although a distinct structural change is documented here.

Nonetheless one of the core issues in introduction of a new fabrication method of a modified device is the question about functionality. As a first experiment to proof this, FIB sectioning on cell-covered nanocavity sensors were done and will be presented and discussed in the following.

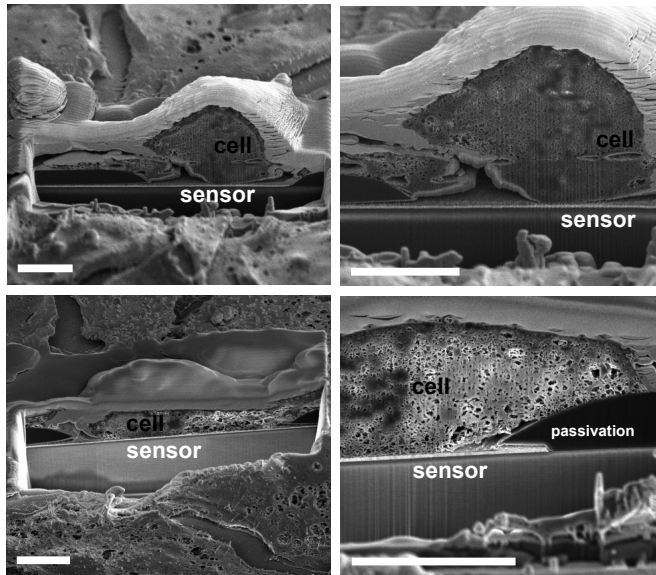


Figure 4.18: FIB cross-section of HL-1 cells on a nanocavity sensor. A tight contact between cell and gold (top) and platinum (bottom) sensor can be seen. Scale bar: 5 μm .

4.2.5 FIB: Cell-Chip Coupling

A crucial factor, which influences the sensing and stimulation performance of a functional device, is the cell-substrate interface. A low seal resistance of this junction alters signal transmission between the cell membrane and sensor and reduces the signal transfer significantly. It has been shown that the seal resistance for nanocavity devices can lie in the range of several tens of $M\Omega$, an order of magnitude higher than standard planar MEAs [43]. Here, the cell-sensor interface has been evaluated by SEM in combination with focused ion beam (FIB) sectioning, as shown in Fig. 4.18. The cell covered sensor displays only a small cleft between cell and electrode. Further it can be clearly seen, that the cell adheres tightly and directly to the electrode surface, even for a nanocavity sensor with Pt electrode (Fig. 4.18 bottom), showing only a small roughening effect.

This behavior might be promoted by the rough surface morphology, which is associated with an increased surface energy. Several studies have shown, that micro- and nanostructured surface modifications of metallic and non-metallic surfaces influence cell adherence and growth [143–147]. Hallab et al. [148] evaluated metallic biomaterials and found that surface energy and roughness are correlated with cell adhesion strength. Although they stated that there is no clear effect of surface roughness on adhesion strength on metallic surfaces, they showed a linear relationship between surface energy (measured in PBS and DMEM medium among other liquids) and cell adhesion strength of fibroblasts. It can be assumed, that influencing surface energy by increasing the surface roughness can lead to an improved cell adhesion on metallic biomaterials. Brüggemann et al. [44] showed in their study

about the adhesion of electrogenic cells on gold nanopillar electrodes, that a surface structuring on a nanoscale promotes the adhesion of HL-1 and HEK cells, but is not advantageous for neuronal cells.

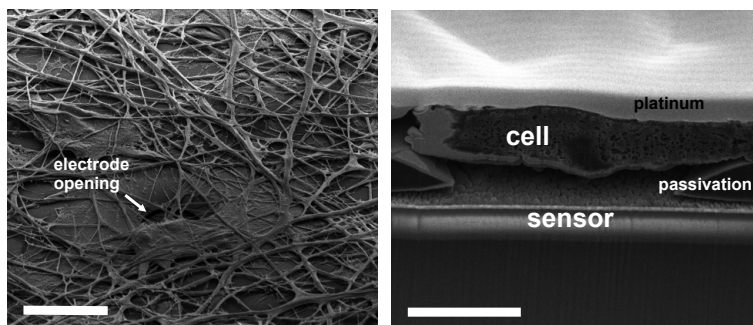


Figure 4.19: FIB cross-section of ReNcell VM on a gold nanocavity sensor. The cells show good adhesion on the PI passivation, but does not extend into the electrode opening. Scale bars: 10 μm (left) and 3 μm (right).

Here, this finding can be confirmed for the adhesion on nanostructured cavity electrodes. Even though it is not clear, whether an improved adhesion strength is related to the cell-chip interaction or the interaction between adhesion proteins and the surface, it has been shown that the nanostructuring of nanocavity sensors leads to a higher surface energy, promoting a better cell adhesion for HL-1 cells. Furthermore, SEM investigations on differentiated ReNcell VM (Fig. 4.19) show a weaker cell adhesion of neuronal cell bodies to the nanostructured electrode. Thus the findings regarding neuron adhesion on nanopillar gold electrodes in literature [44] can be confirmed for the neuronal progenitor cell line ReNcell VM.

In further FIB investigations, another highly functionalizable feature of nanocavity devices could be demonstrated. Remarkably, parts of the HL-1 cell seem to grow inside the channel covering the nanostructured

4. Results & Discussion

electrode. The ability of the HL-1 cell to penetrate into microstructures [149] is well known and utilized in applications like spatial separation [150], cell tapping [35] and guided growth [151]. Here, it is demonstrated that HL-1 cells are also capable of penetrating much smaller channel-like structures, which exhibit a height of only around 180 nm, providing a tight cell-device sealing.

In summary, a good cell-chip coupling and even the tight sealing by HL-1 cell growth into the cavity have been demonstrated. To further verify the functionality, extracellular AP recordings and stimulation were performed with nanocavity arrays, accomplishing two important applications for micro-electrode arrays in electrophysiological cell investigations.

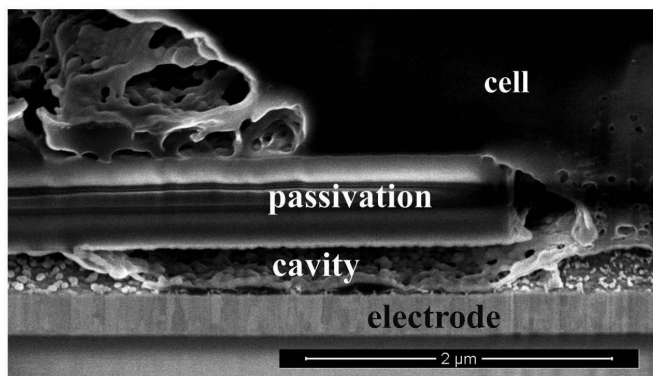


Figure 4.20: FIB cross-section of an HL-1 cell on a gold nanocavity sensor. In-between passivation and electrode, cellular protrusion into the cavity is observed. The cleft between cell and electrode is small, allowing for a tight sensor sealing and therefore a good signal transduction. Published in [46] and reproduced by permission of The Royal Society of Chemistry.

4.3 Application

4.3.1 Action Potential Recordings

The evaluation of the nanocavity device for cell culture applications was performed by extracellular action potential recordings. As model for an electrophysiologically active cell system, the cardiomyocyte-like cell line HL-1 was used [58]. A confluent cell layer is loaded with the calcium sensitive fluorescent dye Fluo-4 AM for a simultaneous optical monitoring of electrical activity. By using a calcium-sensitive fluorescent dye it is possible to visualize intracellular calcium concentrations correlated with the occurrence of action potentials [152]. The graph in Fig. 4.21 shows electrical signals captured from five channels (blue) and the correlated optical fluorescence signal, extracted from areas of interest above the corresponding electrodes (red overlay). Although the calcium signal is significantly slower than the electrical action potentials, the correlation is clearly visible. The staining of the confluent cell layer on the chip leads to the observation of a propagating calcium wave through the confluent cell layer. This can be utilized for the optical evaluation of stimulation experiments [152] without electrical recordings, which are often distorted during the chip-based stimulation process via crosstalk [153].

Recorded electrical signals from a back-etched nanocavity are displayed in Fig. 4.22. They show peak-to-peak amplitudes of up to approx. 3 mV, which suggests good sealing properties at the cell-sensor interface. The large signals avoid any necessity to reduce the bandwidth by filtering the data. Nevertheless, the unfiltered noise during record-

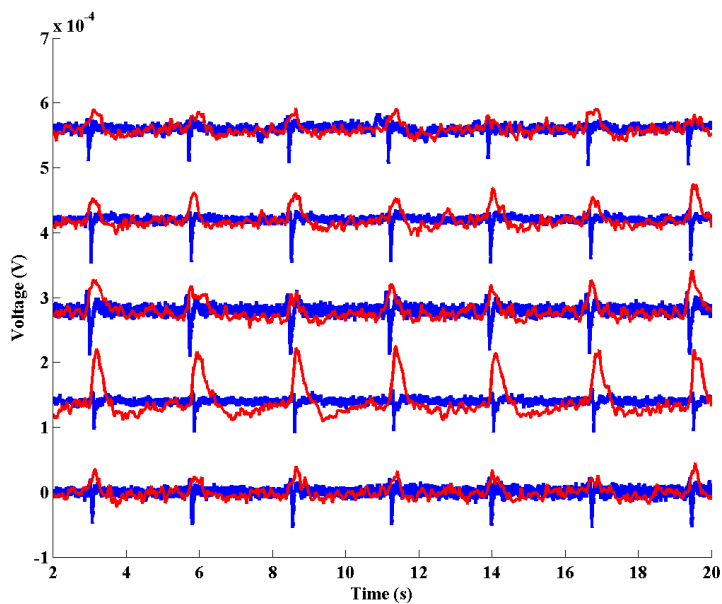


Figure 4.21: Electrical signals recorded on five electrodes (blue) and corresponding optical traces, captured directly above the electrodes (red, a.u.). Although the calcium signal is significantly slower than the electrical action potential, the correlation is clearly observed. Published in the Electronic Supplementary Information of [46] and reproduced by permission of The Royal Society of Chemistry.

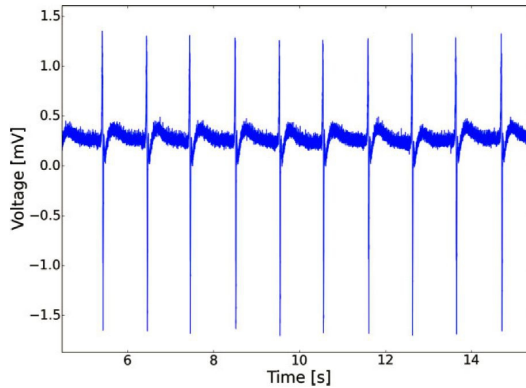


Figure 4.22: Action potential recordings from HL-1 cells performed with nanocavity arrays. Published in [45] and reproduced with permission of Wiley-VCH.

ing was relatively high ($\sim 27 \mu\text{V}$ RMS) and can be attributed to the home-built headstage. Since it features both, stimulation and recording properties, the signal path has to be separated and is equipped with additional electronic elements contributing to the overall noise level. However, the results demonstrate the promising capabilities of the back-etched nanocavity devices.

The functionality of surface structured nanocavity arrays has been demonstrated as well (see Fig. 4.23a and b). Additionally, the propagation of the electrical signal through the cell layer and the spatial resolution of the device are illustrated. Exemplary traces of three channels are displayed, showing action potential recordings of HL-1 cells recorded with surface structured nanocavity sensors. To remove artifacts, that originate from the camera trigger during simultaneous optical recording, electrical AP recordings have been smoothed by a Savitzky-Golay filter [154] (window size of 51, 3rd order polynomial,

unfiltered data shown in Fig. 4.23c). The action potentials have a peak-to-peak amplitude in the range of 1 mV and a signal-to-noise ratio of about 50 (peak-to-peak signal vs. peak-to-peak noise). The propagation of the electrical signals through the cell layer and the spatial resolution of the device are illustrated by the temporal difference of signals recorded with channels, located at different positions on the chip. Calculated from three exemplary traces, the propagation velocity of the action potential wave is approx. 11 mm s^{-1} .

The here discussed evaluation of the nanocavity sensor applicability for action potential recordings has further confirmed the concept of a simplified modification method towards low impedance electrodes with a good cell-sensor sealing, enabling high SNR voltammetric recordings. Besides a high SNR, the measured signals show comparable or even higher amplitudes as measured with devices fabricated with a more complex approach [29, 30, 32].

4.3.2 Voltage-Controlled Stimulation

This paragraph focuses on the evaluation of localized voltage-controlled stimulation using nanocavity arrays. To evaluate the cell activity independent of electrical measurements, simultaneous optical recordings were performed. For the stimulation experiments, biphasic square wave pulses with a duty cycle of 30, a frequency of 250 Hz and amplitudes between 600 mV and 900 mV were applied. 30 cycles were repeated within a 60 s time frame generating a stimulation pattern of approximately 0.5 Hz. The calcium fluorescence intensities at the 16 electrodes within the sample image were extracted and plotted over time (see Fig. 4.24). The left graph shows a rather irregular

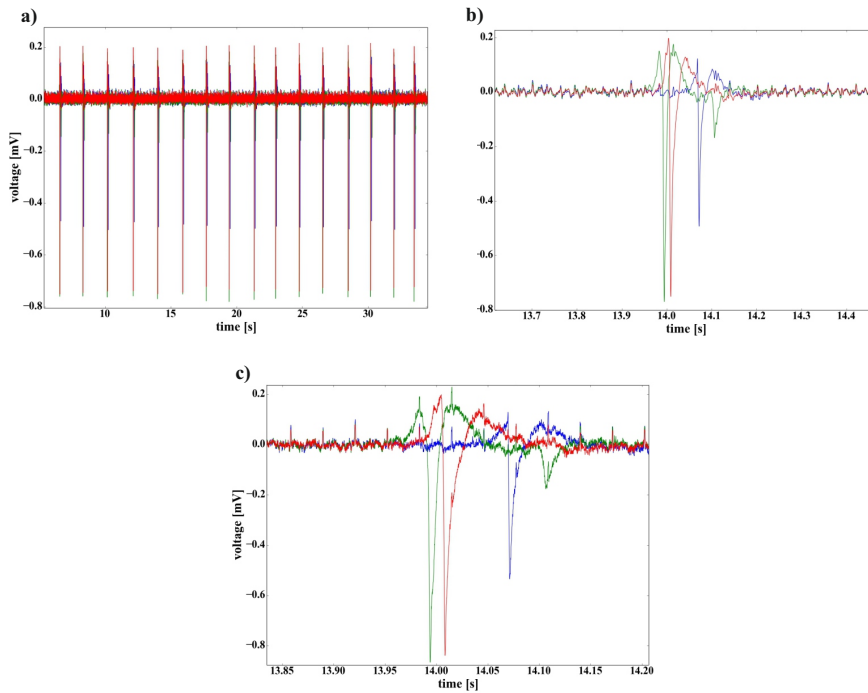


Figure 4.23: Action potential recordings performed with surface structured nanocavity arrays. Shown are three channels, the traces are smoothed by a Savitzky-Golay-filter. The beating behavior over a time span of 30 s is shown in (a). (b) Shows single beating events of the same traces at a higher time resolution. The temporal shift of the three spikes becomes evident indicating the propagation of the action potential across the cell layer. The unfiltered signal is depicted in (c). Published in [46] and reproduced by permission of The Royal Society of Chemistry.

4. Results & Discussion

behavior of the unstimulated HL-1 layer (Fig. 4.24a). The right graph displays the cell network's response to the stimulation in terms of a higher beating frequency and an increased regularity (Fig. 4.24b). The data unequivocally shows that the signal, which is applied via the nanocavities, forces the beating pattern of the HL-1 network to fall in line with the stimulation frequency. This circumstance gets even more explicit by calculating the mean spike frequencies for the stimulated and unstimulated network as shown in Fig. 4.25. The beating pattern of the stimulated network is increased to the stimulation frequency. At the same time, the variations in the beating pattern (standard deviation) is significantly reduced, highlighting the reliability of the stimulation process.

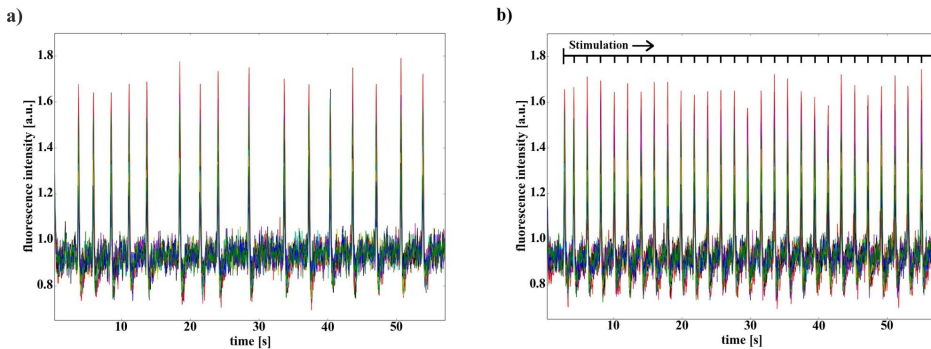


Figure 4.24: Calcium fluorescence signals from 16 regions of interests without (a) and with (b) stimulation. The spontaneous beating activity (no stimulation, a) is rather irregular. When applying voltage pulses, the optical signal follows the regular stimulation pattern (b). The signal applied via the nanocavities thus clearly forces the beating pattern of the HL-1 network to fall in line with the stimulation frequency. Published in [46] and reproduced by permission of The Royal Society of Chemistry.

To further analyze the network response to prolonged stimulation, calcium imaging videos of spontaneous as well as stimulated beating

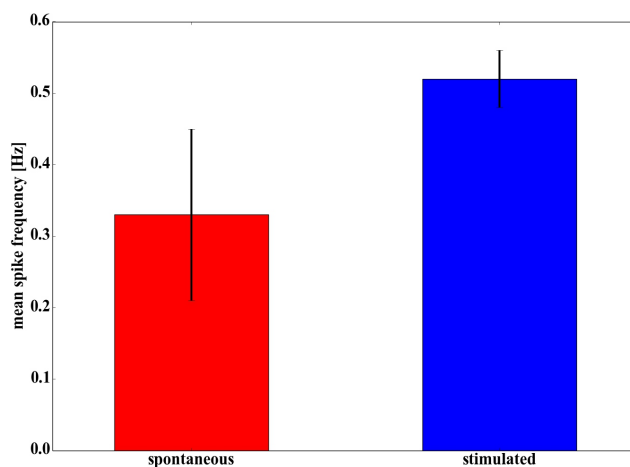


Figure 4.25: Mean spike frequencies, calculated on basis of the cross-correlation analysis of calcium imaging videos. In the stimulated case, the frequency is increased to the stimulation frequency while the variation in the beating pattern is significantly reduced as compared to the spontaneous activity. Published in [46] and reproduced by permission of The Royal Society of Chemistry.

4. Results & Discussion

activity were recorded and subsequently analyzed by a Matlab script to perform a cross-correlation analysis of the local fluorescence intensity. The propagation plots can be seen in Fig. 4.26.

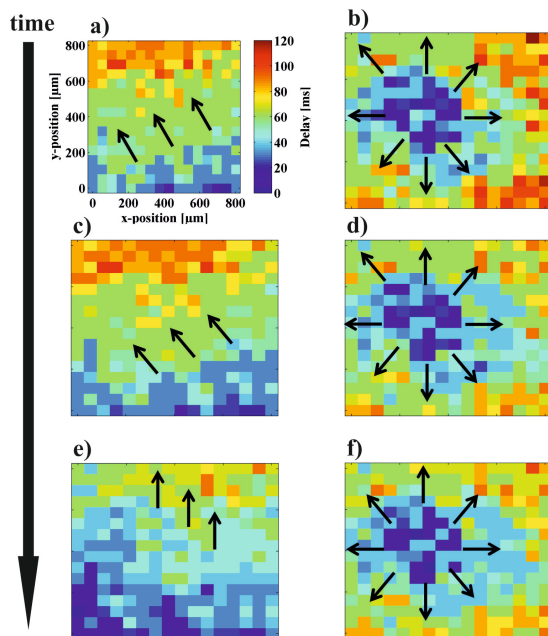


Figure 4.26: Cross-correlation analysis of calcium imaging videos. The time delay of the propagating action potential front is color coded, referring to the color scale in (a). x- and y-axis give the dimensions of the observed sample section. A voltage-controlled stimulation protocol has been applied in every second measurement (b,d,f) to high-jack the cell's pacemaker and change the network's beating behavior. Spontaneous activity can be seen in (a), (c) and (e). Every image represents the same position on the same sample. Published in [46] and reproduced by permission of The Royal Society of Chemistry.

In this experiment, one minute videos with alternating applied and non-applied stimulation protocols were recorded and used for data analysis. While the spontaneous calcium waves starts at the bottom

of the image and propagates to the top, the onset of four electrode stimulation in the center of the sample triggers the calcium wave to originate in the center before propagating to the outer periphery. This “high-jacking” effect on the cells’ pacemaker can be repeated several times. In Fig. 4.26 a cycle of three stimulation onsets is shown. After each stimulation period, the cells return to their intrinsic beating behavior. This influence on the signal conduction could be used in future applications for investigation of cardiac arrhythmia by creating activity patterns connected to fibrillation. After the second stimulation period (Fig. 4.26d) a shift of the wave front to a more horizontal orientation was observed (Fig. 4.26e). Similar effects have been observed during cardiac conduction blocking with high-frequency signals shown in the work of Dura et al. [68]. Also it has been reported, that rapid stimulation can cause electrical remodeling of cardiac cells, which might lead to increased vulnerability to atrial fibrillation [155]. The change in action potential direction could be a transition stage to stimulation induced occurrence of fibrillation phenomena on a cellular level [156].

To sum up, cell-chip communication in both directions, receiving information from the cell system by high SNR action potential recordings as well as feeding in by stimulation and pacing of a HL-1 cell network, could be demonstrated with nanocavity arrays.

4.4 Implementation of an Alternative Cell System

After the device was successfully employed as electrical interface of cells, a next step was the system's extension on a second electrogenic cell model. For that reason, the commercially available ReNcell VM was implemented and different differentiation protocols were investigated. In the end, ReNcells, positively stained for tyrosine hydroxylase (TH, indicating a dopaminergic development) and neuronal character were examined via calcium imaging to gain information about the possible development of action potentials and voltage-controlled stimulation was used to test the existence of voltage-gated ion channels and thus the electrogenic development.

4.4.1 Differentiation Protocols and Immunostaining

Investigations on the differentiation of a dopaminergic and electrically active cell system provided the fundament for two master theses [129, 157]. Here, the findings regarding differentiation of ReNcells towards a neuronal fate are presented. ReNcell VM are reported to develop dopaminergic behavior and action potentials in the differentiated state, and connected with this, to exhibit a tyrosine hydroxylase (TH) expression [59, 60]. To verify the ascribed characteristics, the standard differentiation protocol provided by Millipore (see subsection 3.3.2) was tested as described in [157]. After 21 days of cell differentiation, an immunohistochemical analysis was performed. Figure 4.27 shows

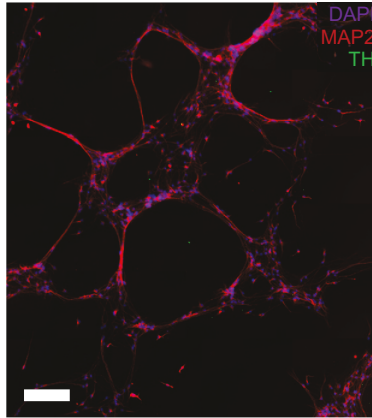


Figure 4.27: Immunostaining of neurosphere-differentiated ReNcell VM against TH, MAP2 and DAPI [157]. No TH positive cells could be identified. The staining against MAP2 indicates a neuronal phenotype. Scale bar: 200 μm .

the staining for TH, microtubule-associated protein 2 (MAP2) and 4,6-Diamidin-2-phenylindol (DAPI, a fluorescent DNA marker used to mark the cell nucleus). MAP2 is a dendrite-specific marker and used to confirm neuronal development. The cells expressed neuronal marker proteins, as MAP2 and showed no functional TH expression. This means, neuronal properties are proven but no dopaminergic characteristics could be assumed.

In a second attempt, a different ReNcell VM culture with a similar passage number was used. The cells were differentiated by the standard protocol for a duration time of 21 days and were stained against MAP2 and TH (Fig. 4.28a). Here, an amount of 8% TH-positive ReNcells could be determined. To gain a higher differentiation success rate and find a more cost-efficient differentiation protocol, two alternatives were evaluated. As described in subsection 3.3.2, the first option is

4. Results & Discussion

based on a heparin supported differentiation documented by Choi et al. [126]. The corresponding staining can be seen in Fig. 4.28b. Here, an amount of 31% of TH-positive cells could be determined. Fig. 4.28c represents the immunostaining by the second method, the cofactor induced differentiation protocol, according to Kirkeby et al. [128]. Kirkeby's method has led to a rather divergent result of 4% TH-positive cells in the depicted image and around 55% for a cell aggregation (data not shown, details given in [129]). The neuronal

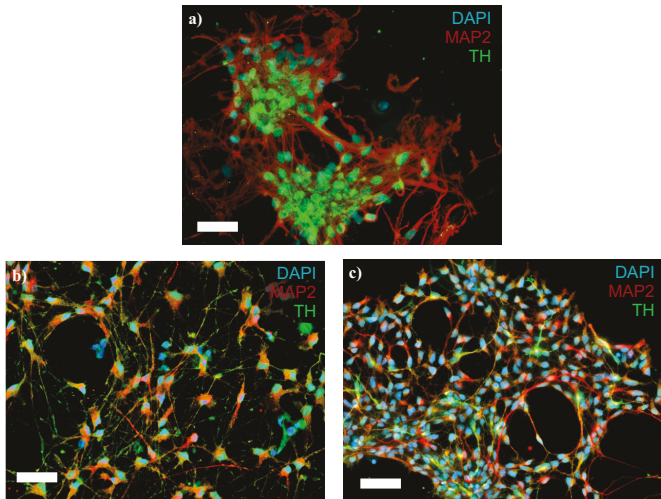


Figure 4.28: Immunostainings against TH, MAP2 and DAPI on ReN-cells treated with the standard Millipore differentiation (a), the heparin supported differentiation (b) and the cofactor-induced differentiation (c). Scale bars: 50 μm .

character could be determined by a MAP2 staining. To aim a higher differentiation rate the heparin-supported differentiation protocol was implemented in further cell experiments.

After all, the examination of different differentiation protocols has revealed the complex differentiation mechanisms towards a dopaminer-

gic cell character. Although a differentiation in a neuron-like cell type seems to be successfully implemented, the in literature reported properties regarding development of a dopaminergic phenotype [59, 60, 123] could not be confirmed in the same scope.

4.4.2 Optical Action Potential Detection

To further investigate the cell's development state and to examine the question of fast voltage-gated channels in the cell membrane, which are necessary for occurrence of action potentials, calcium imaging was performed on differentiated ReNcells. Additionally three different substrate types have been evaluated: polystyrole culture dishes, $\text{SiO}_2/\text{Si}_3\text{N}_4$, and polyimide passivated chips. Spontaneous calcium activity was detected on all three sample types and is displayed in Fig. 4.29, 4.30 and 4.31. The calcium-correlated change in fluorescence intensity has been extracted for different regions of interest (ROIs), marked in the cell images. The colored circles indicate the color code of the corresponding trace of fluorescence intensity. To enable a better relation between the data and cell appearance, in Fig. 4.29, 4.30 and 4.31 the unprocessed fluorescence cell image is depicted, while Fig. 4.32 shows the sequential subtracted image, depicting the intensity change between different frames. Nonetheless, for higher contrast and better visualization, all calcium imaging videos have been recorded in the sequential subtraction mode, as described in subsection 3.4.2.

Although measured on the same cell system, signals differ significantly from each other. One factor here could be different calcium kinetics. To characterize the time scale of the recorded fluorescence signals, representative peaks have been analyzed regarding rise and

4. Results & Discussion

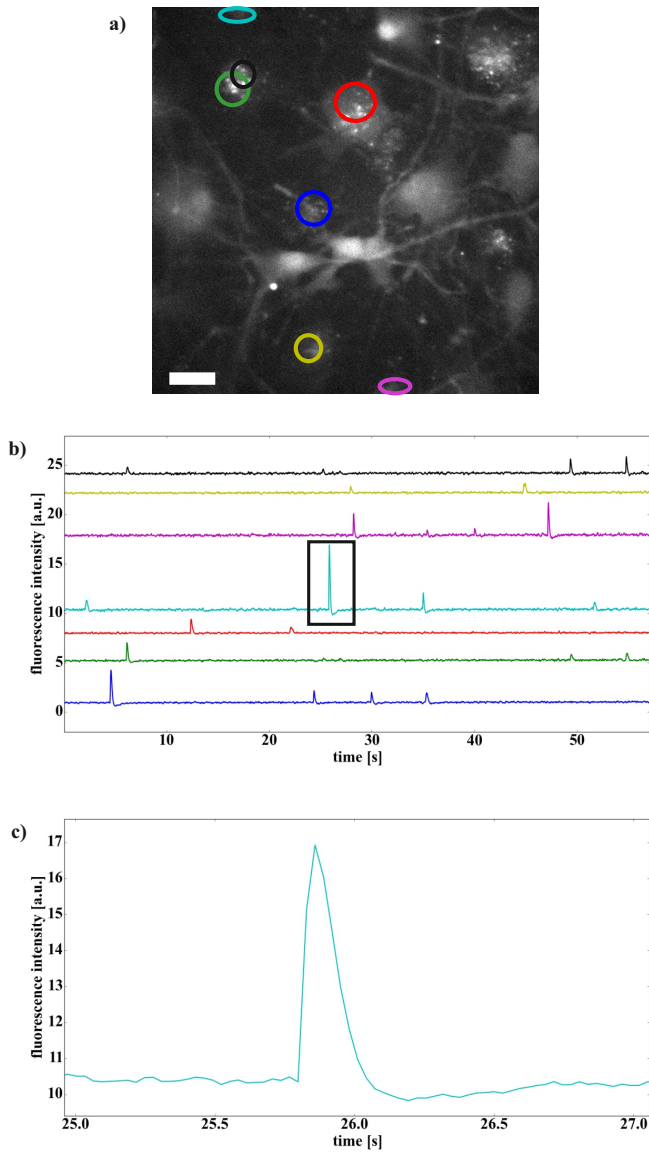


Figure 4.29: Spontaneous calcium activity of differentiated ReNcells on a polystyrene substrate. Depicted are 7 ROIs. Sampling rate approx. 33 Hz. A representative peak shows a FWHM of 0.12s, a rise time of 0.06s and a fall time of 0.18s. Scale bar: 25 μm .

fall time, i.e. time-to-peak and decay kinetics, as well as the full width half maximum (FWHM). As a baseline for these calculations the data median was used, for a more precise adaption to the average noise level. Time values were rounded to two decimal places. It becomes clear, that two types of spontaneous cellular calcium signals have been measured. The spontaneous signals in Fig. 4.29 and 4.30 were recorded on a cell sample differentiated for 21 days, following the original Millipore differentiation protocol. Two representative peaks are magnified. The FWHM of the two fluorescence peaks is 0.12 s or 0.16 s, respectively, while their rise times are 0.06 s and 0.15 s and their fall times 0.18 s and 0.95 s. These fluorescence signals show a hyperpolarization-like undershoot, e.g. a signal dip underneath the baseline. This signal shape is typical for electrical action potential recordings. But in this case it is ascribed to artifacts of the video processing by sequential subtraction. The calcium depletion underneath the pre-spike level should be too small to be detected here.

The second type of spontaneous signal is pictured in Fig. 4.31 and 4.32 and has been recorded on a $\text{SiO}_2/\text{Si}_3\text{N}_4$ passivated chip. The corresponding time values here are 1.02 s (3.05 s) for the FWHM, 1.01 s (4.00 s) rise time and 1.92 s (5.22 s) fall time. Further, the fluorescence increase in the videos of Fig. 4.29 and 4.30 seems to occur in a region limited to the cell soma with a blinking appearance, while the video forming the basis for Fig. 4.31 shows the propagation of the calcium signal along the neurites. Although there are no voltage-gated calcium channels in the myelin area and the Ranvier node of the fully differentiated axon, T- and R-type voltage-gated calcium channels are documented in the axon initial segment (AIS) [158]. Further, Kalil and Hutchins [159] report that calcium activity measured in axons and

4. Results & Discussion

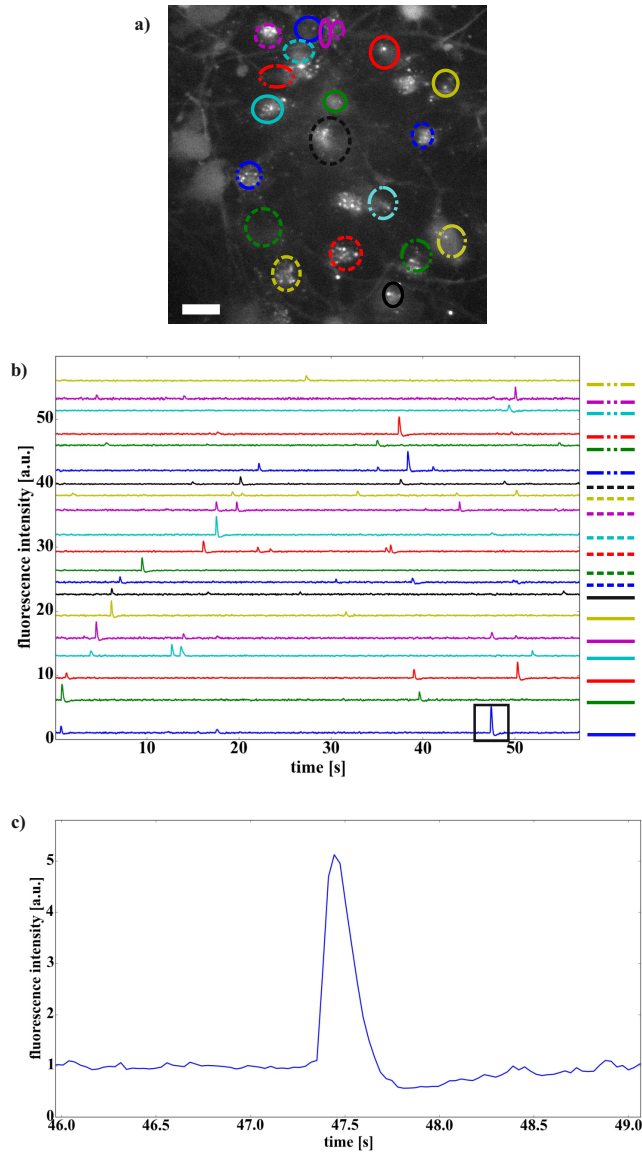


Figure 4.30: Calcium imaging on differentiated ReNcells on a polystyrole substrate with a high activity. Depicted are 20 ROIs. FWHM: 0.16 s, rise time: 0.15 s, fall time: 0.95 s. Scale bar: 25 μm .

its branches is related to axon pathfinding, outgrowth and branching. Electrical activity and calcium signaling is involved in all three phases (proliferation, migration and differentiation) of neural development and thus, the generation and propagation of transient elevations of intracellular calcium involved in the growth cone of neurons is well-known [160]. Despite that, calcium sparks in dendrites can occur with a time scale of several hundred ms [161]. Beside the effect of glial signaling, these phenomena of calcium signaling outside the soma have to be taken into account when evaluating the observed propagating signal character along the neurites and can be an indication of a not completed differentiation state of the examined cells.

The two discussed signal types with fast localized and slow propagating properties can not be accurately compared, since they can be interpreted as different parts of the cell's signaling apparatus. Even so, it is evident that the short signal type shows a locally defined spiking behavior on a time scale one order of magnitude lower than the time scale of the slower signal type, which occurred also in the soma, but shows a propagating intracellular calcium increase as well.

Cells with those slow calcium dynamics were observed parallel to cells with the fast signals, but with a low incidence. Further, slow signals were also observed on polystyrol substrates, ruling out the influence of substrate composition on this aspect of cell development. An influence of the substrate material is visualized in 4.32. This signal has been measured on a PI passivated chip and shows a signal-to-noise ratio (SNR) of approx. 29 (peak-to-peak amplitude vs. RMS noise), while the signal measured with a $\text{SiO}_2/\text{Si}_3\text{N}_4$ passivated chip (Fig. 4.31) has a SNR of approx. 180, which is about six times higher. The reason for this is autofluorescence of polyimide [162–164] with a wavelength in

4. Results & Discussion

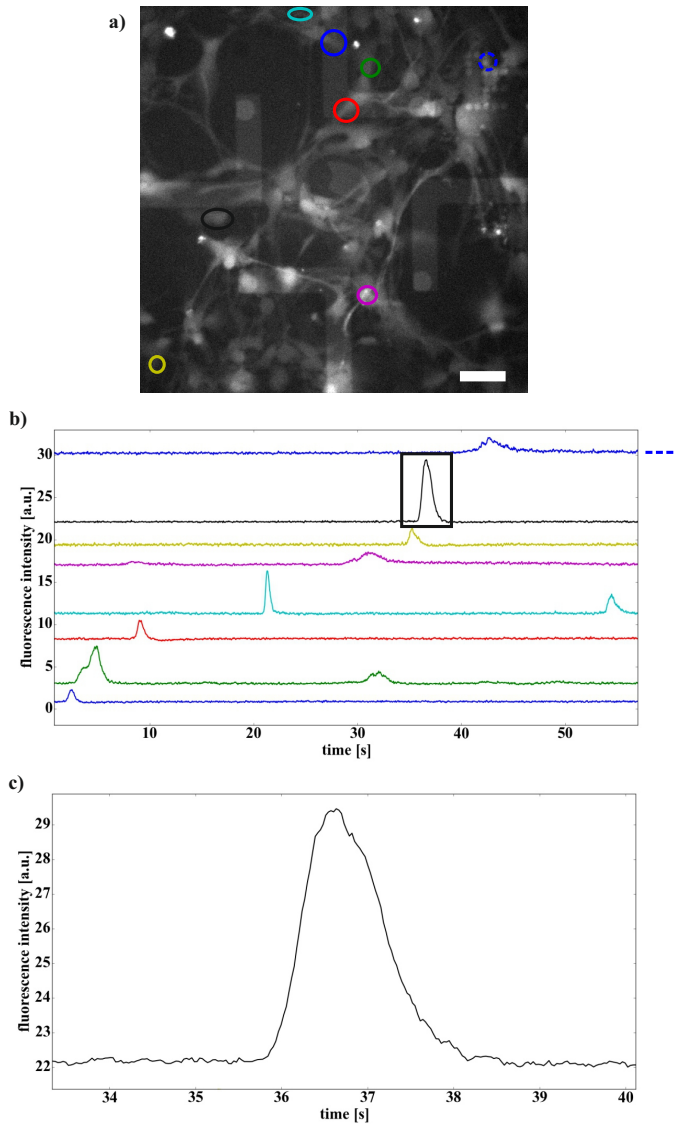


Figure 4.31: Spontaneous calcium activity of differentiated ReN cells on a $\text{SiO}_2/\text{Si}_3\text{N}_4$ passivated chip. The investigated cell areas are indicated in the fluorescence images on the left side. FWHM: 1.02 s, rise time: 1.01 s, fall time: 1.92 s. Scale bar: 50 μm .

the range of 515–555 nm (equivalent to green) and which is co-imaged with the green fluorescence of the calcium indicator Fluo-4. Thus, this passivation material is not optimal for fluorescence investigations based on Fluo-4, although ReNcell VM show a better differentiation behavior on PI passivation than on $\text{SiO}_2/\text{Si}_3\text{N}_4$ (see subsection 3.3.2).

The fast signals correspond to results reported for neuronal AP detection by calcium imaging. Smetters et al. [165] report on calcium signals from neuronal action potentials occurring in the soma with a time-to-peak of around 10-40 ms and decay kinetics of 1-5 s, recorded with camera frame rates of 50-200 Hz. The rise time here is approximately in the same order of magnitude compared to that shown for the short signals, while the decay time is about one order of magnitude longer. After all, the here depicted short calcium signals have a similar time scale to the action potential caused signals presented in literature [165]. Therefore it can be assumed, that the transient calcium peaks in the ReNcell somata are action potential related.

Identifying single action potentials or action potential bursts from calcium signals remains challenging [166–168]. A first limitation is set here by the sampling rate of the recordings. All calcium imaging videos processed in this thesis have been recorded with a maximal sampling rate of approx. 33 Hz. According to Quan et al. [168] AP burst firing sequences can consist of APs with intervals of less than 20 ms, while they record fluorescence signals with a sampling rate of 1kHz. Regarding the signals shown in Fig. 4.29-4.31 it is to be assumed, that some information is lost due to undersampling of the underlying signal. Since the identification of single APs from bursting firing can be done by analyzing the signals' rise time [168], due to a lack of signal resolution it can not be stated here, whether the measured signals

4. Results & Discussion

correlate to single events or AP bursts. A drawback lies in the method of calcium imaging itself. Calcium dynamics are generally slower than APs and the calcium signals can become saturated with increasing events, leading to another uncertainty in relating calcium and potential spikes. Additionally the process of AM ester loading is cell dependent because it relates to intracellular enzymatic cleavage. This means, the loading efficiency can differ from cell to cell [167]. Finally, calcium signals are not exclusively coupled to action potential occurrence [166] as it will be further elaborated next by taking a closer look at the slow calcium kinetics observed in ReNcells.

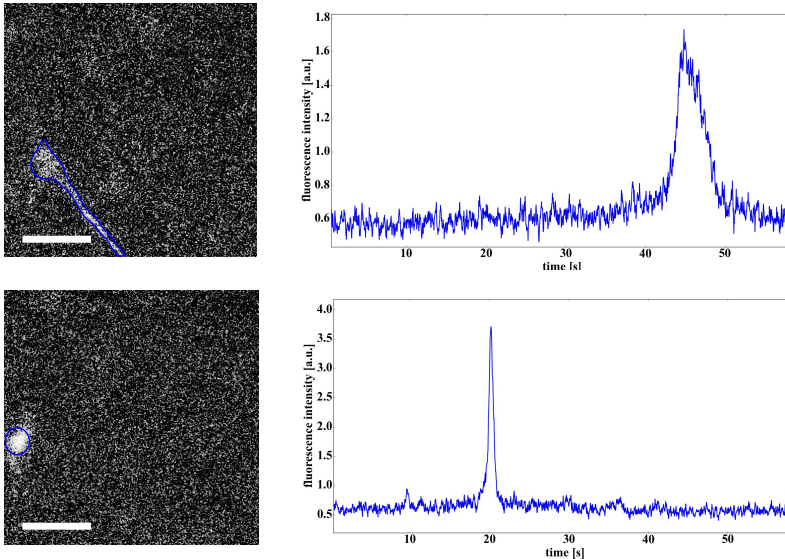


Figure 4.32: Spontaneous calcium activity of differentiated ReNcells on a PI passivated chip. FWHM: 3.05 s, rise time: 4.00 s, fall time: 5.22 s. Scale bar: 25 μm .

A versatile range of ion channels, pumps and buffers are included in maintaining the cellular calcium gradient as well as in excitatory

calcium signaling [169]. Besides the fast $\text{Na}^+/\text{Ca}^{2+}$ exchanger and voltage-gated Ca^{2+} selective channels, which are included in the generation of action potentials, transient receptor potential (TRP) channels are a predominant source of calcium influx in human embryonic stem cell-derived neural epithelial cells and developing neurons [124]. Morgan et al. [124] further provided proof that these channels are the major source of spontaneous calcium signaling in both proliferating and neurosphere-supported (see subsection 3.3.2) differentiating ReNcells and that calcium transients in these cells are thought to be almost entirely due to calcium influx from the extracellular space. The reported signals have been investigated in a control group and different medium conditions and appeared at around 50% of proliferating cells and around 30% of differentiating cells. The signal frequency here ranges from 2.9 mHz for the control group of proliferating cells up to 4.2 Hz, corresponding to time ranges of 5.78 min and 0.24 s. For differentiating cells, frequency ranges of 0.2 Hz up to 4.2 Hz are given, corresponding to 5 s and 0.24 s. Another signal source, which should be considered here are the calcium dynamics of astrocytes [170]. According to the distributor and literature [59, 60], ReNcell VM are also able to differentiate into neuronal subtypes, including oligodendrocytes and astrocytes. The calcium fluorescence signals documented by Hirase et al. [170] show a rather wide time scale of 5-50 s and thus seem to be too long to match the dynamics shown in Fig. 4.31 and 4.32. But still, a possible astrocyte contribution cannot be completely excluded here.

To sum up, the slow calcium dynamics measured on differentiated ReNcells could be attributed to comparably slow TRP channels, which are reported to be weakly voltage-sensitive [169]. This property might

also play a role in the analysis of stimulated ReNcells in the next subsection.

4.4.3 Voltage-Controlled Stimulation

To further approach the goal of developing an alternative electrogenic cell system, stimulation experiments were performed on differentiated ReNcells. The intention here was to evaluate their electrical behavior and to confirm the existence of voltage-gated ion channels. Fig. 4.33 displays the voltage-controlled stimulation with a PI passivated Ti/Au/Cr nanocavity array. The cells were prepared at passage 12 and differentiated on chip for 33 days with the alternative heparin differentiation protocol presented in subsection 3.3.2. A pulse with a 0.8 V amplitude, a frequency of 250 Hz and a duration of 300 ms has been applied and the cell response in calcium fluorescence was recorded. An unsubtracted fluorescent cell image is provided to mark the position of the stimulation electrode with an electrode opening of 12 μm . It can be seen, that the stimulation response starts directly above the stimulation electrode and propagates to another cell. The soma excitation is clearly visible, before the fluorescence signals assume a rather diffuse behavior with decreased amplitude including propagation along neurites and point-like fluorescent areas. The obtained calcium fluorescence signals appear on a time scale around one to several seconds, thus can be categorized as the slow TRP channel attributed ReNcell signals discussed in the last subsection.

Park et al. have demonstrated voltage-controlled stimulation of differentiated ReNcells with a graphene covered electrode [171] and evaluated the stimulation response by calcium imaging with Fluo-4

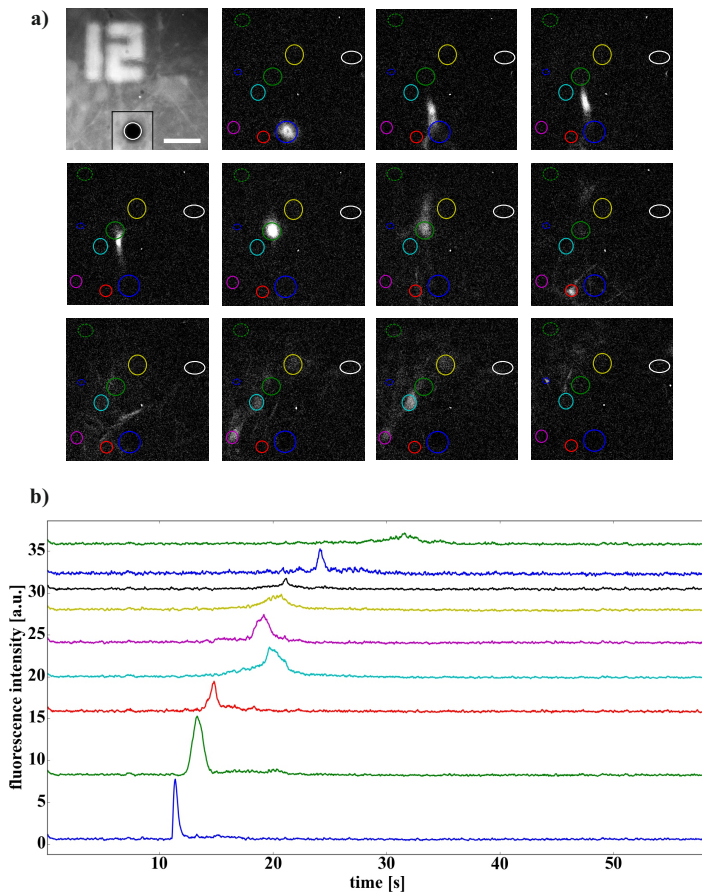


Figure 4.33: Voltage-controlled stimulation with a PI passivated Ti/Au/Cr nanocavity array. An additional unsubtracted fluorescent cell image is provided to mark the position of the stimulation electrode. Scale bar: 50 μm .

as the indicator. They report a long-lasting stimulation response in the range of several minutes and interpret these signals as proof for neuronal function of the cells. By staining for GFAP (glial fibrillary acidic protein) and TUJ1 (neuron-specific class III beta-tubulin) they further estimated the percentage of glial cells and neurons to be approx. 23% and 40% respectively on a graphene covered device and 35% and 33% respectively on a glass surface. Although stimulation of neurons combined with Fluo-4 calcium imaging was performed by Wang et al. [37] with a similar result by observing fluorescence peaks on a time scale of several seconds, it seems to be questionable if slow calcium dynamics can be counted as proof of neuronal cell fate. This impression is supported in particular by considering the high amount of glial cells reported by Park et al. [171] and the signal discussion of two different calcium processes in the last section.

Recapitulatory, the spontaneous activity of differentiated ReNcell VM could be proven and different signal types identified, indicating different development paths in neuronal differentiation. Despite the uncertainty of a complete differentiation into neurons and a readily developed calcium signaling pathway, the stimulation experiments have shown that differentiated ReNcells develop voltage-sensitive calcium ion channels.

Although stimulated ReNcell calcium activity on a long time scale is documented in literature [171], the ReNcell signaling observations could be supplemented here by documentation of a propagating signal behavior in a cell network, thus revealing different calcium signaling mechanisms in ReNcell differentiation. Further, findings could be complemented by measuring fast spontaneous calcium signals, which could be attributed to action potential occurrence.

Chapter 5

Conclusion & Outlook

Within the scope of this thesis, a novel approach for microelectrode array (MEA) functionalization by introducing nanocavities is presented as an widely applicable, efficient and well controlled way to improve electrode characteristics for on-chip electrophysiology. This represents a promising contribution addressing challenges of transducer design for communication between electronical and biological systems.

The fabrication process significantly enhances the sensor performance by lowering the electrode impedance and promotes cell-sensor sealing by allowing cells to protrude into the cavity. The devices provide both a large electrode surfaces and a small microaperture, which preserves the spatial resolution. The improved fabrication method is independent from CMOS technology and the postprocessing by wet-etching can be done in a standard chemical lab environment. The

cavity fabrication does not require any additional lithography steps, by which alignment problems of the sacrificial layer can be avoided.

The sensor concept has further been complemented with the nanostructuring of the electrode layer by utilizing not only the chromium adhesion layer of a conventional MEA, but also the heating step included in the fabrication. This is done by the attempt to easily increase the surface area of the electrode and thus further decreasing the sensor impedance and additionally provide a rough surface, beneficial for cell adhesion. A distinct surface roughening was demonstrated for gold electrodes, whereas platinum electrodes showed only a small increase in surface roughness and therefore was not pursued further in this work.

The underlying process of gold diffusion into chromium was characterized, revealing several possible influences on the surface capacitance: organic contamination, metallic impurities, fissures by thermal stress as well as material mixing with increasing annealing temperature due to alloy formation. Also the temperature dependence of the interdiffusion was shown and an onset temperature of approx. 200 °C estimated.

Finally, the presented device was successfully applied for cell applications. By FIB sectioning, a tight contact between cell and nanocavity sensor could be demonstrated and action potential recordings were performed, documenting a high signal-to-noise ratio. Further, the pacing of a HL-1 network was accomplished by voltage-controlled stimulation.

Towards the implementation of an alternative electrogenic cell system, the commercially available ReNcell VM was differentiated and its neuronal character could be proven by MAP2 staining. Also TH-positive cells were identified, indicating a dopaminergic development of the cells. Further, the spontaneous calcium activity of differentiated

cells could be observed. Here, signal types with different time scales were recorded supposing an incomplete differentiation path, although voltage-gated stimulation of the cell network could show the development of voltage-gated ion channels.

Nanocavity arrays show great potential for on-chip electrophysiology and the presented device further provides possibilities for investigation of intercellular communication as well as cardiac phenomena like stimulation-induced arrhythmia and pacing. Due to their beneficial performance in extracellular recording and highly resolved multi-channel measurements, additional prospectes can be seen in investigation of cellular networks regarding drug development, which is known for conventional MEAs [172]. In general it was shown, that the introduction of nanocavities to a conventional MEA is improving its electrode impedance and thus its recording capabilities. Therefore, a transfer of this concept of electrode modification can generally lead to sensor improvement, also for other than standard MEA device geometries.

Future applications lie also in the combination of nanocavity devices and guided cell growth. Guided neurites growing into a functionalized cavity could improve cell-chip coupling for localized action potential as well as neurotransmitter recording and investigations on cellular communication. It has been shown, that HL-1 cells can grow into the cavity channel. To expand the concept on other cell systems, the viability and adhesion of neural cells on the diffusion structures have to be examined in detail. In literature it has been reported [44], that the neuronal cell body avoids gold nanopillar structures. Thus, evidence has to be found whether neuronal cells show the same behavior on the here presented nanostructuring by interdiffusion. Besides, the question

of neurite adhesion has to be evaluated. The finding of a beneficial passivation material for ReNcell VM differentiation can maybe lead to improved on-chip cultivation of other neuron-like or neuronal cell types.

For more detailed cell adhesion and viability studies, complementing investigations need to be carried out on the surface structuring. Here, more data is needed regarding the exact material composition for high temperature processing for a better understanding of surface energy effects, which again is crucial for the functionality of adhesion proteins. To maximize the structuring effect, the influence of material mixing on the electronic device properties needs to be further evaluated. A better control of the temperature-initiated process can lead to a optimization of the surface structuring in terms of a high structuring effect without the occurrence of defects like thermal fissures. Especially the effect of 300 °C and 400 °C annealing demands further attention, since the impression of a common structural or surface chemical effect was received, altering surface energy and capacitive behavior.

Regarding the differentiation of ReNcell VM, it is still not clear if the calcium signaling pathway and mechanism of dopamine generation are readily developed, thus further experiments are required not only on neurotransmitter release, but also on electrical proof of action potential generation, for example by extracellular and patch-clamp recordings. A promising protocol for development of dopaminergic and electrical active cells has been found and spontaneous activity observed as well as the cell's response to extracellular stimulation. Hence, this cell line represents a potential alternative to electrogenic and dopaminergic primary neurons, which could be combined in future with the nanocavity perspectives in guided growth and localized neurotransmitter detection.

The presented study on nanocavity arrays for action potential recordings and stimulation of cell systems has introduced a novel approach for efficiently interfacing biological cells and tissue and has further revealed interesting impulses towards the investigation and extended application of functionalized sensor surfaces.

References

- [1] Willner, I. & Katz, E. *Bioelectronics* (Wiley-VCH Verlag GmbH & Co. KGaA, Weinheim, 2005).
- [2] DIYBIO. URL diybio.org.
- [3] Bulletproof Biohacking Conference (2015). URL <https://bulletproofconference.com/bp-conference-2015>.
- [4] Forum biohack.me. URL <http://forum.biohack.me/>.
- [5] Wikipedia entry "Cyborg". URL <https://en.wikipedia.org/wiki/Cyborg>.
- [6] Chislenko, A. Technology as extension of human functional architecture (1997). URL <http://www.lucifer.com/~sasha/articles/techuman.html>.
- [7] Rathbun, D. L., Jalligampala, A., Member, S., Stingl, K. & Zrenner, E. To What Extent Can Retinal Prostheses Restore Vision? In *7th Annual International IEEE EMBS Conference on Neural Engineering*, 22–24 (Montpellier, 2015).
- [8] Jiang, N., Dosen, S. & Farina, D. Myoelectric control of artificial limbs - is there a need to change focus? *IEEE Signal Processing Magazine* **152** (2012).

- [9] Zeng, F.-G., Popper, A. N. & Fay, R. R. (eds.) *Cochlear implants: auditory prostheses and electric hearing* (Springer Science+Business Media, New York, 2004).
- [10] Al-Ahmad, A., Ellenbogen, K. A., Natale, A. & Wang, P. J. (eds.) *Pacemakers and implantable cardioverter defibrillators* (Cardiotext Publishing, 2010).
- [11] Jahnke, H.-G. *et al.* An impedimetric microelectrode-based array sensor for label-free detection of tau hyperphosphorylation in human cells. *Lab on a Chip* **9**, 1422–1428 (2009).
- [12] Cui, H.-F. *et al.* In situ temporal detection of dopamine exocytosis from l-dopa-incubated MN9D cells using microelectrode array-integrated biochip. *Sensors and Actuators, B: Chemical* **115**, 634–641 (2006).
- [13] Xiang, G. *et al.* Microelectrode array-based system for neuropharmacological applications with cortical neurons cultured in vitro. *Biosensors & Bioelectronics* **22**, 2478–84 (2007). URL <http://www.ncbi.nlm.nih.gov/pubmed/17071071>.
- [14] Blau, A. *et al.* Characterization and optimization of microelectrode arrays for in vivo nerve signal recording and stimulation. *Biosensors & Bioelectronics* **12**, 883–92 (1997). URL <http://www.ncbi.nlm.nih.gov/pubmed/9451781>.
- [15] Rutten, W. L. C. Selective electrical interfaces with the nervous system. *Annual Review of Biomedical Engineering* **4**, 407–52 (2002). URL <http://www.ncbi.nlm.nih.gov/pubmed/12117764>.
- [16] Hierlemann, A., Frey, U., Hafizovic, S. & Heer, F. Growing cells atop microelectronic chips: interfacing electrogenic cells in vitro with CMOS-based microelectrode arrays. *Proceedings of the IEEE* **99**, 252–284 (2011). URL <http://ieeexplore.ieee.org/lpdocs/epic03/wrapper.htm?arnumber=5594982>.

-
- [17] Heer, F. *et al.* CMOS microelectrode array for the monitoring of electrogenic cells. *Biosensors & Bioelectronics* **20**, 358–66 (2004). URL <http://www.ncbi.nlm.nih.gov/pubmed/15308242>.
- [18] Stoelzle, S. *et al.* State-of-the-art automated patch clamp devices: heat activation, action potentials, and high throughput in ion channel screening. *Frontiers in pharmacology* **2**, 76 (2011). URL <http://www.pubmedcentral.nih.gov/articlerender.fcgi?artid=3223389&tool=pmcentrez&rendertype=abstract>.
- [19] Hamill, O. P., Marty, A., Neher, E., Sakmann, B. & Sigworth, F. J. Improved patch-clamp techniques for high-resolution current recording from cells and cell-free membrane patches. *Pflügers Archiv: European Journal of Physiology* **391**, 85–100 (1981).
- [20] Chow, R. H., von Rüden, L. & Neher, E. Delay in vesicle fusion revealed by electrochemical monitoring of single secretory events in adrenal chromaffin cells. *Nature* **356**, 60–63 (1992).
- [21] Breckenridge, L. J. *et al.* Advantages of using microfabricated extracellular electrodes for in vitro neuronal recording. *Journal of Neuroscience Research* **42**, 266–76 (1995). URL <http://www.ncbi.nlm.nih.gov/pubmed/8568928>.
- [22] Yakushenko, A., Kätelhön, E. & Wolfrum, B. Parallel on-chip analysis of single vesicle neurotransmitter release. *Analytical Chemistry* **85**, 5483–90 (2013). URL <http://www.ncbi.nlm.nih.gov/pubmed/23642073>.
- [23] Wang, J., Trouillon, R., Lin, Y., Svensson, M. I. & Ewing, A. G. Individually addressable thin-film ultramicroelectrode array for spatial measurements of single vesicle release. *Analytical Chemistry* (2013).
- [24] Blau, A. Cell adhesion promotion strategies for signal transduction enhancement in microelectrode array in vitro electrophysiology: An introductory overview and critical discussion. *Current Opinion in Colloid & Interface Science* **18**, 481–492 (2013). URL <http://linkinghub.elsevier.com/retrieve/>
-

pii/S1359029413000976.

- [25] Pine, J. Recording action potentials from cultured neurons with extracellular microcircuit electrodes. *Journal of Neuroscience Methods* **2**, 19–31 (1980).
- [26] Heuschkel, M. O., Fejtl, M., Raggenbass, M., Bertrand, D. & Renaud, P. A three-dimensional multi-electrode array for multi-site stimulation and recording in acute brain slices. *Journal of Neuroscience Methods* **114**, 135–48 (2002). URL <http://www.ncbi.nlm.nih.gov/pubmed/11856564>.
- [27] Griscom, L., Degenaar, P., Lepiou, B., Tamiya, E. & Fujita, H. Techniques for patterning and guidance of primary culture neurons on micro-electrode arrays. *Sensor Actuator* **83**, 15–21 (2002).
- [28] Spira, M. E. & Hai, A. Multi-electrode array technologies for neuroscience and cardiology. *Nature Nanotechnology* **8**, 83–94 (2013). URL <http://www.ncbi.nlm.nih.gov/pubmed/23380931>.
- [29] Wesche, M. *et al.* A nanoporous alumina microelectrode array for functional cell-chip coupling. *Nanotechnology* **23**, 495303 (2012). URL <http://www.ncbi.nlm.nih.gov/pubmed/23150042>.
- [30] Brüggemann, D. *et al.* Nanostructured gold microelectrodes for extracellular recording from electrogenic cells. *Nanotechnology* **22**, 265104 (2011). URL <http://www.ncbi.nlm.nih.gov/pubmed/21586820>.
- [31] Hai, A., Shappir, J. & Spira, M. E. In-cell recordings by extracellular microelectrodes. *Nature Methods* **7**, 200–2 (2010). URL <http://www.ncbi.nlm.nih.gov/pubmed/20118930>.
- [32] Santoro, F., Schnitker, J., Panaitov, G. & Offenhäusser, A. On chip guidance and recording of cardiomyocytes with 3D mushroom-shaped electrodes. *Nano Letters* **13**, 5379–84 (2013). URL <http://www.ncbi.nlm.nih.gov/pubmed/24088026>.

-
- [33] Cohen-Karni, T., Timko, B. P., Weiss, L. E. & Lieber, C. M. Flexible electrical recording from cells using nanowire transistor arrays. *Proceedings of the National Academy of Sciences of the United States of America* **106**, 7309–13 (2009). URL <http://www.pubmedcentral.nih.gov/articlerender.fcgi?artid=2678623&tool=pmcentrez&rendertype=abstract>.
- [34] Beckman, R. A. *et al.* Fabrication of conducting Si nanowire arrays. *Journal of Applied Physics* **96**, 5921 (2004). URL <http://scitation.aip.org/content/aip/journal/jap/96/10/10.1063/1.1801155>.
- [35] Meng, E. & Erickson, J. O. N. Biocompatible parylene neurocages. *IEEE Engineering in Medicine and Biology Magazine* 30–33 (2005).
- [36] Dankerl, M. *et al.* Graphene solution-gated field-effect transistor array for sensing applications. *Advanced Functional Materials* **20**, 3117–3124 (2010). URL <http://doi.wiley.com/10.1002/adfm.201000724>.
- [37] Wang, K., Fishman, H. A., Dai, H. & Harris, J. S. Neural stimulation with a carbon nanotube microelectrode array. *Nano Letters* **6**, 2043–2048 (2006). URL <http://dx.doi.org/10.1021/nl061241t>.
- [38] Luo, X., Weaver, C. L., Zhou, D. D., Greenberg, R. & Cui, X. T. Highly stable carbon nanotube doped poly(3,4-ethylenedioxythiophene) for chronic neural stimulation. *Biomaterials* **32**, 5551–7 (2011). URL <http://www.pubmedcentral.nih.gov/articlerender.fcgi?artid=3109196&tool=pmcentrez&rendertype=abstract>.
- [39] Bareket-Keren, L. & Hanein, Y. Carbon nanotube-based multi electrode arrays for neuronal interfacing: progress and prospects. *Frontiers in Neural Circuits* **6**, 122 (2012). URL <http://www.pubmedcentral.nih.gov/articlerender.fcgi?artid=3540767&tool=pmcentrez&rendertype=abstract>.
-

- [40] David-Pur, M., Bareket-Keren, L., Beit-Yaakov, G., Raz-Prag, D. & Hanein, Y. All-carbon-nanotube flexible multi-electrode array for neuronal recording and stimulation. *Biomedical Microdevices* **16**, 43–53 (2014). URL <http://www.pubmedcentral.nih.gov/articlerender.fcgi?artid=3921458&tool=pmcentrez&rendertype=abstract>.
- [41] Chuang, M.-C., Lai, H.-Y., Annie Ho, J.-A. & Chen, Y.-Y. Multifunctional microelectrode array (mMEA) chip for neural-electrical and neural-chemical interfaces: characterization of comb interdigitated electrode towards dopamine detection. *Biosensors & Bioelectronics* **41**, 602–7 (2013). URL <http://www.ncbi.nlm.nih.gov/pubmed/23083904>.
- [42] Hofmann, B., Kätelhön, E., Schottdorf, M., Offenhäusser, A. & Wolfrum, B. Nanocavity electrode array for recording from electrogenic cells. *Lab on a Chip* 0–4 (2011).
- [43] Schottdorf, M., Hofmann, B., Kätelhön, E., Offenhäusser, A. & Wolfrum, B. Frequency-dependent signal transfer at the interface between electrogenic cells and nanocavity electrodes. *Physical Review E* **85**, 031917 (2012). URL <http://link.aps.org/doi/10.1103/PhysRevE.85.031917>.
- [44] Brüggemann, D., Michael, K. E., Wolfrum, B. & Offenhäusser, A. Adhesion and survival of electrogenic cells on gold nanopillar array electrodes. *International Journal of Nano and Biomaterials* **4**, 108–127 (2012). URL <http://www.ingentaconnect.com/content/ind/ijnbm/2012/00000004/00000002/art00003>.
- [45] Czeschik, A., Offenhäusser, A. & Wolfrum, B. Fabrication of MEA-based nanocavity sensor arrays for extracellular recording of action potentials. *Physica Status Solidi (a)* **211**, 1462–1466 (2014). URL <http://doi.wiley.com/10.1002/pssa.201330365>.
- [46] Czeschik, A. *et al.* Nanostructured cavity devices for extracellular stimulation of HL-1 cells. *Nanoscale* 9275–

-
- 9281 (2015). URL <http://pubs.rsc.org/en/Content/ArticleLanding/2015/NR/C5NR01690H>.
- [47] Sackmann, E. & Merkel, R. *Lehrbuch der Biophysik* (Wiley-VCH Verlag GmbH & Co. KGaA, 2010), 1 edn.
- [48] Dudel, J. Innerneurale Homeostase und Kommunikation, Erregung. In Schmidt, R. F. (ed.) *Neuro- und Sinnesphysiologie*, 31–58 (Springer, 1998), 3 edn.
- [49] Physiologyweb. Neuronal Action Potential - Introduction (2015). URL http://www.physiologyweb.com/lecture_notes/neuronal_action_potential/neuronal_action_potential_introduction.html.
- [50] Wikipedia entry "Threshold Potential" (2015). URL https://en.wikipedia.org/wiki/Threshold_potential.
- [51] Wikipedia entry "Cardiac Action Potential" (2015). URL https://en.wikipedia.org/wiki/Cardiac_action_potential.
- [52] Maybeck, V. *Tools for Non-Invasive Communication with Electrogenic Cells: Optogenetic Stimulation and Diamond Recording Devices*. Ph.D. thesis (2011). URL <http://darwin.bth.rwth-aachen.de/opus/volltexte/2012/3963/>.
- [53] Klabunde, R. E. Cardiovascular Physiology Concepts (2015). URL <http://www.cvphysiology.com/Arrhythmias/A004.htm>.
- [54] Wikipedia entry "Pacemaker Potential" (2015). URL <http://de.wikipedia.org/wiki/Zellmembran>.
- [55] Hodgkin, A. L. & Huxley, A. F. Currents carried by sodium and potassium ions through the membrane of the giant axon of Loligo. *J. Physiol.* **116**, 449–472 (1952).
- [56] Johnston, D. & Miao-Sin Wu, S. *Foundations of Cellular Neurophysiology* (The MIT Press, Cambridge, Massachusetts, 1995).
-

- [57] Pereda, A. E. Electrical synapses and their functional interactions with chemical synapses. *Nature Reviews: Neuroscience* **15**, 250–63 (2014). URL <http://www.ncbi.nlm.nih.gov/pubmed/24619342>.
- [58] Claycomb, W. C. *et al.* HL-1 cells: a cardiac muscle cell line that contracts and retains phenotypic characteristics of the adult cardiomyocyte. *Proceedings of the National Academy of Sciences of the United States of America* **95**, 2979–84 (1998).
- [59] Corteling, R. L. & Miljan, E. A. ReNcell VM Cell Line - A Model of Human Neural Development and Differentiation - Millipore. *Millipore Corporation, Billerica, MA 01821 U.S.A.* 1–3 (2008).
- [60] Donato, R. *et al.* Differential development of neuronal physiological responsiveness in two human neural stem cell lines. *BMC Neuroscience* **8**, 36 (2007). URL <http://www.pubmedcentral.nih.gov/articlerender.fcgi?artid=1888696&tool=pmcentrez&rendertype=abstract>.
- [61] Novak, J. L. & Wheeler, B. C. Multisite hippocampal slice recording and stimulation using a 32 element microelectrode array. *Journal of Neuroscience Methods* **23**, 149–59 (1988). URL <http://www.ncbi.nlm.nih.gov/pubmed/3357355>.
- [62] Gross, G. W., Rhoades, B. K., Azzazy, H. M. & Wu, M. C. The use of neuronal networks on multielectrode arrays as biosensors. *Biosensors & Bioelectronics* **10**, 553–67 (1995). URL <http://www.ncbi.nlm.nih.gov/pubmed/7612207>.
- [63] Eversmann, B. *et al.* A 128 x 128 CMOS biosensor array for extracellular recording of neural activity. *IEEE Journal of Solid-State Circuits* **38**, 2306–2317 (2003). URL <http://ieeexplore.ieee.org/lpdocs/epic03/wrapper.htm?arnumber=1253878>.
- [64] Nam, Y., Wheeler, B. C. & Heuschkel, M. O. Neural recording and stimulation of dissociated hippocampal cultures using microfabricated three-dimensional tip electrode array. *Journal of Neuroscience Methods* **155**, 296–9 (2006). URL <http://www>.

- ncbi.nlm.nih.gov/pubmed/16494949.
- [65] Yeung, C. K. *et al.* Drug profiling using planar microelectrode arrays. *Analytical and Bioanalytical Chemistry* **387**, 2673–80 (2007). URL <http://www.ncbi.nlm.nih.gov/pubmed/17318515>.
- [66] Berdondini, L. *et al.* Active pixel sensor array for high spatio-temporal resolution electrophysiological recordings from single cell to large scale neuronal networks. *Lab on a Chip* **9**, 2644–51 (2009). URL <http://www.ncbi.nlm.nih.gov/pubmed/19704979>.
- [67] Wagenaar, D. A., Pine, J. & Potter, S. M. An extremely rich repertoire of bursting patterns during the development of cortical cultures. *BMC Neuroscience* **7**, 11 (2006). URL <http://www.pubmedcentral.nih.gov/articlerender.fcgi?artid=1420316&tool=pmcentrez&rendertype=abstract>.
- [68] Dura, B., Kovacs, G. T. A. & Giovannardi, L. Spatiotemporally controlled cardiac conduction block using high-frequency electrical stimulation. *PloS one* **7**, e36217 (2012). URL <http://www.pubmedcentral.nih.gov/articlerender.fcgi?artid=3340354&tool=pmcentrez&rendertype=abstract>.
- [69] Sessolo, M. *et al.* Easy-to-fabricate conducting polymer microelectrode arrays. *Advanced Materials* **25**, 2135–9 (2013). URL <http://www.ncbi.nlm.nih.gov/pubmed/23417987>.
- [70] Klauke, N., Smith, G. L. & Cooper, J. M. Stimulation of isolated ventricular myocytes within an open architecture microarray. *IEEE transactions on bio-medical engineering* **52**, 531–8 (2005). URL <http://www.ncbi.nlm.nih.gov/pubmed/15759583>.
- [71] Schmickler, W. & Santos, E. *Interfacial Electrochemistry* (Springer, 2010), 2 edn.
- [72] Helmholtz, H. Ueber einige Gesetze der Vertheilung elektrischer Ströme in körperlichen Leitern mit Anwendung auf die thierisch-elektrischen Versuche. *Ann. Phys. Chem.* **89**, 211–233, 353–377

- (1853).
- [73] Helmholtz, H. Studien über electriche Grenzsichten. *Annalen der Physik und Chemie* **243**, 337 (1879).
- [74] Bard, A. J. & Faulkner, L. R. *Electrochemical Methods - Fundamentals and Applications* (John Wiley & Sons, INC., 2001), 2 edn.
- [75] Stern, O. Zur Theorie der elektrolytischen Doppelschicht. *Z. Elektrochem.* **30**, 508–516 (1924).
- [76] Thomas, C. A., Springer, P. A., Loeb, G. E., Berwald-Netter, Y. & Okun, L. M. A miniature microelectrode array to monitor the bioelectric activity of cultured cells. *Experimental Cell Research* **74**, 61–6 (1972). URL <http://www.ncbi.nlm.nih.gov/pubmed/4672477>.
- [77] Pine, J. A History of MEA Development. chap. 1 (Springer, 2006).
- [78] Regehr, W. G., Pine, J., Cohan, C. S., Michelle, D. M. & Tank, D. W. Sealing cultured invertebrate neurons to embedded dish electrodes facilitates long-term stimulation and recording **30**, 91–106 (1989).
- [79] Park, S., Song, Y. J., Boo, H. & Chung, T. D. Nanoporous Pt microelectrode for neural stimulation and recording: In vitro characterization. *Journal of Physical Chemistry C* **114**, 8721–8726 (2010).
- [80] Seker, E. *et al.* The fabrication of low-impedance nanoporous gold multiple-electrode arrays for neural electrophysiology studies. *Nanotechnology* **21**, 125504 (2010).
- [81] Cui, X. & Martin, D. C. Fuzzy gold electrodes for lowering impedance and improving adhesion with electrodeposited conducting polymer films. *Sensors and Actuators, A: Physical* **103**, 384–394 (2003).

-
- [82] Janders, M., Egert, U., Stelzle, M. & Nisch, W. Novel thin film titanium nitride micro-electrodes with excellent charge transfer capability for cell stimulation and sensing applications. *Proceedings of 18th Annual International Conference of the IEEE Engineering in Medicine and Biology Society* **1**, 245–247 (1996).
- [83] Fejtl, M., Stett, A., Nisch, W., Boven, K.-H. & Möller, A. On micro-electrode array revival: its development, sophistication of recording, and stimulation. In Taketani, M. & Baudry, M. (eds.) *Advances in Network Electrophysiology*, chap. 2 (Springer, 2006).
- [84] Ludwig, K. a. *et al.* Poly(3,4-ethylenedioxythiophene) (PEDOT) polymer coatings facilitate smaller neural recording electrodes. *Journal of neural engineering* **8**, 014001 (2011).
- [85] Venkatraman, S. *et al.* In vitro and in vivo evaluation of PEDOT microelectrodes for neural stimulation and recording. *IEEE Transactions on Neural Systems and Rehabilitation Engineering* **19**, 307–316 (2011).
- [86] Gerwig, R. *et al.* PEDOT-CNT composite microelectrodes for recording and electrostimulation applications: fabrication, morphology, and electrical properties. *Frontiers in Neuroengineering* **5**, 1–11 (2012).
- [87] Zhou, H., Cheng, X., Rao, L., Li, T. & Duan, Y. Y. Poly(3,4-ethylenedioxythiophene)/multiwall carbon nanotube composite coatings for improving the stability of microelectrodes in neural prostheses applications. *Acta Biomaterialia* **9**, 6439–6449 (2013). URL <http://dx.doi.org/10.1016/j.actbio.2013.01.042>.
- [88] Deng, M. *et al.* Electrochemical deposition of polypyrrole/graphene oxide composite on microelectrodes towards tuning the electrochemical properties of neural probes. *Sensors & Actuators: B. Chemical* **158**, 176–184 (2011). URL <http://dx.doi.org/10.1016/j.snb.2011.05.062>.
- [89] Maher, M. P., Pine, J., Wright, J. & Tai, Y. C. The neurochip: a new multielectrode device for stimulating and recording
-

- from cultured neurons. *Journal of Neuroscience Methods* **87**, 45–56 (1999). URL <http://www.ncbi.nlm.nih.gov/pubmed/10065993>.
- [90] Wrobel, G. *et al.* Transmission electron microscopy study of the cell-sensor interface. *Journal of the Royal Society: Interface* **5**, 213–22 (2008). URL <http://www.pubmedcentral.nih.gov/articlerender.fcgi?artid=2705973&tool=pmcentrez&rendertype=abstract>.
- [91] Sommerhage, F. *et al.* Membrane allocation profiling: a method to characterize three-dimensional cell shape and attachment based on surface reconstruction. *Biomaterials* **29**, 3927–35 (2008). URL <http://www.ncbi.nlm.nih.gov/pubmed/18621415>.
- [92] Joye, N., Schmid, A., Leblebici, Y., Member, S. & Model, A. An electrical model of the cell-electrode interface for high-density microelectrode arrays. In *30th Annual International IEEE EMBS Conference*, 559–562 (2008).
- [93] Fromherz, P. The Neuron-semiconductor interface. In *Bioelectronics*, chap. 12, 339–349 (Wiley-VCH Verlag GmbH & Co. KGaA, 2005).
- [94] Banci, L. *Metallomics and the Cell* (Springer, 2013).
- [95] Takahashi, A., Camacho, P., Lechleiter, J. D. & Herman, B. Measurement of intracellular calcium. *Physiological Reviews* **79**, 1089–125 (1999). URL <http://www.ncbi.nlm.nih.gov/pubmed/10508230>.
- [96] Thermo Fisher. Fluo-4, AM, cell permeant (2015). URL <https://www.thermofisher.com/order/catalog/product/F14201>.
- [97] Neher, E. & Augustine, G. J. Calcium gradients and buffers in bovine chromaffin cells. *The Journal of Physiology* **450**, 273–301 (1992).
- [98] Bootman, M. D., Rietdorf, K., Collins, T., Walker, S. & Sanderson, M. Ca²⁺-sensitive fluorescent dyes and intracellular

-
- Ca²⁺ imaging. *Cold Spring Harbor Protocols* **8**, 83–99 (2013).
- [99] MicroChemicals. Chromium Etching (2013). URL www.microchemicals.com/downloads/application_notes.html.
- [100] Hirvonen, J. K., Weisenberger, W. H., Westmoreland, J. E. & Meussner, R. A. Backscattering investigation of low temperature migration of chromium through gold films. *Applied Physics Letters* **37**, 15–18 (2012).
- [101] Thomas, R. E. & Haas, G. A. Diffusion measurements in thin films utilizing work function changes: Cr into Au. *Journal of Applied Physics* **4900** (2007).
- [102] Slusark, W., Lalevic, B. & Fuschillo, N. Structure and electrical conductivity of cosputtered gold-chromium alloy films. *Journal of Applied Physics* **44**, 2891–2892 (1973).
- [103] Rairden, J., Neugebauer, C. A. & Sigsbee, R. A. Interdiffusion in thin conductor films- chromium/gold, nickel/gold and chromium silicide/gold. *Metallurgical Transactions* **2**, 719–722 (1971).
- [104] Shimatsu, T. & Uomoto, M. Atomic diffusion bonding of wafers with thin nanocrystalline metal films. *Journal of Vacuum Science & Technology B* **28**, 706 (2010).
- [105] Moody, N. R., Adams, D. P., Medlin, D., Headley, T. & Yang, N. Effects of diffusion on interfacial fracture of gold-chromium hybrid microcircuit films. *International Journal of Fracture* **119/120**, 407–419 (2003).
- [106] Kenrick, P. Grain boundary diffusion effects in films of gold and chromium. *Nature* **217**, 1249–1251 (1968).
- [107] Holloway, P. H. Gold/chromium metallizations for electronic devices. *Gold Bulletin* **12**, 99–106 (1979).
- [108] Mehrer, H. Diffusion: introduction and case studies in metals and binary alloys. In Heitjans, P. & Kärger, J. (eds.) *Diffusion in Condensed Matter* (Springer, 2005).
-

References

- [109] Wikipedia entry "Electrical Impedance". URL https://en.wikipedia.org/wiki/Electrical_impedance.
- [110] MacDonald, J. R. *Impedance Spectroscopy: Emphasizing Solid Materials and Systems* (Wiley, New York, 1987).
- [111] Binnig, G. & Quate, C. F. Atomic Force Microscope. *Physical Review Letters* **56**, 930–933 (1986).
- [112] Kittel, C. *Einführung in die Festkörperphysik* (Oldenbourg Wissenschaftsverlag GmbH, München, 2006).
- [113] Wikipedia entry "Atomic Force Microscopy" (2015). URL https://en.wikipedia.org/wiki/Atomic_force_microscopy#Tapping_Mode.
- [114] Goldstein, J. *et al.* *Scanning Electron Microscopy and X-Ray Microanalysis* (Plenum Press, New York, 1992), 2 edn.
- [115] Wikipedia entry "Energy-Dispersive X-Ray Spectroscopy" (2015). URL https://en.wikipedia.org/wiki/Energy-dispersive_X-ray_spectroscopy.
- [116] Grundlagen der Anregung von Röntgenstrahlen durch Elektronen. URL <http://www.mikroanalytik.de/info1.phtml#link5>.
- [117] Reyntjens, S. & Puers, R. A review of focused ion beam applications in microsystem technology. *J. Micromech. Microeng.* **11**, 287–300 (2001).
- [118] Giannuzzi, L. A. & Stevie, F. A. (eds.) *Introduction to Focused Ion Beams: Instrumentation, Theory, Techniques and Practice* (Springer Science+Business Media, 2005).
- [119] Kwok, D. Y. & Neumann, A. W. U. Contact angle measurement and contact angle interpretation. *Advances in Colloid and Interface Science* **81**, 167–249 (1999).
- [120] Meiron, T. S., Marmur, A. & Saguy, I. S. Contact angle measurement on rough surfaces. *Journal of Colloid and Interface Science* **274**, 637–644 (2004).

-
- [121] Law, J. K. Y. *et al.* The use of microelectrode array (MEA) to study the protective effects of potassium channel openers on metabolically compromised HL-1 cardiomyocytes. *Physiological Measurement* **30**, 155–67 (2009). URL <http://www.ncbi.nlm.nih.gov/pubmed/19136734>.
- [122] Santoro, F., Neumann, E., Panaitov, G. & Offenhäusser, A. FIB section of cell-electrode interface: An approach for reducing curtaining effects. *Microelectronic Engineering* **124**, 17–21 (2014). URL <http://dx.doi.org/10.1016/j.mee.2014.04.021>.
- [123] Chemicon. ReNcell VM Immortalized Cell Line - Product Information (2006).
- [124] Morgan, P. J., Hübner, R., Rolfs, A. & Frech, M. J. Spontaneous calcium transients in human neural progenitor cells mediated by transient receptor potential channels. *Stem Cells and Development* **22**, 1–36 (2013).
- [125] Yu, Y., Gu, S., Huang, H. & Wen, T. Combination of bFGF, heparin and laminin induce the generation of dopaminergic neurons from rat neural stem cells both in vitro and in vivo. *Journal of the Neurological Sciences* **255**, 81–86 (2007).
- [126] Choi, S. H. *et al.* A three-dimensional human neural cell culture model of Alzheimer’s disease. *Nature* (2014). URL <http://dx.doi.org/10.1038/nature13800>.
- [127] Colombres, M. *et al.* Heparin activates Wnt signaling for neuronal morphogenesis. *Journal of Cellular Physiology* **216**, 805–815 (2008).
- [128] Kirkeby, A. *et al.* Generation of regionally specified neural progenitors and functional neurons from human embryonic stem cells under defined conditions. *Cell Reports* **1**, 703–714 (2012). URL <http://dx.doi.org/10.1016/j.celrep.2012.04.009>.
- [129] Peischard, S. Development of Dopaminergic Cell Culture Systems for On-Chip Neurotransmitter Release. Tech. Rep., RWTH
-

- Aachen Universtiy (2015).
- [130] Eick, S. *Extracellular Stimulation of Individual Electrogenic Cells with Micro-Scaled Electrodes*. Ph.D. thesis (2010).
- [131] Rinklin, P. *Microwire Crossbar Arrays for Chemical, Mechanical, and Thermal Stimulation of Cells*. Ph.D. thesis, RWTH Aachen (2014).
- [132] Norlin, A., Pan, J. & Leygraf, C. Investigation of interfacial capacitance of Pt, Ti and TiN coated electrodes by electrochemical impedance spectroscopy. *Biomolecular Engineering* **19**, 67–71 (2002). URL <http://www.ncbi.nlm.nih.gov/pubmed/12202164>.
- [133] Schnitker, J., Afanasenkau, D., Wolfrum, B. & Offenhäusser, A. Planar reference electrodes on multielectrode arrays for electrochemical measurements of ionic currents. *Physica Status Solidi (a)* **210**, 892–897 (2013).
- [134] Moulton, S. E., Barisci, J. N., Bath, A., Stella, R. & Wallace, G. G. Studies of double layer capacitance and electron transfer at a gold electrode exposed to protein solutions. *Electrochimica Acta* **49**, 4223–4230 (2004). URL <http://linkinghub.elsevier.com/retrieve/pii/S0013468604003688>.
- [135] Buchholz, S., Fuchs, H., Rabe, J. P., Buchholz, S. & Fuchs, H. Surface structure of thin metallic films on mica as seen by scanning tunneling microscopy, scanning electron microscopy, and low energy electron diffraction. *Journal of Vacuum Science & Technology B* **857** (2010).
- [136] Salvadori, M. C. *et al.* Platinum and gold thin films deposited by filtered vacuum arc: morphological and crystallographic grain sizes. *Surface Coatings & Technology* **200**, 2965–2969 (2006).
- [137] van Attekum, P., Woerlee, P., Verkade, G. & Hoeben, A. Influence of grain boundaries and surface Debye temperature on the electrical resistance of thin gold films. *Physical Review B* **29**

- (1984).
- [138] Chidsey, C. E. D., Loiacono, D. N., Sleator, T. & Nakahara, S. STM study of the surface morphology of gold on mica. *Surface Science* **200**, 45–66 (1988).
- [139] Thomas, R. E. & Haas, G. A. Diffusion measurements in thin films utilizing work function changes: Cr into Au. *Journal of Applied Physics* **43**, 4900 (2007).
- [140] Majni, G., Ottaviani, G. & Prudenziati, M. Interdiffusion of thin Cr and Au films deposited on silicon. *Thin Solid Films* **38**, 15–19 (1976).
- [141] Hansen, M. *Constitution of Binary Alloys* (McGraw-Hill Book Company, 1958), 2 edn.
- [142] Wikipedia entry "Eutectic System" (2015). URL https://en.wikipedia.org/wiki/Eutectic_system.
- [143] Lim, J. Y. & Donahue, H. J. Review cell sensing and response to micro- and nanostructured surfaces produced by chemical and topographic patterning. *Tissue Engineering* **13** (2007).
- [144] Anselme, K. *et al.* Qualitative and quantitative study of human osteoblast adhesion on materials with various surface roughnesses. *Wiley & Sons, Inc.* (1999).
- [145] Huang, H.-h. *et al.* Effect of surface roughness of ground titanium on initial cell adhesion. *Biomolecular Engineering* **21**, 93–97 (2004).
- [146] Chung, T.-W., Liu, D.-Z., Wang, S.-Y. & Wang, S.-S. Enhancement of the growth of human endothelial cells by surface roughness at nanometer scale. *Biomaterials* **24**, 4655–4661 (2003).
- [147] Ponsonnet, L., Comte, V., Othmane, A., Lagneau, C. & Charbonnier, M. Effect of surface topography and chemistry on adhesion, orientation and growth of fibroblasts on nickel-

- titanium substrates. *Materials Science and Engineering* **21**, 157–165 (2002).
- [148] Hallab, N. J., Bundy, K. J., Moses, R. L. & Jacobs, J. J. Evaluation of metallic and polymeric biomaterial surface energy and surface roughness characteristics for directed cell adhesion. *Tissue Engineering* **7**, 55–71 (2001).
- [149] Peyrin, J.-M. *et al.* Axon diodes for the reconstruction of oriented neuronal networks in microfluidic chambers. *Lab on a Chip* **11**, 3663–73 (2011). URL <http://www.ncbi.nlm.nih.gov/pubmed/21922081>.
- [150] Leclerc, A. *et al.* Three dimensional spatial separation of cells in response to microtopography. *Biomaterials* **34**, 8097–104 (2013). URL <http://www.ncbi.nlm.nih.gov/pubmed/23899447>.
- [151] Mahoney, M. J., Chen, R. R., Tan, J. & Saltzman, W. M. The influence of microchannels on neurite growth and architecture. *Biomaterials* **26**, 771–8 (2005). URL <http://www.ncbi.nlm.nih.gov/pubmed/15350782>.
- [152] Herzog, N., Shein-Idelson, M. & Hanein, Y. Optical validation of in vitro extra-cellular neuronal recordings. *Journal of Neural Engineering* **8**, 056008 (2011). URL <http://www.ncbi.nlm.nih.gov/pubmed/21841241>.
- [153] Olsson, R. H., Buhl, D. L., Sirota, A. M., Buzsaki, G. & Wise, K. D. Band-tunable and multiplexed integrated circuits for simultaneous recording and stimulation with microelectrode arrays. *IEEE Transactions on Biomedical Engineering* **52**, 1303–1311 (2005).
- [154] Savitzky, A. & Golay, M. J. Smoothing and differentiation of data by simplified least squares procedures. *Analytical Chemistry* **36**, 1627–1639 (1964).
- [155] Yang, Z., Shen, W., Rottman, J. N., Wikswo, J. P. & Murray, K. T. Rapid stimulation causes electrical remodeling in cultured

- atrial myocytes. *Journal of Molecular and Cellular Cardiology* **38**, 299–308 (2005). URL <http://www.ncbi.nlm.nih.gov/pubmed/15698836>.
- [156] Jacquir, S. *et al.* Cardiac arrhythmias induced by an electrical stimulation at a cellular level. *2008 Computers in Cardiology* 625–628 (2008). URL <http://ieeexplore.ieee.org/lpdocs/epic03/wrapper.htm?arnumber=4749119>.
- [157] Tihaa, I. Investigation of Dopaminergic Cell Systems for Chip-Based Detection of Neurotransmitter Release. Tech. Rep., RWTH Aachen University (2014).
- [158] Debanne, D., Campanac, E., Bialowas, A., Carrier, E. & Alcaraz, G. Axon physiology. *Physiological reviews* **91**, 555–602 (2011).
- [159] Hutchins, B. I. & Kalil, K. Differential outgrowth of axons and their branches is regulated by localized calcium transients. *The Journal of neuroscience : the official journal of the Society for Neuroscience* **28**, 143–153 (2008). NIHMS150003.
- [160] Spitzer, N. C. Electrical activity in early neuronal development. *Nature* **444**, 707–712 (2006).
- [161] Ross, W. N., Miyazaki, K., Popovic, M. a. & Zecevic, D. Imaging with organic indicators and high-speed charge-coupled device cameras in neurons: some applications where these classic techniques have advantages. *Neurophotonics* **2**, 021005 (2014). URL <http://neurophotonics.spiedigitallibrary.org/article.aspx?doi=10.1117/1.NPh.2.2.021005>.
- [162] Hasegawa, M. & Horie, K. Photophysics, photochemistry, and optical properties of polyimides. *Progress in Polymer Science (Oxford)* **26**, 259–335 (2001).
- [163] Eijkel, J. C. T., Bomer, J., Tas, N. R. & van den Berg, A. 1-D nanochannels fabricated in polyimide. *Lab on a Chip* **4**, 161–163 (2004).

References

- [164] Lu, B., Zheng, S., Quach, Q. & Tai, Y.-c. A study of the autofluorescence of parylene materials for μ TAS applications. *Lab on a Chip* **10**, 1826–1834 (2010).
- [165] Smetters, D., Majewska, A. & Yuste, R. Detecting action potentials in neuronal populations with calcium imaging. *Methods* **18**, 215–221 (1999).
- [166] Moreaux, L. & Laurent, G. Estimating firing rates from calcium signals in locust projection neurons in vivo. *Frontiers in Neural Circuits* **1**, 2 (2007). URL <http://www.pubmedcentral.nih.gov/articlerender.fcgi?artid=2526277&tool=pmcentrez&rendertype=abstract>.
- [167] Yuste, R., MacLean, J., Vogelstein, J. & Paninski, L. Imaging action potentials with calcium indicators. *Cold Spring Harbor Protocols* **2011**, 985–9 (2011). URL <http://www.ncbi.nlm.nih.gov/pubmed/21807854>.
- [168] Quan, T., Liu, X., Lv, X., Chen, W. R. & Zeng, S. Method to reconstruct neuronal action potential train from two-photon calcium imaging. *Journal of Biomedical Optics* **15**, 066002 (2010). URL <http://www.pubmedcentral.nih.gov/articlerender.fcgi?artid=3032232&tool=pmcentrez&rendertype=abstract>.
- [169] Clapham, D. E. Calcium signaling. *Cell* **131**, 1047–1058 (2007).
- [170] Hirase, H., Qian, L., Barthó, P. & Buzsáki, G. Calcium dynamics of cortical astrocytic networks in vivo. *PLoS Biology* **2**, 494–499 (2004).
- [171] Park, S. Y. *et al.* Enhanced differentiation of human neural stem cells into neurons on graphene. *Advanced Materials* **23**, H263–7 (2011). URL <http://www.ncbi.nlm.nih.gov/pubmed/21823178>.
- [172] Meyer, T., Boven, K.-H. & Fejtl, M. Micro-Electrode Arrays in Cardiac Safety Pharmacology. *Drug Safety* **27**, 763–772 (2004).

Author's list of publications

- Czeschik, A., Rinklin, P., Derra, U., Ullmann, S., Holik, P., Steltenkamp, S., Offenhäusser, A. & Wolfrum, B. Nanostructured cavity devices for extracellular stimulation of HL-1 cells. *Nanoscale*, 7, 9275 (2015). doi:10.1039/c5nr01690h
- Czeschik, A., Offenhäusser, A. & Wolfrum, B. Fabrication of MEA-based nanocavity sensor arrays for extracellular recording of action potentials. *Physica Status Solidi (a)*, 211(6), 1462-1466 (2014). doi:10.1002/pssa.201330365

Author's list of publications

Acknowledgements

Accomplishing a PhD project would not be possible without advice, support and legwork. I was very lucky to find lots of these during my PhD time. I want to express my thanks to the PGI-8/ICS-8 institute and the following people in particular:

Prof. Dr. Bernhard Wolfrum - for the opportunity to work in his group, his excellent supervision and a skilled course correction from time to time. I highly appreciated to learn from you. Your inspiring attitude is a benefit for everybody working with you.

Prof. Dr. Andreas Offenhäusser - for being the leading part with the leading thought of our institute. Thank you for bringing together such a wide range of people and disciplines, creating an unique working environment.

Prof. Dr. Jörg Fitter - thank you for kindly taking over the role of the second examiner of my work.

Marko Banzet - for cleanroom processing, steadily providing me with chips, his sunny disposition and aura of sanity.

Peter Holik and **Dr. Siegfried Steltenkamp** from CAESAR Bonn - for collaboration and chip production.

Acknowledgements

Norbert Wolters and **Dieter Lomparski** - for building amplifier system and software interface for action potential recordings and stimulation experiments.

Bettina Breuer and **Rita Fricke** - for cell culture and lab organization. Thank you for relentlessly fighting chaos and anarchy, never without a smile and a nice word.

Susanne Bippus - for answering every kind of organizational question and administrative support.

Dr. Elmar Neumann and **Elke Brauweiler-Reuters** - for their helpful and accurate work, for the FIB cuts and EDX spectra.

Dr. Vanessa Maybeck - for being my biolab encyclopedia, always professional, having an answer to every scientific/logistic/stupid question and fearlessly facing my attempts in english prose.

Dr. Philipp Rinklin - for the Matlab script for crosscorrelation analysis of HL-1 activity, for lots of tips and tricks in the lab and sharing his wisdom regarding thesis writing.

Dr. Kathrin Zobel and **Dr. Wienke Lange** - for biological advice and support on the ReNcell differentiation.

Volker Schöps - for the AFM and SEM images on the interdiffusion samples, for cleanroom processing and chemical advice.

Fabian Brings - for his work on the BiomasAnalyzer, advice for signal analysis and lots of noise discussion.

Jan Schnitker - for his work on the amplifier system.

Jonas Albers - for extensive discussion on calcium imaging and neuronal signaling.

Sabrina Ullmann and **Ulrike Derra** - for support in nanocavity etching statistics and optical HL-1 recordings.

Kay Krause - for lively exchange about the amplifier system,

impedance spectroscopy and electrochemistry. It was always nice to have another physicist down the corridor.

Irina Tihaa and **Stefan Peischard** - for their work on dopaminergic cell systems within their master projects. Especially for the immunohistochemical stainings of neural progenitor and stem cells.

I am very thankful for the international and interdisciplinary working environment I found here in Jülich. It allowed me not only to learn on a high level, but also to build up some interesting and inspiring friendships, long-lasting even beyond my time here. My personal acknowledgments go out to:

„Stammtisch Jülich“ – **Koji, Sung-Eun, Mana** and especially **Wienke**. Thank you for supporting me and providing a social life in Jülich. I always appreciated the nights out, Japanese cooking lessons and sophisticated movies.

My office mates **Geng** and **Dmitry** for their supportive and even-minded attitude. Geng, thank you for valuable pearls of wisdom and intercultural exchange – between Germany and China, in Germany and in China. Dmitry, thank you for being not only annoying, but also entertaining and the constant source of Russian spirit (pun intended). No creativity without insanity.

Jonas – for introducing me to the early morning routine, for flank protection in lab work and nerf gun battles.

Ranjita and **Enno**: For the wisdom of a sisterly friend and a how-to guide to the PGI-8/ICS-8 universe.

Irina – First student, then ~~student~~ and friend. Thank you for being the guinea pig to my mentoring experiments.

Volker – for coming up just in the right moment - unexpected but needed. Thank you for teaming up, being a person of trust, a comrade,

Acknowledgements

a jester and an unpaid work force. Having you in my head and by my side allowed me to tip the balance in my favor.

Band / Volume 111

Long range order in 3D nanoparticle assemblies

E. Josten (2015), 238 pp

ISBN: 978-3-95806-087-6

Band / Volume 112

Silicon nanowire structures for neuronal cell interfacing

S. Pud (2015), 153 pp

ISBN: 978-3-95806-089-0

Band / Volume 113

**Memristive Phenomena –
From Fundamental Physics to Neuromorphic Computing**

Lecture Notes of the 47th IFF Spring School 2016

22 February – 04 March 2016, Jülich, Germany

ed. by R. Waser and M. Wuttig (2016), ca 1000 pp

ISBN: 978-3-95806-091-3

Band / Volume 114

**Single-Cell Analysis of Microbial Production Strains
in Microfluidic Bioreactors**

A. M. Grünberger (2015), XIX, 225 pp

ISBN: 978-3-95806-092-0

Band / Volume 115

**Magnetic order and spin dynamics in the
extended kagome system $\text{CaBaCo}_2\text{Fe}_2\text{O}_7$**

J. Reim (2015), viii, 144 pp

ISBN: 978-3-95806-097-5

Band / Volume 116

**Structural and electronic investigations on homo- and hetero-organic
layers involving CuPc on silver single crystal surfaces**

K. M. Schönauer (2015), x, 148 pp

ISBN: 978-3-95806-112-5

Band / Volume 117

**First-principles investigation of inelastic magnetic excitations
in nanostructures deposited on surfaces**

B. J. Schweflinghaus (2016), v, 204 pp

ISBN: 978-3-95806-115-6

Band / Volume 118

Magnetic, structural, and electronic properties of NiFe_2O_4 ultrathin films

M. Hoppe (2016), vii, 118 pp

ISBN: 978-3-95806-122-4

Band / Volume 119

First-principle investigation of displacive response in complex solids

D. A. Klüppelberg (2016), xi, 179 pp

ISBN: 978-395806-123-1

Band / Volume 120

**Beam Cooling at COSY and HESR – Theory and Simulation –
Part 1 Theory**

H. Stockhorst, T. Katayama and R. Maier (2016), v, 192 pp

ISBN: 978-3-95806-127-9

Band / Volume 121

**Scanning tunneling microscopy of single-molecule magnets and hybrid-
molecular magnets: Two approaches to molecular spintronics**

V. Heß (2016), x, 127 pp

ISBN: 978-3-95806-128-6

Band / Volume 122

**Bulk and surface sensitive energy-filtered photoemission microscopy
using synchrotron radiation for the study of resistive switching memories**

M. C. Patt (2016), viii, 247 pp

ISBN: 978-3-95806-130-9

Band / Volume 123

Group IV Epitaxy for Advanced Nano- and Optoelectronic Applications

S. Wirths (2016), vi, 116, XXX pp

ISBN: 978-3-95806-132-3

Band / Volume 124

**Strained Silicon-Germanium/Silicon Heterostructure Tunnel FETs
for Low Power Applications**

S. Blaeser (2016), iv, 91, xvii pp

ISBN: 978-3-95806-135-4

Band / Volume 125

**Nanocavity Arrays for Extracellular Recording and Stimulation of
Electroactive Cell Systems**

A. Czeschik (2016), x, 162 pp

ISBN: 978-3-95806-144-6

Weitere *Schriften des Verlags im Forschungszentrum Jülich* unter
<http://www.zb1.fz-juelich.de/verlagextern1/index.asp>

**Schlüsseltechnologien /
Key Technologies
Band / Volume 125
ISBN 978-3-95806-144-6**

